ÉCOLE DOCTORALE
ENERGIE, MATÉRIAUX, SCIENCES DE LA TERRE ET DE L'UNIVERS
PRISME ORLEANS/ FSVPSL BEIJING

THÈSE EN COTUTELLE INTERNATIONALE présentée par:

Zhaojing NI

soutenue le : 27 Juin 2022

pour obtenir le grade de:
Docteur de Université d'Orléans
et de Beijing Institute of Technology

Discipline/ Spécialité : Energétique

Rainbow Experiment and Numerical Study on the Evaporation Characteristics of Droplets

THÈSE dirigée par :

Fabrice Foucher	Professeur, Université d'Orléans
Kai Han	Professeur associé, Beijing Institute of Technology

RAPPORTEURS :

Frédéric Grisch	Professeur, INSA-Rouen
Gilles BRUNEAUX	Chef de Département(HDR), IFP Energies nouvelles

---

JURY :

Frédéric Grisch	Professeur, INSA-Rouen, Président du jury
Gilles BRUNEAUX	Chef de Département(HDR), IFP Energies nouvelles
Baolu Shi	Professeur, Beijing Institute of Technology
Chenglong Tang	Professeur, Xi'an Jiaotong University
Zhenyu Zhang	Professeur associé, Beijing Institute of Technology
Fabrice Foucher	Professeur, Université d'Orléans
Camille Hespel	Professeur associé, Université d'Orléans

[Zhaojing NI]

[Expérience Rainbow et étude numérique sur les caractéristiques d'évaporation des gouttelettes]

Résumé :
L'évaporation des gouttelettes est omniprésente dans de nombreuses industries et applications biologiques. L'évaporation des gouttelettes dans les moteurs est essentielle pour le comportement de combustion du carburant pulvérisé et les performances d'émission. Les recherches sur le processus d'évaporation de différents types de gouttelettes dans des conditions ambiantes complexes sont essentielles pour obtenir une combustion propre et efficace. Ce travail applique les approches expérimentales et de simulation pour mettre en lumière l'influence conjointe des conditions ambiantes et du type de combustible liquide sur le comportement d'évaporation des gouttelettes. Premièrement, un modèle d'équilibre vapeur-liquide non idéal basé sur le modèle de conductivité et de diffusivité effectives a été créé et validé. Deuxièmement, le système expérimental d'évaporation de gouttelettes basé sur la technique de l'arc-en-ciel a été conçu et mis en place. Un algorithme d'inversion a été proposé en tenant compte de l'impact du gradient d'indice de réfraction et du changement de forme de la gouttelette sur l'angle arc-en-ciel. Les distributions de diamètre et de température des gouttelettes en vaporisation dans des conditions de haute température ont été mesurées simultanément. De plus, les processus d'évaporation de gouttelettes binaires mono et éthanol/heptane dans différentes conditions ont été étudiés avec des méthodes expérimentales et de simulation. Les résultats révèlent une inversion de l'ordre d'évaporation des composants éthanol et heptane à la surface des gouttelettes lorsque le composant plus léger éthanol domine le mélange. La comparaison de l'indice de réfraction entre les mesures de l'arc-en-ciel et les prédictions du modèle confirme la précision du modèle d'équilibre vapeur-liquide non idéal dans la prédiction du comportement d'évaporation préférentiel de la gouttelette binaire pour la première fois.
Mots clés : Évaporation des gouttelettes, Réfractométrie arc-en-ciel, Modèle d'évaporation binaire, Évaporation préférentielle, Détection de température

[Rainbow Experiment and Numerical Study on the Evaporation Characteristics of Droplets]

Summary :
Droplet evaporation are ubiquitous in many industries and biological applications. The evaporation of droplets in engines is critical for the combustion behavior of fuel spray and the emission performance. The investigations on the evaporation process of different kinds of droplets under complex ambient conditions are essential to achieve clean and efficient combustion. This work applies the experimental and simulation approaches to shed a light on the joint influence of ambient conditions and liquid fuel type on the evaporation behavior of droplets. Firstly, a non-ideal vapor-liquid equilibrium model based on the effective conductivity and diffusivity model has been created and validated. Secondly, the droplet evaporation experimental system based on the rainbow technique has been designed and established. An inversion algorithm has been proposed by taking into account the impact of refractive index gradient and shape change of droplet on the rainbow angle. The diameter and temperature distributions of vaporizing droplets under high-temperature conditions have been measured simultaneously. Furthermore, the evaporation processes of mono and ethanol/heptane binary droplets under different conditions have been investigated with both experimental and simulation methods. The results reveal an inversion of the evaporation order of ethanol and heptane components at the droplet surface when the lighter component ethanol dominates the mixture. The comparison of the refractive index between the rainbow measurements and model predictions confirms the accuracy of the non-ideal vapor-liquid equilibrium model in predicting the preferential evaporation behavior of binary droplet for the first time.
Keywords : Droplet evaporation, Rainbow refractometry, Binary evaporation model, Preferential evaporation, Temperature detection

Laboratoire Pluridisciplinaire de Recherche Ingénierie des Systèmes, Mécanique, Énergétique
8 rue Léonard de Vinci
45072 Orléans Cedex 2

1. Introduction

Le transport et l'évaporation des gouttelettes sont omniprésents dans de nombreuses industries et applications biologiques allant des moteurs à la gestion thermique en passant par l'impression à jet d'encre, etc. Compte tenu de son importance, le comportement d'évaporation ainsi que les facteurs d'influence et les résultats ultérieurs ont reçu une grande attention dans différents domaines.

Pour comprendre le processus de transfert de chaleur et de masse des gouttelettes en ce qui concerne son importance dans les applications pratiques, de nombreuses recherches ont été menées jusqu'à présent. La section examine le développement et la perspective des recherches sur l'évaporation des gouttelettes du point de vue de l'expérience et de la simulation. Pour les études expérimentales, les gouttelettes stationnaires suspendues avec un fil ou à l'aide d'approches acoustiques/optiques/électriques et les gouttelettes mobiles en chute libre sont les configurations de gouttelettes les plus courantes.

Par rapport à la configuration de la technique d'ombrage rétroéclairé pour enregistrer le changement de taille des gouttelettes en suspension, la combinaison de la technique de l'arc-en-ciel avec des gouttelettes en chute libre peut mesurer avec précision plusieurs paramètres, notamment la taille, la température ou la concentration des gouttelettes pendant le processus d'évaporation. Ces avantages sont non seulement utiles pour révéler le mécanisme sous-jacent du processus d'évaporation, mais également utiles pour la validation du modèle. En conséquence, ce travail adopte la technique de l'arc-en-ciel pour étudier le processus d'évaporation du flux de gouttelettes en ce qui concerne son potentiel et sa précision.

Les modèles d'évaporation de gouttelettes peuvent être classés dans le modèle unidimensionnel classique et les simulations de la dynamique des fluides computationnelle (CFD). Les avantages et les inconvénients du modèle 1D et de la CFD sont nettement distincts. Comparé aux travaux CFD, le modèle unidimensionnel d'évaporation d'une seule gouttelette est plus réalisable au niveau de la pulvérisation car ils sont moins sollicités sur les ressources informatiques. Alors que le CFD donne un aperçu de la dynamique 3D complexe et du processus de transport thermique au

détriment des ressources numériques. Dans ce cas, il faut équilibrer les bénéfices et les coûts en fonction de la cible. Dans les applications pratiques, un grand nombre de gouttelettes doit être considéré. La solution directe de ces équations de conservation dans chaque gouttelette n'est pas abordable dans la modélisation de pulvérisation. Par conséquent, un modèle simplifié pour prédire le transfert de chaleur et de masse est nécessaire.

La modélisation des gouttelettes multicomposants reste une tâche difficile. Chaque composant du mélange a un comportement d'évaporation différent. Les différences dans la séquence d'évaporation et le taux d'évaporation conduisent à la distribution temporelle et spatiale inhomogène de la concentration dans la phase liquide. Le transfert de masse de chaque composant est considéré comme contrôlé par diffusion. Lorsque les mélanges multi-composants sont composés de composants ayant une grande différence de polarité, il est inapproprié de le traiter comme un liquide idéal car l'équilibre de phase non idéal a un impact significatif sur le processus d'évaporation. Par exemple, la combinaison de carburants alcooliques et de carburants hydrocarbonés n'est pas un mélange idéal en raison de la polarité d'une molécule d'alcool.

Visant la description précise du comportement d'évaporation des gouttelettes et le développement de la théorie de l'évaporation et de la technique de mesure, la combinaison de la méthode expérimentale et de l'approche de simulation a été utilisée pour analyser le comportement d'évaporation des gouttelettes mono et binaires dans différentes conditions. Du point de vue de la simulation, la littérature ci-dessus a démontré la nécessité d'adopter un modèle simple mais fiable concernant l'incorporation dans une échelle de pulvérisation avec un grand nombre de gouttelettes. Par conséquent, un modèle amélioré basé sur le modèle de conductivité et de diffusivité effectives a été proposé, qui intègre les impacts de la convection, les paramètres physiques dépendant de la température, l'équilibre vapeur-liquide non idéal du mélange et l'effet de la distance entre les voisins. gouttelettes. D'un autre côté, un effort expérimental parallèle pour obtenir le comportement d'évaporation des gouttelettes en mouvement demande de l'ingéniosité. Pour être réaliste, les gouttelettes testées doivent être petites (de l'ordre de 100 μm) et exemptes de tout

dispositif de suspension. En conséquence, la combinaison de la technique arc-en-ciel de haute précision avec des gouttelettes en chute libre a été utilisée pour mesurer simultanément la taille, la température et la concentration des gouttelettes pendant le processus d'évaporation. Un algorithme prenant en compte le gradient d'indice de réfraction dans la phase liquide et le changement de forme a été développé pour récupérer les paramètres d'évaporation à partir de l'image de diffusion, ce qui améliore considérablement la précision du traitement des données. Ensuite, les processus d'évaporation de gouttelettes binaires mono et éthanol/heptane avec différentes conditions ont été étudiés avec des méthodes expérimentales et de simulation. La thèse comporte principalement six chapitres :

Le chapitre 1 présente les applications et le contexte de l'évaporation des gouttelettes. Les recherches expérimentales et les études numériques largement adoptées dans l'étude des évaporations de gouttelettes ont été décrites. La nécessité d'adopter les configurations expérimentales de la technique de l'arc-en-ciel avec les gouttelettes en chute libre est décrite. Une revue de la simulation d'évaporation de gouttelettes pose les bases de la thèse.

Le chapitre 2 décrit systématiquement la méthodologie expérimentale, y compris l'ensemble de la configuration et chaque segment, la vérification de la théorie de l'arc-en-ciel pour le post-traitement. Le paramètre physique du carburant testé et sa dépendance à la température dans le présent travail ont également été introduits. Un algorithme d'inversion est proposé pour le post-traitement des données expérimentales. Sur cette base, la fiabilité et la répétabilité de la méthode de mesure ont été vérifiées.

Le chapitre 3 décrit les détails de la méthode numérique, y compris la description physique, les hypothèses du modèle, la solution du processus de transfert de chaleur et de masse et l'algorithme numérique. L'impact de la convection, les paramètres physiques dépendant de la température, l'équilibre non idéal du mélange et l'effet de la distance entre les gouttelettes voisines sont pris en compte. Par ailleurs, le modèle est validé par des résultats expérimentaux et de simulation dans la littérature.

Le chapitre 4 se concentre sur le comportement d'évaporation transitoire des gouttelettes d'éthanol et d'heptane par des mesures d'arc-en-ciel. Le diamètre des gouttelettes récupérées et l'indice de réfraction des motifs arc-en-ciel ont été comparés

aux prédictions du modèle. En conséquence, les évolutions temporelles et les distributions spatiales de la température sont obtenues. La différence entre les prédictions du modèle et les résultats expérimentaux a été étudiée plus en détail.

Le chapitre 5 rend compte du comportement d'évaporation des gouttelettes binaires d'éthanol et d'heptane obtenues par des méthodes expérimentales et de simulation. L'influence de l'équilibre vapeur-liquide non idéal sur le comportement préférentiel des gouttelettes binaires est observée et confirmée par les résultats expérimentaux de l'arc-en-ciel. L'influence du couplage de la température ambiante, de la pression et des compositions en phase liquide sur l'évaporation préférentielle des gouttelettes est obtenue.

Le chapitre 6 résume les principaux résultats du présent travail et met en évidence les innovations. Il parle également de l'effort requis dans les travaux futurs.

2. Méthodologie expérimentale

Ce chapitre décrit systématiquement la méthodologie expérimentale, y compris la composition de l'ensemble de la configuration, le fonctionnement de chaque segment, l'algorithme d'extraction des données. Les paramètres physiques du combustible testé et leur dépendance à la température dans le présent travail sont également introduits. Les procédures de post-traitement sont essentielles pour extraire le diamètre des gouttelettes et l'indice de réfraction de la courbe d'intensité lumineuse de diffusion. La précision de la méthode d'inversion des données est examinée. La fiabilité et la répétabilité de la méthode de mesure ont également été vérifiées. Les remarques finales sont résumées ci-dessous :

1. Le système expérimental d'évaporation de gouttelettes basé sur la technique de l'arc-en-ciel a été conçu et établi, qui est principalement composé de la génération de gouttelettes, de la chambre à haute température et du système d'image arc-en-ciel. Un flux de gouttelettes stable peut être obtenu en ajustant la pression d'injection et la fréquence d'excitation du générateur.

2. Un algorithme d'inversion a été proposé pour extraire simultanément le diamètre des gouttelettes et les distributions de température des motifs de diffusion de la lumière pour la première fois. La méthode améliore la précision du processus de

post-traitement en tenant compte de l'impact du gradient d'indice de réfraction et de la modification du changement de forme sur l'angle arc-en-ciel.

3. La dépendance des modèles de diffusion sur le diamètre et l'indice de réfraction a été révélée. Les résultats indiquent que l'indice de réfraction détermine la position angulaire des motifs lumineux de diffusion tandis que le diamètre contrôle la fréquence des pics principaux.

4. Les examens de fiabilité et de répétabilité ont été effectués pour garantir la précision de la mesure de l'arc-en-ciel. Le diamètre aéré et le diamètre d'ondulation évalués à partir des motifs aérés et des structures d'ondulation sont comparés au diamètre obtenu par itération pour vérifier l'algorithme d'inversion.

3. Modèle d'évaporation des gouttelettes

Ce chapitre présente les détails de la méthode numérique. À partir de la description physique et des hypothèses, l'algorithme numérique contient principalement le transfert de chaleur et de masse dans la phase liquide, la diffusion de masse dans la phase gazeuse et l'équilibre entre les phases liquide et gazeuse. Le modèle est validé par des résultats expérimentaux et de simulation dans des références. Les remarques conclusives sont les suivantes :

1. Un modèle d'équilibre vapeur-liquide non idéal basé sur le modèle de conductivité et de diffusivité effectives a été créé. La méthode intègre l'impact de la convection, les interactions entre les gouttelettes voisines, les paramètres physiques dépendant de la température et les différences de polarité entre les différents composants.

2. La validation expérimentale du modèle établi est faite à partir des aspects diamètre et température. Le processus d'évaporation des mélanges multi-composants ABE-diesel (acétone-butanol-éthanol et diesel) et du mélange binaire éthanol/gouttelettes d'eau est simulé et comparé à la littérature.

3. La validation numérique est faite en imitant le même processus d'évaporation de gouttelettes d'éthanol/iso-octane de la littérature. En outre, la capacité du modèle à présenter l'impact de la concentration de vapeur ambiante est examinée en effectuant le processus d'évaporation de gouttelettes binaires heptane-dodécane.

4. Caractérisation du flux de gouttelettes mono

Les caractéristiques d'évaporation transitoire des gouttelettes d'éthanol et d'heptane en chute libre à des températures ambiantes de 373-473 K sont étudiées dans ce chapitre avec la technique de l'arc-en-ciel. En analysant les motifs arc-en-ciel capturés au voisinage de l'angle arc-en-ciel, la taille des gouttelettes, la température équivalente de la gouttelette ainsi que les valeurs de température à l'intérieur de la gouttelette ont été simultanément extraites. Certaines des conclusions sont résumées comme suit :

1. Les pics primaires et les structures d'ondulation sont présentés distinctement dans les images arc-en-ciel en utilisant la configuration expérimentale actuelle. On observe que le motif arc-en-ciel se déplace vers des angles de diffusion inférieurs en augmentant la température ambiante. Alors que la particule de plus grande taille a tendance à avoir plus de pics dans la même plage d'angle de diffusion.

2. L'impact de la température ambiante, du diamètre initial des gouttelettes et du type de combustible sur le taux de réduction de la taille des gouttelettes et le taux de chauffage dans la phase liquide a été obtenu. Les résultats indiquent que les gouttelettes moins volatiles sont plus susceptibles d'être affectées par le changement de température ambiante ou la taille initiale des gouttelettes par rapport aux gouttelettes plus volatiles.

3. Les mesures expérimentales montrent un bon accord avec les résultats de simulation dans la variation de diamètre. Cependant, on observe l'écart entre les températures mesurées et les valeurs prédites, qui provient du gradient de température dans la phase liquide.

4. La distribution parabolique de l'indice de réfraction le long de la direction du rayon est validée. La relation sous-jacente entre la température mesurée et le gradient de température à l'intérieur de la gouttelette est révélée. Les distributions de température dans la phase liquide sont obtenues à partir des mesures arc-en-ciel.

5. Évaporation préférentielle des gouttelettes binaires

Le comportement d'évaporation des gouttelettes binaires d'éthanol et d'heptane a

été étudié dans ce chapitre en utilisant à la fois des méthodes expérimentales et de simulation. La principale contribution est l'observation d'un ordre d'évaporation inverse des composants heptane et éthanol en raison de l'impact d'un équilibre vapeur-liquide non idéal. En outre, le comportement préférentiel des gouttelettes binaires d'éthanol et d'heptane est confirmé avec la mesure de l'arc-en-ciel pour la première fois. Les résultats fournissent une nouvelle vue pour mesurer et comprendre le comportement d'évaporation des gouttelettes binaires. Les principales remarques de conclusion sont les suivantes :

1. L'influence de l'équilibre vapeur-liquide non idéal sur l'évaporation préférentielle des gouttelettes binaires est évaluée. Les résultats révèlent un changement significatif du facteur de séparation et une inversion de l'ordre d'évaporation des composants éthanol et heptane à la surface des gouttelettes lorsque le composant plus léger domine le mélange.

2. La comparaison de l'indice de réfraction entre les mesures arc-en-ciel et les prédictions du modèle confirme la précision du modèle d'équilibre vapeur-liquide non idéal pour prédire pour la première fois le comportement d'évaporation préférentiel des gouttelettes binaires. La nécessité de considérer l'impact du mélange non idéal a également été démontrée.

3. L'influence du couplage de la température ambiante, de la pression et des compositions en phase liquide sur le comportement d'évaporation préférentiel des gouttelettes est révélée. Il révèle que l'effet de l'équilibre vapeur-liquide non idéal est plus susceptible d'être affecté par les conditions ambiantes lorsque les composants plus légers dominent le mélange.

4. L'influence conjointe de la température et des compositions liquides sur l'indice de réfraction de la gouttelette binaire est obtenue. La température contrôle la variation de l'indice de réfraction au début de l'étape d'évaporation tandis que la composition détermine l'indice de réfraction plus tard. En outre, la composition domine la distribution spatiale de l'indice de réfraction près de la surface des gouttelettes.

6. Conclusions et travaux futurs

6.1 Conclusion

Le transport et l'évaporation des gouttelettes sont omniprésents dans de nombreuses industries et applications biologiques allant des moteurs à la gestion thermique en passant par l'impression à jet d'encre, etc. L'évaporation des gouttelettes dans les moteurs détermine la formation de vapeur de carburant, ce qui est essentiel pour le comportement de combustion du carburant pulvérisé et les performances d'émission. Pendant ce temps, la norme d'émission sans cesse croissante et la conscience respectueuse de l'environnement évoquent le changement d'environnement d'évaporation et un certain nombre de carburants alternatifs verts. Les recherches sur le processus d'évaporation de différents types de gouttelettes dans des conditions ambiantes complexes sont essentielles pour obtenir une combustion propre et efficace. La combinaison de la méthode expérimentale et des approches de simulation a été utilisée pour faire la lumière sur l'influence conjointe des conditions ambiantes et du type de carburant liquide sur le comportement d'évaporation des gouttelettes. La réfractométrie arc-en-ciel optique de haute précision a été conçue et mise en place. Un algorithme d'inversion considérant un gradient d'indice de réfraction parabolique dans la phase liquide a été proposé pour extraire simultanément les distributions de diamètre et de température des motifs de diffusion de la lumière. Une analyse systématique des différences entre les données expérimentales et les résultats de simulation a été faite. Les principales conclusions sont les suivantes:

1. Le système expérimental d'évaporation de gouttelettes basé sur la technique de l'arc-en-ciel a été conçu et établi, qui est principalement composé de la génération de gouttelettes, de la chambre à haute température et du système d'image arc-en-ciel. Les examens de fiabilité et de répétabilité ont été effectués pour garantir la précision de la mesure de l'arc-en-ciel.

2. Un algorithme d'inversion a été proposé pour extraire simultanément le diamètre des gouttelettes et les distributions de température des motifs de diffusion de la lumière pour la première fois. La méthode améliore la précision du processus de post-traitement en tenant compte de l'impact du gradient d'indice de réfraction et de la modification du changement de forme sur l'angle arc-en-ciel.

3. Un modèle d'équilibre vapeur-liquide non idéal basé sur le modèle de

conductivité et de diffusivité effectives a été créé. La méthode intègre l'impact de la convection, les interactions entre les gouttelettes voisines, les paramètres physiques dépendant de la température et les différences de polarité entre les différents composants. La précision du modèle établi est vérifiée avec les données expérimentales et les résultats de simulation dans la littérature.

4. Les caractéristiques d'évaporation transitoire des gouttelettes d'éthanol et d'heptane en chute libre à différentes températures ambiantes sont étudiées avec la technique de l'arc-en-ciel. La distribution parabolique de l'indice de réfraction le long de la direction du rayon est validée. La relation sous-jacente entre la température mesurée et le gradient de température à l'intérieur de la gouttelette est révélée.

5. L'impact de la température ambiante, du diamètre initial des gouttelettes et du type de combustible sur le taux de réduction de la taille des gouttelettes et le taux de chauffage dans la phase liquide a été obtenu. Les résultats indiquent que les gouttelettes moins volatiles sont plus susceptibles d'être affectées par le changement de température ambiante ou la taille initiale des gouttelettes par rapport aux gouttelettes plus volatiles.

6. L'influence des compositions liquides sur le comportement d'évaporation préférentiel des gouttelettes binaires est observée. Les résultats révèlent un changement significatif du facteur de séparation et une inversion de l'ordre d'évaporation des composants éthanol et heptane à la surface des gouttelettes lorsque le composant plus léger, l'éthanol, domine le mélange.

7. La comparaison de l'indice de réfraction entre les mesures de l'arc-en-ciel et les prédictions du modèle confirme la précision du modèle d'équilibre vapeur-liquide non idéal pour prédire pour la première fois le comportement d'évaporation préférentiel de la gouttelette binaire. L'influence du couplage de la température ambiante, de la pression et des compositions en phase liquide sur le comportement d'évaporation préférentiel des gouttelettes est révélée.

6.2 Nouveautés

1. La configuration d'évaporation de gouttelettes de haute précision basée sur la technique de l'arc-en-ciel a été conçue et établie. Un algorithme d'inversion a

été proposé en tenant compte de l'impact du gradient d'indice de réfraction et du changement de forme de la gouttelette sur l'angle arc-en-ciel. Les distributions de diamètre et de température de gouttelettes en vaporisation dans des conditions de haute température ont été mesurées simultanément pour la première fois.

2. Un modèle d'équilibre vapeur-liquide non idéal basé sur le modèle de conductivité et de diffusivité effectives a été créé et validé. La méthode intègre l'impact de la convection, les interactions entre les gouttelettes voisines, les paramètres physiques dépendant de la température et les différences de polarité entre les différents composants.
3. L'influence des compositions liquides sur le comportement d'évaporation préférentiel des gouttelettes binaires est observée. Les résultats révèlent une inversion de l'ordre d'évaporation des composants individuels à la surface des gouttelettes lorsque le composant le plus léger domine le mélange. L'expérience arc-en-ciel confirme la précision du modèle d'équilibre vapeur-liquide non idéal en prédisant pour la première fois le comportement d'évaporation préférentiel des gouttelettes binaires.

6.3 Travaux futurs

La description précise du comportement d'évaporation des gouttelettes et le développement de la théorie de l'évaporation et de la technique de mesure ont été réalisés en couplant la méthode expérimentale et l'approche de simulation dans ce travail. Les travaux futurs peuvent se concentrer sur le comportement d'évaporation dans des conditions de haute pression. Il est difficile d'obtenir un flux stable d'une gouttelette en chute libre dans le premier. D'une part, la différence de pression exige une pression d'injection plus élevée du générateur. D'autre part, toute perturbation de pression conduit à l'oscillation du flux de gouttelettes, qui se répercute finalement sur la distorsion des motifs de diffusion. De plus, la simulation est conçue pour une seule goutte, ce qui n'est pas strictement cohérent avec la configuration expérimentale. La gouttelette voisine à l'intérieur du flux de gouttelettes a une influence sur la masse et la diffusion thermique dans la phase vapeur, qui est considérée par le paramètre

d'espacement sans dimension dans le présent modèle. Des efforts supplémentaires peuvent être faits pour étendre le modèle de gouttelette unique aux configurations de flux de gouttelettes.

ACKNOWLEDGMENT

This work has received substantial supports from numerous people and several institutes. It is the outcome of international collaborations between two universities in two countries. Firstly, I would like to give my deepest gratitude to my supervisors both in China and in France, Prof. Han Kai, Prof. Fabrice Foucher, and my co-supervisor in France Prof. Camille Hespel. Prof. Han Kai helped me to foster the scientific mind to do the research and encouraged me to apply and undertake project during the first two years of my PhD study in China. He is good at individualizing the teaching approach to each people's aptitude, personality, and interest. He opened the chance for me to go to European country and gave me a wonderful experience. His kindness guidance and enthusiasm inspire me to step forward along the way. I would also like to express my appreciation to my supervisor in France, Prof. Fabrice Foucher who gave advice, support, and inspiration during my PhD in France. He is expert in guiding the direction of my thesis and providing good comments when I encountered problems every time. He passed on me the grateful and persistent attitude towards life and academic, which is an invaluable wealth and will equip me for life. Another special huge thank my co-supervisor in France, Prof. Camille Hespel who has paid great efforts in directing my PhD. The thesis would have not been completed without her efforts, comments, wisdom, and encouragement. She taught me another wonderful and interested field of rainbow which I never know before. She not only provided the idea and inspiration of my thesis but also helped me assemble the experimental setup and checked every detail of my manuscript every time. Thanks for her patience to discuss endless about the experimental results and my thesis. Along the journey of my thesis, all of my professors try their best to provide the best resources, guidance, and platform to light my research way. They are the best teachers and researchers in my mind. I am extremely grateful to their support from the bottom of my heart.

Also special thanks to the China Scholarship Council for offering numerous overseas exchange programs and providing financial support during my study in France. A special appreciation to another two important people in helping me apply for the overseas exchange program, Prof. Ying Hang and Ms. Weiqi Zhang. They first

established the collaboration between the Beijing Institute of Technology and the University of Orleans and bridged the cooperation between two labs of Laboratory PRISME at the University of Orleans and the Research Center of Power Machinery in Beijing Institute of Technology. Without their contributions, I would not have had the opportunity to study abroad.

Next, I would like to thank Dr. Xiaokang Ma and M.E. Guoqian Song in guiding me to learn and develop the evaporation model. They taught me the method to establish the model, to process data and plot beautiful scientific figures with different types of simulation tools. I also would like to express my appreciation to M.E. Hao Chen and M.E. Bo Pang for presenting and discussing the evaporation results relating to the high-temperature and pressure conditions, that gives me a fundamental cognition on the to understand the overall evaporation behavior. Next, my thanks go to all the members in the team of Prof. Han Kai. It is a big nice and warm family including M.E. Dongyang Wang, M.E. Tiantian Li, M.E. Zhengda Qi, M.E. Lei Shi, Xiaoling Li, Chaofan Liu, Chang Ke, Bao Lv, Xuanyu Wang, Zhaonian Ye, Shengli Hao, Juntao Han, Ziqian Yang, Hongxia Tan, Yan Zhang, Huize Wang, Haoran Sun. Thanks for all your company along my PhD journey.

Also special thanks to all the members in PRISME lab for helping and supporting my study in France. In particular to mechanical technicians Bruno Moreau and Yahia Haidous who instructed and repaired my experiment setup, solved the issues of hardware and software. This guarantees the completion of my experiment. Specially mentioned go to Anthony Roque whom I spent most of my study time in France with. We shared a lot of life experiences with each other and he was always the first one to encourage me and stand by myside during my research in France. Another thanks to Prof. Yi Yu, Long Yang and Dr. Yu Song for the kind talking and accompany, which makes me to feel at home during my stay in France.

Thanks to all my friends for providing firmly support to continue my study. My Friends in France, Min Cai, Chaoyang Xue, Tian Tian, Xinling Song, Li Jia, Guangguang Ouyang, we spend wonderful time together and organized several brilliant trips together in France. Your appearance made my life in France unforgettable and memorable. Special mentioned my friend who I met in college, Tingting Xu. Although

she continued her study in Japan, she conveyed me the experiences and positive attitude towards oversea life, that taught me how to cherish this oversea learning opportunities and make use of the resources.

Next, I would like to give my thanks to my parents who taught me an independent personality and freedom mind to explore the external world. A special thanks to my fiancé Dr. Wendong Liang who gave enormous mental support along my research journey. We met in freshmen year and fell in love with each other later on. Since then, we have kept the same pace in getting the bachelor's degree, continuing graduate study, determining to proceed on Ph.D. research. He is more of a firm backbone and soulmate for me who can ease my mind when I face obstacles. It is really lucky to have his company throughout my life journey.

Finally, my work is supported by the National Natural Science Foundation of China (Grant No. 91741121). Thanks for the support of the State Key Laboratory of Engines at Tianjin University. The financial support provided by the China Scholarship Council (No.201806030456) for a research visit of the author to the Université d'Orléans is acknowledged. Special thanks to the PSIME lab for providing finance support to extended my study in France. This work would not be successful without being kindly supported for all of them.

ABSTRACT

Droplet transport and evaporation are ubiquitous in many industries and biological applications ranging from engines to thermal management to inkjet printing and so on. The evaporation of droplets in engines decides the formation of fuel vapor, which is critical for the combustion behavior of fuel spray and the emission performance. Meanwhile, the ever-rising emission standard and the environmental-friendly awareness bring up the change of evaporation environment and a number of green alternative fuels. Both the change of fuel type and vaporizing conditions have a significant impact on the droplet evaporation process. The investigations on the evaporation process of different kinds of droplets under complex ambient conditions are essential to achieve clean and efficient combustion. This work applies the experimental and simulation approaches to shed a light on the joint influence of ambient conditions and liquid fuel type on the evaporation behavior of droplets. Firstly, a non-ideal vapor-liquid equilibrium model based on the effective conductivity and diffusivity model has been created and validated. The method incorporates the impact of convection, the interactions between neighboring droplets, temperature-dependent physical parameters, and the polarity differences between different components. Secondly, the droplet evaporation experimental system based on the rainbow technique has been designed and established, which is mainly composed of droplet generation, the high-temperature chamber, and the rainbow image system. An inversion algorithm has been proposed by taking into account the impact of refractive index gradient and shape change of droplet on the rainbow angle. The diameter and temperature distributions of vaporizing droplets under high-temperature conditions have been measured simultaneously for the first time. Furthermore, the evaporation processes of mono and ethanol/heptane binary droplets under different conditions have been investigated with both experimental and simulation methods. The influence of liquid compositions on the preferential evaporation behavior of binary droplet is observed. The results reveal an inversion of the evaporation order of ethanol and heptane components at the droplet surface when the lighter component ethanol dominates the mixture. The comparison of the refractive index between the rainbow measurements

and model predictions confirms the accuracy of the non-ideal vapor-liquid equilibrium model in predicting the preferential evaporation behavior of binary droplet for the first time. The coupling influence of ambient temperature, pressure, and compositions in the liquid phase on the preferential evaporation behavior of droplets is revealed.

Keywords:

Droplet evaporation; Rainbow refractometry; Binary evaporation model; Preferential evaporation; Temperature detection;

CONTENTS

LIST OF FIGURES

LIST OF TABLES

NOMENCLATURE

Acronyms

DGI	Gasoline Direct Injection
SMD	Sauter mean diameter
BTM	Battery Thermal Management
LIF	Laser-induced Fluorescence
2cLIF	Two-color-induced Fluorescence technique
PLIF	Planar Laser-Induced Fluorescence
FSI	Forward scattering interferometry
PDA	Phase Doppler anemometry
MDR	Morphology-dependent resonances
GRT	Global rainbow technique
LMT	Lorenz-Mie's theory
CAM	Complex angular momentum
STR	Standard rainbow technique
ORT	One-dimensional rainbow technique
PRR	Phase Rainbow Refracteometry
GLMT	Generalized Lorenz-Mie theory
GAT	Generalized Airy Theory
CERS	Cavity enhanced Raman scattering
IPI	Interferometric Particle Imaging
ICM	The Infinite Conductivity Model
IDM	The Infinite Diffusivity Model
CLM	The Conductivity Limit Model
DLM	The Diffusivity Limit Model
ECM	The Effective Conductivity Model
EDM	The Effective Diffusivity Model
CFD	Computational Fluid Dynamics
VOF	Volume of Fluid
LS	Level-Set

EOS	Equations of State
PR EOS	Peng-Robison equations of state
RK EOS	Redlich-Kwong equations of state
SRK EOS	Soave-Redlich-Kwong equations of state
DCM	Discrete Component Model
UNIFAC	Universal quasi-chemical Functional Group Activity Coefficients
VLE	Vapor-liquid equilibrium
FFT	Fast Fourier Transform
NI	Non-ideal equilibrium model
I	Ideal equilibrium model
ETH25	Initial volume fraction of ethanol in the mixture is 25%
ETH50	Initial volume fraction of ethanol in the mixture is 50%
ETH75	Initial volume fraction of ethanol in the mixture is 75%

Constants

f_1	Focal length of first lens=150 (mm)
f_2	Focal length of second lens=50 (mm)
M	Magnification ratio=1.17
S_1	The distance from the droplet to the front principal plane of the lens=278 (mm)
S_2	The distance between camera and the first lens=70 (mm)
c	Constants defined by $c = \alpha_1 / \alpha_2$
α_1	Constants before the angle corresponding to the first extreme value = 1.0874
α_2	Constants before the angle corresponding to the second peak = 3.4668
R	Ideal gas constant =8.3100598 ($J \cdot K^{-1} \cdot mol^{-1}$)
π	Mathematical constant=3.1415926
$A_1\ A_2\ A_3\ A_4$	Constants in the dimensionless spacing parameter, A_1=0.431, A_2=0.179, A_3=0.5, A_4=5.076

Greek Alphabets

λ	Wavelength of incident rays (μm)
θ	Scattered angle of droplet around rainbow angle-degree (°)
θ_{rg}	Rainbow angle-degree (°)
θ_v	Scattering angle as a result of variable refractive index-degree (°)
θ_1	The angle corresponding to the first peak-degree (°)
θ_2	The angle corresponding to the second peak-degree (°)
$\theta_{rg,1}$	Rainbow angles for spheroidal particles-degree (°)
$\theta_{rg,2}$	Rainbow angles for spherical particles-degree (°)
$\Delta\theta_{rg}$	The deviation of rainbow angle spheroidal and spherical droplets-degree (°)
τ	Incident angle-degree (°)
τ'	Refraction angle-degree (°)
τ_p	The complements of incident angles-degree (°)
τ_p'	The complements of refraction angles-degree (°)
τ_{rg}	Rainbow incident angle-degree (°)
ε_1	Variable relates with the complements of incident and refraction angles
χ_1	Refraction angle considering the variable refractive index - degree (°)
ρ_l	Density in the liquid phase ($kg \cdot m^{-3}$)
ρ_∞	Density of air-flow ($kg \cdot m^{-3}$)
ρ_v	The vapor density ($kg \cdot m^{-3}$)
δ_{T0}	Thickness of thermal boundary layer
δ_{M0}	Thickness of mass boundary layer
μ_g	The viscosity of the vapor
γ_i	Activity coefficient of component *i*
$\hat{\varphi}_{i,sat}$	The fugacity coefficient at the condition of saturated vapor state
$\hat{\varphi}_{i,vs}$	The fugacity coefficient at the condition of vapor state
Ψ_i	Poynting factor

$\nu_k^{(i)}$	The number of k-type structural group
Γ_k	The active coefficient of group k in the mixture
$\Gamma_k^{(i)}$	The active coefficient of group k in pure liquid
α_{ij}	Separation factor
ξ	Droplet unsphericity

Latin Alphabets

u_D	Jet velocity ($m \cdot s^{-1}$)
f_G	Excitation frequency (kHz)
D	Pinhole diameter (μm)
d	Droplet diameter (μm)
P_{inj}	Injection pressure (bar)
P_{amb}	Ambient pressure (bar)
Q	Volume flow rate ($m^3 \cdot s^{-1}$)
A	Cross section area of pinhole (m^2)
p	Rays type
n	Refractive index
n_e	Refractive index of the environment
A_i	Airy integral
z	Argument
h	Variable relates with ray type and refractive index
$\tilde{r}_m$	The minimal distance of the light ray from the droplet center
$\tilde{r}$	non-dimensional particle radius
$n(\tilde{r})$	The profile of refractive index inside the particle
n_c	The refractive index at droplet center
n_s	The refractive index at droplet surface
m	Polynomial order
n_{eq}	The equivalent refractive index
T	Temperature (K)
T_{amb}	Ambient temperature (K)
$r^{(LL)}$	The specific refraction
Y	Mass fraction of component

X	Molar fraction of component
$r_i^{(LL)}$	Specific refraction of the i-th pure component
D_{airy}	The airy diameter
D_{ripple}	The ripple diameter
F	Angular frequency
F_1	Angular frequency coming from the Airy fringes
F_2, F_3	Angular frequency relates to the ripple structure
F_{ripple}	Ripple frequency
F_{Airy}	Airy frequency
U	Droplet velocity ($m \cdot s^{-1}$)
$U\infty$	Velocity of air-flow ($m \cdot s^{-1}$)
r_s	Droplet radius (m）
C_D	The drag coefficient
Re_g	Reynold number in the gas phase
$\dot{m}_d$	The mass diffusion rate ($kg \cdot s^{-1}$)
$p_{i,sat}$	The saturated vapor pressure (bar)
B_M	Spalding mass transfer number
B_T	Spalding heat transfer number
D_v	Diffusion coefficient ($cm^2 \cdot s^{-1}$)
k_g	The conductivity of the gas-vapor mixture thermal conductivity ($W \cdot m^{-1} \cdot k^{-1}$)
$c_{p,v}$	The specific heat capacity of vapor specific heat ($J \cdot kg^{-1} \cdot K$)
$c_{p,l}$	Specific heat of the liquid phase
L	The latent heat of vaporization ($J \cdot kg^{-1}$)
Sh_0	The Sherwood number of non-evaporating droplet
Nu_0	The Nusselt number of non-evaporating droplet
Sh^*	The modified Sherwood number
Nu^*	The modified Nusselt number
Le	Lewis number
k_{eff}	Effective conductivity coefficient
D_{eff}	Effective diffusivity coefficient

Q_l	Instantaneous heat flux absorbed by the liquid phase
B_{ii}	Virial coefficients of pour species
B_{ij}	Cross-section coefficient
$B_{M,V}$	Coefficients linking the pure and cross section
r_i	Relative Van-der-Waals volume
q_i	The surface area
R_k	The volume of each group
Q_k	The surface area of each group
K_i	The equilibrium constant of species *i*
K_j	The equilibrium constant of species *j*
K_v	Evaporation constant
$K_{V,NI}$	Evaporation constant for non-ideal cases
$K_{V,I}$	Evaporation constant for ideal cases
C	Dimensionless spacing parameters
n_{dif1}	Refractive difference between droplet surface and center
n_{dif2}	The difference of the resulting equivalent refractive index and the refractive index at droplet surface

1. Introduction

1.1 Background of droplet evaporation

Droplet transport and evaporation are ubiquitous in many industries and biological applications ranging from engines to thermal management to inkjet printing and so on. Given its importance, the evaporation behavior together with the influencing factors and subsequent outcomes have received great attention in different areas.

Muddapur et al. [1] explored the spray characteristics generated from the multi-hole injector in the Gasoline Direct Injection (GDI) engine both experimentally and numerically. The infinite conductivity droplet evaporation model was incorporated into the ANSYS together with the corrections of convection and the neighboring droplets interactions. The dependence of global Sauter means diameter (SMD) on ambient temperature and pressure had been analyzed, which influences the succeeding combustion and emission performance.

The evaporation of plasmonic droplets is fundamental for the solar-to-heat system. Liu et al. [2] explored the solar water evaporation dynamics through a hanging droplet containing the nanoparticles. They demonstrated the effectiveness of enhancing solar water evaporation by coupling plasmonic nanoparticles within a mesoscale droplet. The gold nanoparticles greatly improved photon absorption and promoted surface evaporation.

Coolant evaporation provides a good solution for battery thermal management (BTM) to achieve the ideal performance and lifespan of a Li-ion battery. As stated by Lei et al. [3], a water spray cooling system cooled down the maximum temperature of Li-ion battery by 29.2 °C at a large discharging current of I_d=25 A. Also, the spray conditions had a decisive impact on the performance of the BTM system. For example, increasing airspeed from natural convection to 6.3 m/s effectively diminishes the battery-surface average temperatures from 50.5°C to 44.2°C. Yang et al. [4] investigated the impacts of water flow rate, water droplet size, and air velocity on the battery performance. The results revealed the importance of the evaporation of droplets on determining the subsequent spray state and the cooling performance of batteries.

Hatte et al. [5] studied the evaporation behavior of an ordered array of droplets, which has extensive applications in inkjet printing and photonics. A theoretical model accounting for the interactions between droplets closely placed inside the array had been proposed and validated with the experimental data.

Recently, the droplet evaporation process has drawn renewed attention in the biological area regarding the direct or indirect transmission of the virus. Bhardwaj et al. [6] analyzed the drying time of respiratory droplets from a COVID-19 infected subject by using a diffusion-limited evaporation model of a sessile droplet. The results indicated that the survival time of the virus is determined by a couple of influencing factors, including the droplet volume, ambient temperature, and humility.

The previous literature presents the universal yet paramount role of droplet evaporation in different kinds of practical scenarios, nevertheless, evaporation is a complex phenomenon, and the underlying mechanism influencing the evaporation characteristics is far from being fully understood.

1.2 Experimental researches of droplets evaporation

To comprehend the heat and mass transfer process of droplets regarding its importance in practical applications, numerous researches have been done up to now. The section reviews the development and perspective of the investigations on droplet evaporation from the point of experiment and simulation. For experimental investigations, stationary droplets suspended with wire or with the help of acoustic/optical/electrical approaches and free-falling moving droplets are the most prevalent configurations of droplets [7]. Herein, the series of suspension fiber and another category of the free-falling method is of interest and introduced.

1.2.1 Vaporization with suspension wire

A host of experimental researches adopted the suspension technique to study the droplet evaporation process up to now. In general, a droplet is produced by a syringe under room temperature conditions and transferred to a high-temperature environment soon afterward with the help of the suspension wire. Without being exhausted listed, in the year 1952, Ranz and Marshall [8] conducted experiments of a suspended single

water droplet with a diameter of 0.6-1.1 mm under an ambient temperature up to 220°C and proposed the standard heat transfer equations. Later, Renksizbulut and Yuen [9] looked into the evaporation of suspended liquid droplets under high convective temperature conditions of 1000 °C in 1983. They analyzed the negative impacts of evaporation on the heat transfer rates at higher temperatures. Recently, Manjunath et al. [10] adopted the suspension method to experimentally investigate the evaporation process of diesel and biodiesel mixtures. The droplet with an initial diameter varying from 1.9 to 2.1 mm is suspended with a quartz wire of 0.5 mm diameter. The results revealed a significant influence of the physical properties of individual components on the overall evaporation behavior of a multi-component droplet. Adding more diesel into the blends enhances the evaporation rate and shortens the droplet lifetime because diesel has a lower boiling point than biodiesel. More recently, the evaporation of heptane droplets under turbulence conditions was studied by Verwey and Birouk [11] with the suspension technique. Droplet with an initial diameter of 500±10 μm locates at the intersection of two microfibers. They focused on the impact of turbulence intensity on the evaporation rate and droplet lifetime.

Despite using the suspension technique, the experimental configurations of those studies differ a lot, as displayed in **Figure 1.1**. Firstly, switching the droplet from a room temperature condition to a high-temperature environment, the major solution is a fixed heating chamber and a moving droplet and suspension wire [12]. On the contrary, some other researchers designed a moving chamber rather than changing the position of the droplet to prevent the falling of liquid during the droplet motion [13]. Secondly, suspending droplet mainly has three configurations, including vertical fiber, horizontal fiber, and cross-fiber, as shown in **Figure 1.2**. In the case of vertical fiber, the diameter of the fiber is normally no less than 0.1 mm together with a larger ball at the end of the wire tip to give enough support for droplet, which induces a greater influence on the evaporation. The horizontal case has the smallest contact area between fiber and droplet yet the stable suspension of the droplet is difficult. The last method can not only suspend droplet firmly but also maintain the droplet shape at nearly spherical compared with the other two methods generating an ellipsoid droplet [14].

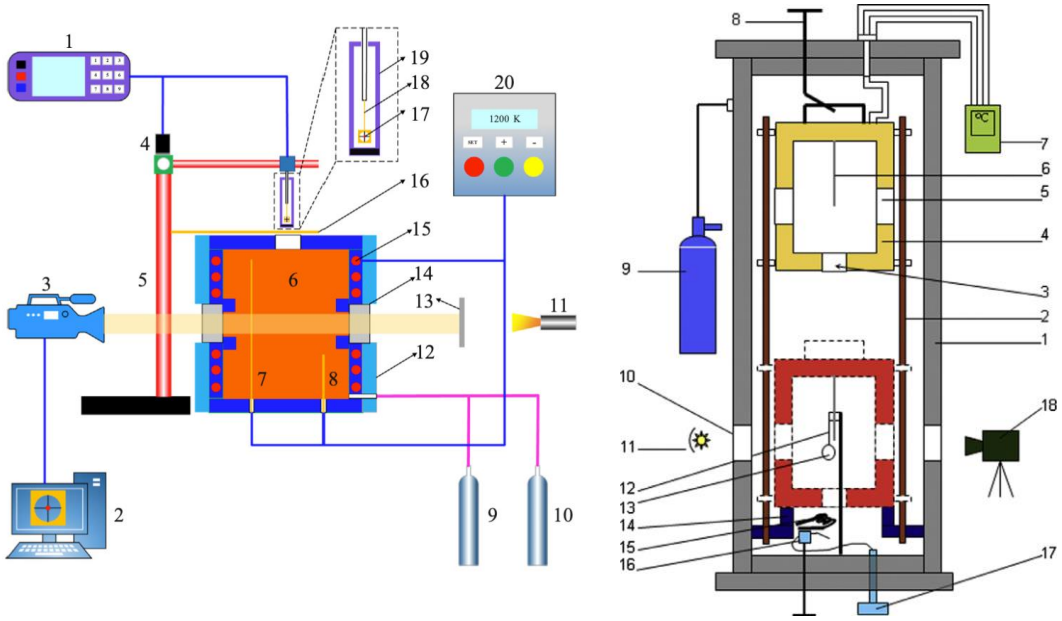

(a) Motion of droplets [12] **(b) Motion of chamber [13]**

Figure 1.1 Comparison of different experimental setup. (a): (1) Stepper motor controller, (2) computer, (3) high-speed video camera, (4) stepper motor, (5) ball screw moving device, (6) heating chamber, (7) thermocouple 1, (8) thermocouple 2, (9) nitrogen vessel, (10) air vessel, (11) LED backlight, (12) insulation layer, (13) scattering film, (14) quartz glass, (15) heating wire, (16) thermal baffle, (17) droplet, (18) support framer, (19) thick quartz tube, (20) thermocouple controller. (b): (1) Pressure vessel, (2) guide bar, (3) furnace entrance, (4) electric furnace, (5) quartz glass window on furnace, (6) thermocouple, (7) temperature controller, (8) lever, (9) nitrogen vessel, (10) quartz glass window on pressure vessel, (11) LED backlight, (12) silicon carbide fiber, (13) droplet, (14) shock absorber, (15) heating wire, (16) droplet maker, (17) plunger micropump, (18) CCD camera.

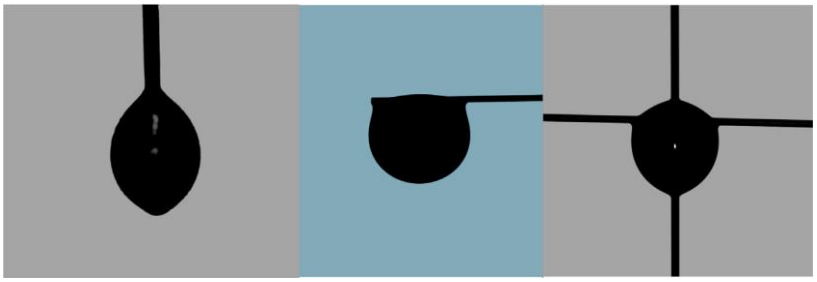

Figure 1.2 Different droplet suspension methods [12].

Furthermore, the materials of suspension fiber can be different, as compared in **Table 1.1**. The widely adopted suspension wires include silica (SiO2), silicon carbide (SiC), glass, quartz, and thermocouple. Different materials have diverse thermal

conductivities and heat transfer abilities. A common cognition is that the usage of suspension wire inevitably introduces additional heat conduction through fiber and impacts the droplet evaporation process. Yang et al. [15] examined the influence of SiO2 fiber by both experimental and simulation approaches. The results revealed the promotion of evaporation rate due to the presence of fiber. In addition, the heat conduction through the fiber is more pronounced when the ambient temperature is relatively lower or the diameter ratio between fiber and droplet is large. Similarly, thermocouples promoted the evaporation rate as investigated by Rehman et al. [16]. It is found that a larger thermocouple diameter leads to a faster evaporation rate and a higher equilibrium temperature. Han et al. [17] separately figured out the influence of thermocouple and quartz fiber on evaporation with both experimental and numerical methods. It is demonstrated that increasing the diameter of the suspension wire intensifies the increase of the evaporation rate and the decrease of droplet lifetime. Additionally, despite the thermocouple can measure the temperature of the suspended droplet, the evaporation rate of droplets suspended by a thermocouple is larger than that suspended with quartz fiber as a result of high thermal conductivity.

As reviewed above, the influence of wire on the evaporation rate of droplet, droplet lifetime, and heating process in the liquid phase is inevitable in the suspension technique. Apart from that, despite some researches stating that fiber cannot induce the micro-explosion when the temperature is low or the diameter of the fiber is small (less than 20 μm) [18], Wang et al. [12, 19] already proved that the usage of suspension wire leads to the occurrence of micro-explosion phenomenon at a high-temperature condition. At the same time, the droplet evaporation takes place without a wire in real applications. Besides, the average initial droplet diameter with suspension technique is at around 1 mm as listed in **Table 1.1**, which is relatively large compared to the droplets inside a spray (order of 100 μm). In terms of the above factors, the suspension technique is not the optimum choice to do the research and it is necessary to conduct the investigation of droplet evaporation in a more realistic situation.

Table 1.1 Comparison of different experimental parameters.

Sequence number	Initial droplet diameter [mm]	Fiber arrangement	Ambient temperature [K]

1 [20]	0.5-1.5	Single vertical silicon carbide (SiC) 142 μm	923-1073
2 [13, 21]	1.0±0.1	Single vertical SiC fiber 100 μm	373-1073
3 [22]	0.8-0.91	Single vertical SiC fiber of 120 μm with a large bead of 200 μm	423-823
4 [14]	0.55-0.8	Single vertical SiC fiber of 106-181 μm	300-997
5 [15]	0.7-1.0	Horizontal or vertical SiC fiber of 50, 150, and 300 μm	490-750
6 [23]	0.40-0.55	Cross of two fibers (alumina and silica) with a glass bead (100 μm)	400-900
7 [24]	1.21-1.23	Regular K-type thermocouple of 127 μm	473-773
8 [12, 25]	~0.84	Cross arrangement of two fibers of quartz, iron and copper with a diameter of 80-150 μm	673-973
9 [26]	0.95-1.19	Irregular K-type thermocouple of 70 μm	573-823

1.2.2 Free-falling droplets configurations

The transient measurement of the droplet evaporation process under practical-like conditions is attractive. The configuration of a free-falling droplet stream is more realistic than the suspension method concerning the motion and diffusion of droplets inside a spray. Another advantage of the free-falling method is the complete removal of the suspension wire. Therefore, the droplets are free of any shape distortion and additional heat conduction. Furthermore, a free-falling configuration is capable to achieve the measurement of a smaller droplet with a length scale of hundred micrometers. This droplet size is more comparable to the droplet sizes in a spray. Regarding this, the free-falling method has been extensively adopted to investigate the evaporation and burning process of droplets.

The instantaneous and accurate capture of a moving droplet is a major challenge accompanied by this configuration as the position of the droplet changes over time. Deprédurand et al. [27] simultaneously measured the variation of droplet size and mean temperature of six kinds of droplets with non-intrusive optical techniques. A

monodisperse droplet stream was generated by the piezoceramic. Droplet temperature is measured through the two-color-induced fluorescence technique (2cLIF) and droplet size is evaluated with the forward scattering interferometry (FSI). The initial velocity and diameter of the droplets are 10 m/s and around 110 μm, respectively. Later, they combined the 2cLIF with the shadow imaging to characterize the evaporation of droplets [28]. The results proved the potential of 2cLIF on measuring the temperature of mono-component and multi-component droplets.

Hillenbrand et al. [29] performed the experiments of binary alkane/ethanol free-falling droplets with a high-resolution Raman spectroscopy setup, which focuses on the mixture formation and component-by-component evaporation. It is validated that Raman spectroscopy is capable of evaluating the composition of gaseous phase nearby droplets. The burning characteristics of acetone-butanol-ethanol and diesel blend droplets were experimentally investigated by Han et al. [30] with the free-falling method. A CCD camera was adopted to capture the burning process of the droplet with an initial diameter of about 200 μm. The droplets at different vertical positions were captured by adjusting the CCD to the same vertical level and repeating the experiment, which requires high reproducibility of the droplet generation. The results validated the feasibility to investigate the burning process of droplet with this method and the micro-explosion was observed under high-temperature conditions, which greatly shortens the burning duration. Volkov et al. [31] applied the thermocouples and Planar Laser-Induced Fluorescence (PLIF) to capture the temperature of droplets, films, and aerosols of water under different heating schemes of 20 to 800 °C. The Rhodamine B dye was the fluorophore. It is concluded that the non-contact optical techniques contribute good visions of the existing mechanisms of warming-up, evaporation, boiling, and breakup of the liquid droplets.

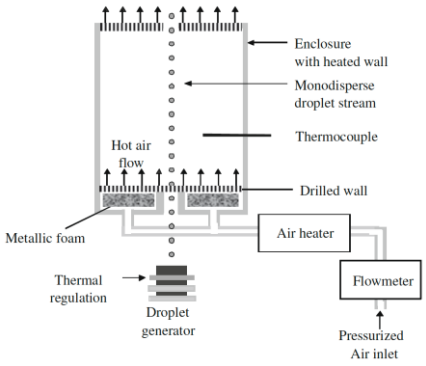

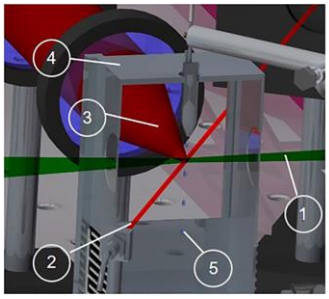

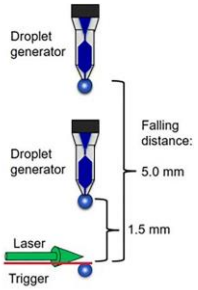

(a) Schematic figure of the droplet generation [27, 28]

(b) Droplet generation and chamber [29]

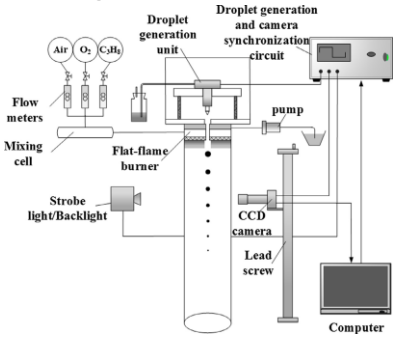

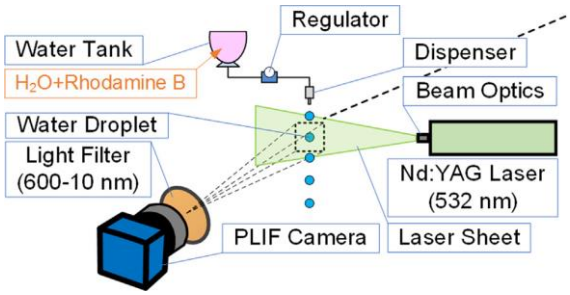

(c) Schematic of the free-falling experimental setup [30]

(d) Scheme of the experimental setup [31]

Figure 1.3 Schematic figures of free-falling technique.

In terms of this new configuration, the interactions of neighboring droplets inside the droplet stream play a significant role in affecting the heat and mass transfer process, which is worth a detailed analysis. The spatial arrangement of droplets is well described by a dimensionless spacing parameter which is defined as the ratio of the distance between neighboring droplets and droplet diameter. In general, the interaction between droplets produces appreciable influence when the dimensionless spacing parameter is smaller than about 10. A smaller dimensionless spacing parameter gives rise to a smaller normalized heat and mass transfer number, which reveals the negative influence of neighboring droplets [27]. Also, the volatility of liquid fuel has a noticeable influence on the interaction mechanism [28]. It is demonstrated that the influence of droplet interactions on the heat and mass transfer rate for low-volatile droplets is more evident for the high-volatile droplet. The Stefan flow surrounding the droplet can provide a clue

for this phenomenon. One assumed that the Stefan flow resulting from evaporation protects the droplet from the perturbation in the outer environment. For low-volatile droplets, the formation of vapor film takes a longer time. Accordingly, it is more sensitive to external conditions and more likely to be affected the neighboring droplets. Li et al. [32] evaluated the evaporation of monodisperse ethanol droplet stream with a combined phase rainbow refractometry and high-speed microscopic shadowgraph. They quantified the influence of droplet interactions by comparing the experimental measurements with the model predictions. The accuracy of different correlations between the dimensionless spacing parameter and the evaporation rate ratio was examined. A more refined regression curve with a similar form had been suggested.

1.3 Optical measurements of moving droplets

1.3.1 Different optical methods

The comparison made in former section reveals that the optical method is prevail for the investigation of moving droplets because of its high accuracy and various possibilities. Some common optical methods include the Phase Doppler Anemometry (PDA), Morphology-dependent resonances (MDRs), Laser-induced Fluorescence (LIF), and Rainbow Refractometry. Each technique has merits and drawbacks judging by the basic principle.

Lase-induced fluorescence (LIF) [33, 34] captures the fluorescence signal coming from the tracer, which predicts the information of concentration and temperature. In principle, the addition of an organic fluorescent dye into the liquid fuel is necessary in order to produce the fluorescence spectra. This is how it works to measure the temperature of liquid droplets. However, it is inevitable to modify the properties of liquid fuel by adding the molecular tracer. Therefore, the effect of the tracer has to be examined and minimized when conducting the experiment. Apart from that, the calibration process is necessary for this method as the signals change with pressure, temperature, and chemical compositions at the same time.

Phase Doppler anemometry (PDA) [35] can simultaneously measure the droplet velocity and size of spherical particles. It is a non-intrusive technique performed at the

intersection of two laser beams. Generally, the signals coming from the interactions of the beam fringe patterns and droplets are recorded by two detectors. The droplets' velocity, droplet diameter, and the refractive index can be respectively extracted from the frequency and the phase shift information of the signal. Nevertheless, this method suffers from the lower accuracy of the refractive index with the limitation to the second digit.

Morphology-dependent resonances (MDRs) [36] are eligible to extract both particle size and refractive index of perfectly spherical droplets. The principle of this method is to analyze the internal reflection scattering light spectra from a spherical droplet. The droplet diameter together with the variation of diameter relates to the resonance peak. This method is especially advantageous for droplets with a maximum diameter of about 80-100 μm. The resolution of diameter variation can be as small as $5\times10^{\wedge-5}$ of droplet radius [37]. The major drawback is the high requirement for the perfect spherical shape of the particle.

The final category, i.e., the rainbow refractometry is especially attractive because of the non-intrusive and tracer-free features. Without being exhaustive listed, some significant contributions have been made by Anders et al. [38], Van Beeck [39], and Sankar et al [40]. This method captures the scattering images of transparent droplets illuminated by the incident rays at the nearby of the rainbow angle, from which extracts the useful information of droplet diameter and refractive index. The rainbow angle is determined by the refractive index whereas the shape of the scattering light intensity curve relates to the particle size. This technique has been widely adopted in the configurations of a single droplet, droplet stream, and droplet spray. In addition, this technique is applicable to the non-spherical droplets as well by adopting the global rainbow refractometry (GRT) [41].

Compared with the configuration of the backlight shadowgraph technique to record the size change of suspended droplets, the combination of the rainbow technique with free-falling droplets can accurately measure multiple parameters including the droplet size, temperature, or concentration during the evaporation process. Those advantages are not only helpful in revealing the underlying mechanism of the evaporation process but also useful for model validation. Accordingly, this work adopts

the rainbow technique to investigate the evaporation process of droplets stream regarding its potential and accuracy.

1.3.2 Rainbow refractometry

The rainbow phenomenon in nature is a common scenery in the sky, which can be observed when rain and sun are present together as shown in **Figure 1.4**. The physical explanation of this phenomenon was introduced by Ren Descartes in 1637 [42]. The rainbow technique leans against the interaction between the transparent droplets with a spherical shape and the incident light. To describe this interaction and the succeeding outcomes, it is practical to split a beam of light into different types of light rays. The light path of each ray is followed according to the laws of geometrical optics. In this context, the Descartes-Snell and Fresnel laws are used to compute the direction and intensity of the reflected and refracted rays when the rays impinge on the interface. To facilitate the discussion, the rays leaving the particle are named according to Van de Hulst's notation [43]:

For p=0 is the externally reflected ray;

p=1 is the refracted twice ray;

p=2 is the ray experiencing one internal reflection and two refractions;

p=3 is the rays experiencing two internal reflections and two refractions;

Similarly, p=n for the rays experiencing n-1 internal reflections and two refractions;

In the framework of geometrical optics, a rainbow corresponds to the rays experiencing one internal reflection and two refractions named p=2, as exemplified in **Figure 1.5**. In addition, the externally reflected ray of p=0 has interference with the p=2 rays, which modifies the characteristics of the scattering rainbow patterns. therefore, the rainbow technique mainly focuses on two types of rays p=0 and p=2. The geometrical rainbow angle (θ_{rg}) is the scattering angle position corresponding to the rays of p=2. Noting that each type of liquid has a different rainbow angle, which only depends on the refractive index. For example, water has a rainbow angle of 138° at atmospheric pressure.

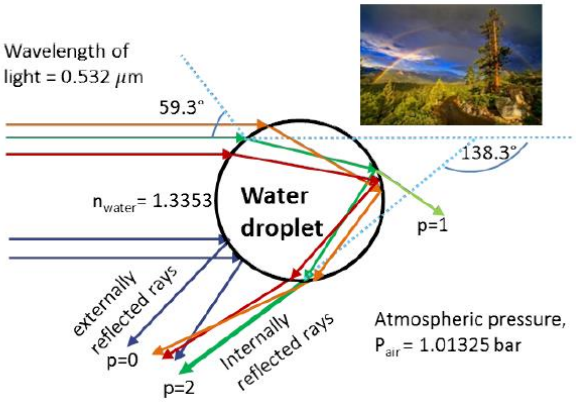

Figure 1.4 The optical paths of the light rays pass through a water droplet [44].

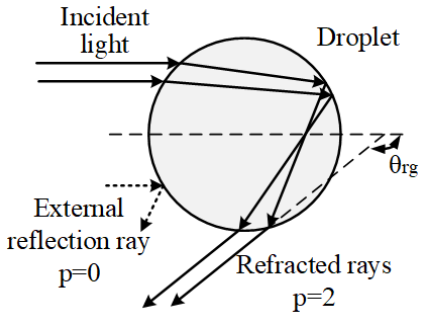

Figure 1.5 The schematical optical paths of the p=2 and p=0 rays.

Nevertheless, the real structure of the rainbow is complex. To interpret and comprehend the scattering light patterns, simulating the scattering light patterns from droplets is indispensable. Several theories are available to achieve this function such as Lorenz-Mie's theory, Airy theory, Debye theory, the complex angular momentum (CAM) method, the catastrophe theory, and so on [45]. The Airy theory was firstly introduced by George B. Airy to simulate the rainbow patterns. It is based on geometrical optics by taking into account the diffraction among different rays. The major drawback of this method is the insufficiency to consider the vector aspect because of its scalar feature. In addition, this method only has accurate prediction at the nearby of the rainbow angle. With the increase of the scattering angle, the prediction by the Airy theory has an obvious deviation in the rainbow positions compared with the results of more rigorous methods. Lorenz-Mie's theory (LMT) is the most rigorous simulation of the scattering light patterns based on the solution of Maxwell's equations [46]. All of the interactions between the incident light and the transparent particle have been taken into consideration. Apart from that, Debye [47] formulated a different way for the

same problem. The expressions obtained with the LMT can be rewritten with different contributions attributable to waves partially reflected and partially transmitted by the particle. In this way, the contribution of each interaction is separated [48]. Nevertheless, the essence of the Debye theory is the same as the LMT with the form of summations, which is computational-demanded and unrealistic for the post-processing process. Another alternative approach is the complex angular momentum theory (CAM theory) developed by Nussenzveig. This method originates from Debye's theory but it is less time-consuming by converting the series into integrals through mathematics formula. They classified different equations depending on the angular regions of interest [49].

An example of the scattered light nearby the rainbow angle evaluated by the Lorenz-Mie theory is displayed in **Figure 1.6**. A green laser (wavelength of 0.532 microns) illuminates the ethanol particle. The diameter and refractive index of the particle are 100 microns and 1.365, respectively. As can be seen, two zones of high intensity can be easily presented. The primary rainbow, resulting from the interference between first internal reflections (p=2). The second rainbow is created by the second internal reflection (p=3). The gap between the first and second rainbows with a low light intensity is Alexander's dark band, which comes from the external reflections. In addition, it can be observed there are oscillations of low and high and frequencies in the first and second rainbows regions. For the first rainbow, the first oscillation having the highest intensity is called the Main rainbow peak and the others are denoted as supernumerary bows (Airy fringes). The high-frequency fringes are called 'ripple structure', which is superimposed on the Airy fringes. Those fringes result from the interference between the external reflection and internal reflection light [50]. The rainbow position and rainbow shape are determined by the refractive index and droplet diameter, respectively. Meanwhile, the refractive index relates to the temperature or the compositions in the liquid phase. Therefore, for the typical scattering light of the rainbow, the most important two parameters are the primary rainbow angle and the distance of airy fringes. The relationship between the rainbow patterns and the refractive index value as well as the droplet size has attracted a lot of researches in the droplet evaporation field, as reviewed in the pioneering work of the Stuttgart University team [51-54].

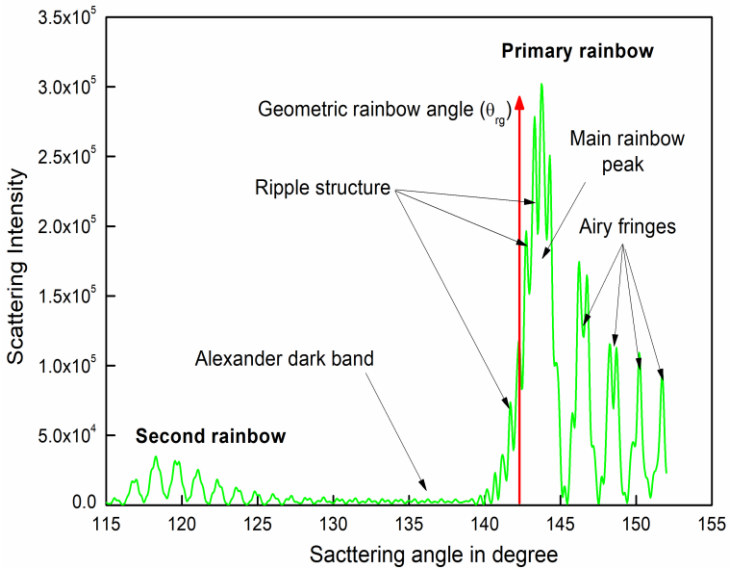

Figure 1.6 The scattering intensity curve evaluated by the Lorenz-Mie theory.

The point one should keep in mind is all of those methods abovementioned are suitable for the direct simulation of elastic-type scattering phenomena of a spherical particle and a plane wave. They can compute similar light patterns as illustrated in **Figure 1.6**. However, in practice inversion procedures where the comparison between the numerical patterns and experimental data is necessary, not all of them are suitable. Therefore, it is necessary to tell the difference between those methods and grasp their fields of validity and the equations which govern them.

1.3.3 The application of rainbow refractometry

This technique can measure the particle diameter and temperature simultaneously by capturing the scattering light patterns as indicated in the last subsection. A variety of rainbow technique configurations are available now, including the standard rainbow technique (STR), global rainbow technique (GRT), and one-dimensional rainbow technique (ORT) for both standard and global one. STR is suitable to measure the evaporation of a single droplet or a droplet stream. The typical scattering image of this technique is shown in **Figure 1.7**(a) with a distinct ripple structure. Without being exhaustive listed, the pioneering work was conducted by Roth et al.[52, 53]. Then, Saengkaew et al [50] proposed a signal processing algorithm by accounting for the impact of the ripple structure, which greatly improved the measurement precision. The accuracy of the data-processing after improvement is up to 0.01 μm for diameter and

0.0001 for refractive index, respectively. Recently, Promvongsa et al. [55] investigated the evaporation of mono-dispersed droplets with the rainbow technique under the room temperature of 20°C conditions. The results validated the possibility of this technique in measuring nanometers change of the particle with a diameter of 80 μm.

The GRT is regarded as an extension of SRT with the measurement volume from a single droplet to a group of droplets or sprays. Compared with standard rainbow, the scattering light obtained by GRT can be taken as the superimposition of rainbow patterns of a host of droplets. As a consequence, the ripple structure is removed as shown in **Figure 1.7**(b). Van Beeck et al. [39] firstly introduced GRT to examine the particle size and temperature. They carried out the experiments at some particular conditions and got the size distribution and average refractive index of droplets. The main limitation of his work is the lower accuracy restricted by the post-processing procedure. Later, Saengkaew et al. [50] introduced an inversion strategy and improved the accuracy of this method in deciding the size distribution and refractive index with the accuracy of 0.0001.

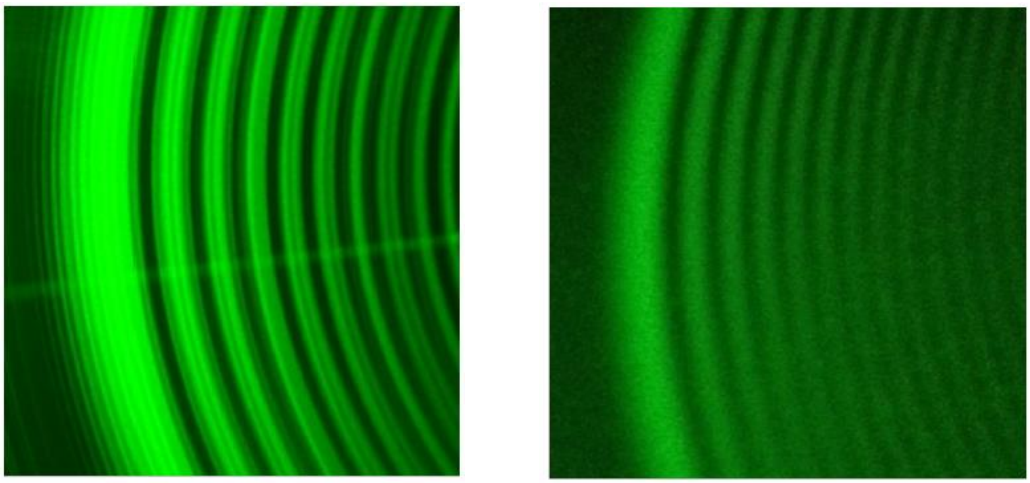

(a) Standard rainbow patterns **(b) Global rainbow patterns**

Figure 1.7 Typical rainbow patterns by different techniques. (a) is the scattering image of mono-disperse water droplets produced from a pinhole size of 50 μm; (b) is the scattering image of nearly mono-disperse water droplets produced from a pinhole size of 100 μm [44].

Although the SRT and GRT are powerful tools in diagnostics of droplets and spray, they are restricted by the problem of a small measurement volume and the measurement at a fixed point. To address this problem, recently a bunch of researches have been done

by the team of Wu et al. [32, 56-61].

Firstly, Wu et al. [56] developed an experimental configuration named the one-dimensional rainbow technique (ORT) on the basis of the GRT. Compared with the configuration of the global rainbow technique, the main modifications to the rainbow system are the addition of slit apertures and a laser light sheet. The laser sheet illuminates more droplets resulting in a larger measurement volume. The slit apertures can turn the single point rainbow signal into a ribbon. Accordingly, the rainbow signal from different heights can then be recorded to yield a one-dimensional image. It was proved that this new system had a good performance in the simultaneous measurement of droplet size and refractive index in the liquid phase. Apart from that, it had the feasibility and potential in measuring the evaporation and combustion of spray. Later, they proposed an alternative ORT system (named ORT2) using the Fourier domain filtering to facilitate the angular calibration [57]. The main difference of this system compared with the former one was the variation of the horizontal slit. They moved the horizontal slit from the position before the first lens to the focal plane of the first lens. This not only simplifies the angular calibration process but also filters the interference of the light without impinging perpendicularly. It was indicated that the new configuration can provide reliable measurement of refractive index and droplets size. After that, Wu et al. [58, 59] introduced a new processing algorithm by taking advantage of the phase shift from the scattering patterns. Accordingly, one-dimensional phase rainbow refractometry (PRR) was named after that. The experiment configuration was generally the same as ORT2. The difference was that the inversion algorithm has been improved by using the phase shift of ripple structures. It had an accurate measurement for a nanoscale variation of diameter with an initial droplet diameter of a micrometer scale. Soon afterward, they adopted the configuration of PRR and the improved inversion algorithm to investigate the evaporation behavior of the n-heptane droplet stream [60]. The experiments were performed under high-temperature and normal pressure conditions. The droplet diameter, refractive index, and the variation of droplet diameter of n-heptane during the evaporation process were simultaneously measured by using the PRR technique. More recently, Li et al. [32] combined two types of measurement methods to explore the evaporation behavior of a stream of free-falling

ethanol droplets. The phase rainbow refractometry (PRR) was adopted to measure the evaporation characteristics of droplets whereas the high-speed microscopic shadowgraph captured the images of the droplet stream. They quantified the impact of interactions between neighboring droplets inside the stream. In addition, to explore the application of the rainbow technique to characterize droplets containing dispersed insoluble particles, Li et al. [61] proposed a new method based on the ratio of second-order refraction and reflection components in the rainbow signal. The scattering light patterns were captured by the standard rainbow refractometry (STR). The refractive index, the diameter of the host droplet, and the colloid concentration of suspension particles were simultaneously obtained. This extends the industrial applications of the rainbow technique.

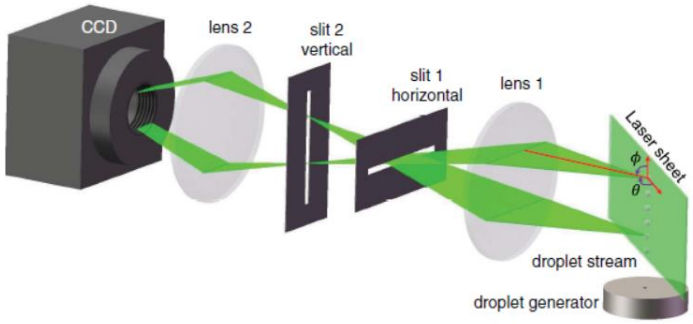

Figure 1.8 Schematic of the new one-dimensional rainbow system [58].

1.3.4 Impact of temperature and refractive index gradient

In general, the condensation, evaporation, or combustion of droplets encountered in practical applications are inhomogeneous with a temperature or concentration gradient in the liquid phase. For instance, if a cold droplet travels to a hot environment, the droplet gets heated from the surface to the center gradually rather than an instant warm. Likewise, if it is a multi-component droplet, each composition has a different reaction time on the change of environment.

A considerable temperature gradient inside the droplet had been evaluated and measured in [62]. Despite that, general conclusions and a systematical comprehension have not been obtained on revealing the relations between the temperature gradient and the evaporation characteristics. To address this issue, Snegirev [63] analyzed the

temperature gradient inside different kinds of droplets by varying ambient temperature with the numerical method. Three characteristic time scales and two dimensionless criteria were adopted to do the comparative study. The overall results showed that the liquid with high volatility is more sensitive to the temperature gradient in the liquid phase at a higher ambient temperature. Despite that the temperature gradient has little influence on the droplet lifetime, it has a remarkable impact on the heating process especially at the initial evaporation stages with a maximum deviation of about 50 K. Consequently, the necessity to consider the temperature gradient in the liquid phase has been substantiated.

The arising inhomogeneous temperature together with the composition gradient inside the droplet leads to the non-uniform refractive index distribution. Accordingly, this can significantly modify the light trajectory in the liquid phase and the optical measurements. Therefore, it is essential to comprehend the impact of refractive index gradient on the rainbow measurements.

Figure 1.9 schematically displays the influence of the inhomogeneous refractive index on the light trajectories inside the droplet. Solid, dashed, and dot lines represent the light paths by a homogeneous refractive index and inhomogeneous refractive index, respectively. It is observed that the light trajectory corresponding to the homogeneous refractive index is straight. When a gradient occurs in the liquid phase, a straight line turns into a curve. If the refractive index at the droplet center has a much higher refractive index in the liquid phase, the light path bends toward the center of the droplet, which leads to the increase of the rainbow angle. On the contrary, when the refractive index at the surface is greater than the other values in the liquid phase, the light path goes towards the droplet surface, which leads to a smaller rainbow angle. In a nutshell, one can conclude that position with a bigger refractive index value determines the shift of the light path.

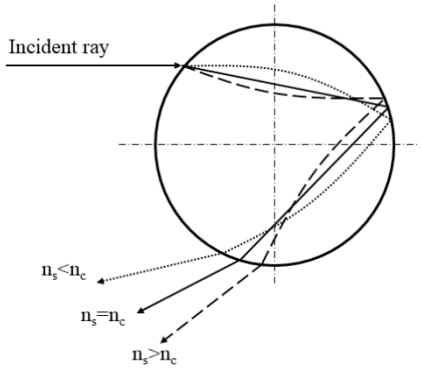

Figure 1.9 The comparison of the light path inside a spherical droplet.

Considering the modifications generated by the gradients inside droplets, the theories for simulating the scattering light from a homogeneous droplet have been extended to an inhomogeneous droplet. An algorithm was developed by Kai and Massoli [64] to simulate the scattering light patterns of an inhomogeneous droplet. The refractive index was regarded as stratified distribution along with the radius directions with a continuous profile. A good result of the scattering patterns was obtained by using the established model. Later, the Generalized Lorenz-Mie theory (GLMT) was proposed by Onofri et al. [65] to take into account the refractive index gradient in the liquid phase, which is an extension of the Lorenz-Mie theory. The droplet was taken as a multilayered sphere. The scattering light patterns of a spherical droplet and the influence of the shape of the laser beam were described by the established model. The results demonstrated the possibility of the improved theory in practical applications with good accuracy. Then, Wu et al. [66, 67] introduced an improved algorithm of the scattering patterns of a multilayered sphere illuminated by a plane wave. The modification of rainbow signals due to the effect of refractive index discontinuity inside droplets was demonstrated. Similarly, the gradient of the refractive index in the liquid phase was considered by Vetrano et al. [68-70] with the Generalized Airy Theory (GAT). They assumed a parabolic profile of refractive index along the radius direction in the liquid phase. The influence of non-uniform in the liquid phase was reflected on the light path and the rainbow angle. It was demonstrated that this theory is as accurate as the other complex theories in presenting the impact of inhomogeneous refractive index. Moreover, Saengkaew et al. [71] simulated the scattering light patterns of the droplet

with a refractive index gradient in the liquid phase. They found that the rainbow created by a non-homogeneous particle is always fitted with a rainbow created by a homogenous one. Accordingly, the concept of equivalent refractive index and size was introduced. Zhou et al. [72] explored the rainbow patterns of a multilayered sphere droplet during the heating process. The analysis was implemented with the framework of Generalized Lorenz-Mie theory (GLMT). The dependence of the scattering light patterns on the beam waist radius, the relative position between the droplet and the Gaussian beam, and the layer number were analyzed. It indicated that the scattering patterns are insensitive to the radius of the beam as long as the radius of the beam is larger than the droplet radius. Besides, a larger layer number is beneficial to eliminating the influence of the discontinuous profile of the refractive index and achieving an accurate result. Those aforementioned theoretical efforts provide a fundamental way to describe the relationship between the non-uniform refractive index and the scattering light patterns. This is critical for the interpretation of the recorded signals from the experiment.

Several experimental studies are available to investigate the temperature gradients inside droplets. Laurent et al. [73] combined two optical methods to measure the mean temperature and the equivalent temperature inside cooling or burning droplets. A line of monodisperse alcohol and acetone droplets with a size of around 100 μm were produced at different injection temperatures. They obtained a mean temperature by laser-induced fluorescence (LIF) and an equivalent temperature by rainbow technique. A parabolic temperature profile inside the droplet was utilized to characterize the temperature at the droplet surface and center. The derived temperature was checked by the numerical prediction with good agreement. Later, the temperature gradients in evaporating alcohol/water droplets were measured by Hopkins et al. [74]. The combination of LIF and cavity-enhanced Raman scattering (CERS) techniques was adopted. LIF provided a volume-averaged temperature and CERS determined a near-surface temperature. One limitation of this work is the experiment by each technique was performed separately rather than simultaneously. By comparing the measured temperature with the numerical predictions, they found that the temperature by CERS agrees well with the model evaluation while a disparity is observed between the value

obtained by LIF and the model. This confirmed the existence of a temperature gradient inside evaporating droplet. Recently, Rosebrock et al. [75] performed experiments to examine the temperature gradients in burning droplets. The rainbow technique was coupled with Interferometric Particle Imaging (IPI) to measure the rainbow signals and droplet size, respectively. Then, the results were compared with a combustion model in order to predict the temperature profiles inside the droplet.

Previous experimental studies confirmed the temperature gradients inside the evaporating or burning droplet. Different techniques, i.e., LIF, CERS, and rainbow technique were exploited to qualitatively and quantitatively measure the gradients in the liquid phase. It is noticed that those former researches combined different experimental methods to get the temperature inside the droplet. The possible combination of the rainbow technique and numerical model to evaluate the temperature is still unknown yet. On the other hand, the two-way couple between the experimental and numerical methods can not only simplify the experimental setup but also provide model validation. Therefore, in this study, the rainbow technique is coupled with the theoretical model to simultaneously quantify the size and temperature during the droplet evaporation process.

1.4 Numerical study of droplet evaporation

1.4.1 Models of droplet evaporation

Droplet evaporation models can be classified into the classical one-dimensional model and the simulations from the Computational Fluid Dynamics (CFD). The evolution and feature of each group are reviewed in this subsection.

The d^2-Law Model: This simplified model originated from Spalding [76], Godsave [77], Goldsmith and Penner [78] assuming a uniform and constant droplet temperature in the liquid phase throughout its lifetime. This model is known as the D^2-Law because of a linear reduction of the normalized squared droplet diameter with time. Due to its simplicity as well as the reasonability, the d^2-Law has been widely used as it is able to provide rough estimation for droplet evaporation rate and spray analyses. Since then, the theories of the fundamental droplet evaporation process have been extensively

exploited during the past decades.

The Infinite Conductivity and Diffusivity Model (ICM and IDM): The main feature of this kind of classical model is the infinite heat and mass transfer rate in the liquid phase so that no temperature or mass fraction gradient occurs. Faeth [79] firstly proposed this droplet evaporation model in 1977 and emphasized its importance to spray evaporation and combustion. The model adopted up to 10 assumptions: 1) The droplet is spherically symmetric with no shape change. The influence of forced convection is considered by multiplying a coefficient; 2) Physical properties of liquid fuel is constant and single component; 3) The gas phase is continuous all the time; 4) Fuel vapor at the droplet surface is saturated; 5) The solubility of gas phase into liquid phase has been neglected; 6) Ignoring the velocity in the liquid phase; 7) The temperature is homogeneous inside the droplet. Accordingly, the temperature maintains spatially uniform but temporally varying; 8) The Lewis number is unit in the vapor film; 9) Radiation is ignored; 10) Chemical reactions are not considered. These hypotheses oversimplified the evaporation, which might induce considerable deviations from reality.

The Conductivity and Diffusivity Limit Model (CLM and DLM): This model assumed a limited heat and mass transfer rate inside the droplet, which leads to an inhomogeneous temperature. It is a typical scenery during the initial 10-20% of the droplet lifetime that has a decisive impact on the combustion characteristics since the reactions occur at a rapid rate in this stage [80]. The results revealed the overall quasi-steadiness of droplet size variation after the initial heating period (20% of the droplet lifetime). By contrast, the unsteadiness of temperature prevails throughout the droplet lifetime. Later, Law C.K. [81] applied this model to simulate the evaporation and combustion characteristics of multicomponent droplets by assuming an ideal solution behavior of the compound. The results indicated a three stages evaporation behavior including an initial transient regime, a quasi-steady stage, and a final volatility limited stage.

The Effective Conductivity and Diffusivity Model (ECM and EDM): Another pioneering work of modeling the droplet evaporation process was done by Abramzon and Sirignano [82]. They developed a simple but sufficient algorithm that can be

adopted in the spray scale. This model considers the influence of droplet motion and the internal circulation on the heat and mass transfer process with the effective conductivity and diffusivity coefficients. The temperature-dependent physical properties, variable Lewis number in the gas-file, the influence of Stefan flow, and transient liquid heating had been incorporated into the model. Sazhin et al. [83] investigated the heating and evaporation of bi-component droplets with this simplified model. The variations of the average temperature evaluated by the model are similar to the experimental data. Despite this model having been universally applied to the simulation of droplet evaporation, its applicability is still open to question as it was only verified for a very limited range of Peclet numbers.

The aforementioned models are one-dimensional and unable to describe the vortex structures as well as the distributions of temperature and species concentrations inside droplets. Regarding this, Computational Fluid Dynamics (CFD) analysis is an alternative method to simulate the droplet evaporation process. A challenge for this kind of model is the capture of the liquid-gas interface. Several methods ranging from fitted grid method, front tracking method, Level-Set method (LS), and Volume of Fluid method (VOF) are available to capture the interface between the liquid and gas phases, which has been substantially used in the investigations of the multiphase flow [84, 85]. Strotos et al [86] predicted the evaporation process of suspended droplets with the VOF method under an ambient temperature up to 1000 K. The adaptive local grid refinement technique was coupled with the VOF method to achieve a high-resolution computation with a controllable computational cost. The model was validated with the experimental data under a wide range of ambient temperature conditions. In general, the Navier-Stokes equations, the energy conservation equations, and species transport equations are directly solved without any simplifications, it can accurately predict the detailed transport information of temperature, mass depletion, vapor concentration, and velocity streamlines during droplet evaporation [86]. Although the detailed information can be accurately predicted, the common feature of the CFD work is the high demand for time and computational resources.

The pros and cons of the 1D model and CFD are significantly distinct. Compared with the CFD works, the one-dimensional model of single droplet evaporation is more

feasible to the spray level as they are less demanded on the computational resources. Whereas the CFD gives insight into the complex 3D dynamics and thermal transport process with the expense of numerical resources. In this case, we have to balance between the benefits and the cost according to the target. In practical applications, a large number of droplets should be considered. The direct solution of those conservation equations in every droplet is not affordable in spray modeling. Therefore, a simplified model to predict the heat and mass transfer is required [63].

1.4.2 Investigations of the influencing factors

Droplet evaporation under different conditions has drawn great attention as its unique applications. To verify the feasibility of different theoretical models in a high-temperature environment, Pinheiro et al. [87] developed the corresponding code of three models: classical evaporation model, Abramzon-Sirignaono model, and non-equilibrium model. They compared the numerical predictions against the experimental data. The performance of different models was also analyzed. It showed that the Abramzon-Sirignano model has the highest agreement with the experimental data in terms of evaporation rate for any ambient conditions. Besides, the influence of the real gas effect of the gas phase surrounding the droplet on the evaporation characteristics is pronounced under high-pressure conditions as a result of the intensified molecules interactions of the gas phase. Several real gas equations of state (EOS) including the Peng-Robison (PR) EOS, the Soave-Redlich-Kwong (SRK) EOS, and the Redlich-Kwong (RK) EOS are available to account for the real gas effect. The accuracy of those equations has been checked in [88] by implementing different equations of state into the numerical model. The transient evaporation of n-heptane droplets in a nitrogen environment had been simulated and validated against the experimental results. It concluded that the PR-EOS predicts the most satisfactory results. Following this, Balaji et al. [89] adopted the PR-EOS to perform the numerical simulations of n-dodecane droplets under high-pressure conditions. The results revealed the different reactions on the variation of ambient pressure according to the ambient temperature. A higher pressure brought about a longer droplet lifetime at sub-critical ambient temperatures, yet shortened the lifetime at super-critical ambient temperature conditions. Besides,

Pinheiro et al. [90] revealed the evaporation behavior of ethanol droplets under different ambient temperature, pressure, and fuel vapor concentration conditions by numerical simulations. The influencing factors of the environment on the evaporation characteristics were systematically analyzed. The most unexpected result was the condensation behavior when the mass fraction of fuel vapor in the ambient is larger than zero. Increasing ambient vapor concentration could have a positive or negative effect on the evaporation rate, which is determined by the threshold temperature.

1.4.3 Investigations of multi-component droplets

Modeling of multicomponent droplets remains a challenging task. The individual component in the mixture has a different evaporation behavior. The differences in the evaporation sequence and the evaporation rate lead to the inhomogeneous temporal and spatial distribution of concentration in the liquid phase. The mass transfer of each component is regarded as diffusion controlled. Following this, the Discrete Component Model (DCM) is one of the prevalent methods when the number of components in the liquid is countable [91]. Due to its CPU-intensive feature, this approach is especially beneficial for the investigations of binary droplets when considering the implementation in the CFD [92, 93]. Apart from that, the Continuous Thermodynamic Approach and the Distillation Curve Model originated from the probabilistic analysis is appliable for the mixture composed of a great number of components [93], for instance, the realistic cases of gasoline and diesel fuels. The main limitation of this kind of model is the assumption of rapid mixing of species inside the droplet. Another alternative approach handles the multi-component by focusing on the diffusion of liquid species named as the quasi-discrete model. The major drawback of this method is the hypothesis of alkanes fuels. Therefore, it can only be applied to the mixture composed of alkanes. The implementation of this model into the mixture composed of other components families is inappropriate [91]. By comparing the models suggested so far, we find that the DCM is the most functional one as it can not only provide species distributions but also have no restrictions on the fuel type.

Ra and Reitz [94] investigated the evaporation behavior of multi-component fuel spray with the Discrete Component Model. The diesel and gasoline were approximated

with six and seven species, respectively. They incorporated this vaporization model into a multi-dimensional CFD code and compared the difference of the results simulated by the single and multi-component fuel. The results indicated that the mass reduction and heating process of droplet by adopting a multi-component and single component model have a significant difference. The multi-component liquid presented the preferential evaporation of different components in the mixture, which significantly impacts the local vapor fuel composition, as shown in **Figure 1.10**. The light components dominate the upstream of the spray while the heavier components are found at the spray tip. This local difference is expected to have an impact on the formation of vapor mixture and combustion process as well as the spray/wall impingement. Similarly, Sazhin et al. [95] simulated the evaporation process of biodiesel with a single-component surrogate fuel and the Discrete Component Model, respectively. They concluded that for biodiesel the predictions based on the multi-component and single component model are close to each other (the difference of lifetimes predicted by two models is less than 5.5 % for typical Diesel engine-like conditions). This is because the major components in biodiesel have similar physical properties such as the molar mass and boiling point. Accordingly, the physical difference is not evident compared to the case of diesel and gasoline.

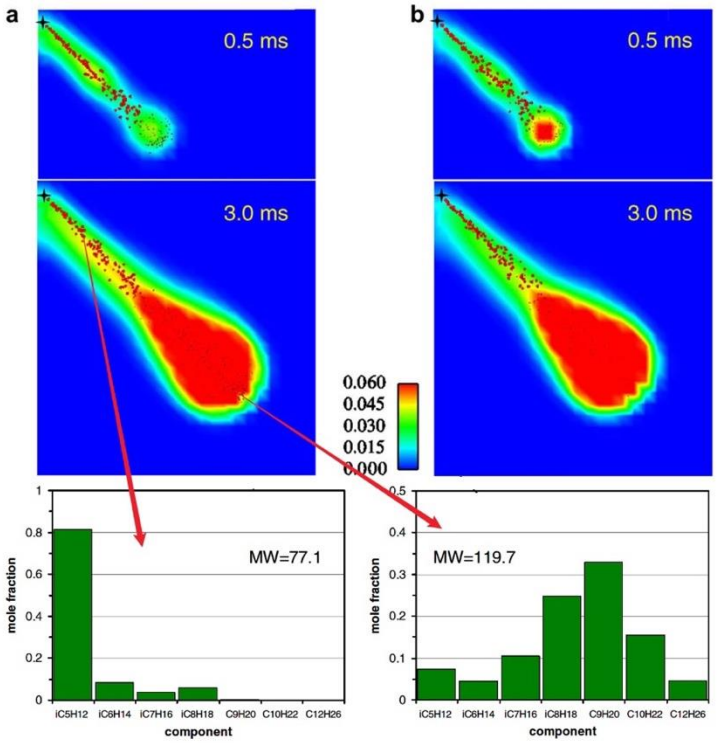

Figure 1.10 Distribution of droplets and fuel mass fractions accompanied by the component distributions at two positions inside the spray [94].

When the multi-component mixtures are composed of components having a large polarity difference, it is inappropriate to treat it as an ideal liquid as the non-ideal phase equilibrium has a significant impact on the evaporation process [96]. For instance, the combination of alcohol fuels and hydrocarbon fuels is a non-ideal mixture because of the polarity of an alcohol molecule.

Several pieces of numerical work provide insight into the influence of the non-ideal equilibrium on the droplet evaporation process. In general, the impact of the non-ideal behavior of the blend on the droplet evaporation process is composed of three aspects, i.e., the non-ideal behavior in the liquid phase, the non-ideal behavior in the vapor phase, and the non-ideal vapor-liquid equilibrium (VLE). The liquid fuel is often the blend of ethanol with acetone, water, or other hydrocarbon fuels. The non-ideal behavior in the liquid phase is considered through the activity coefficient. Maqua et al. [62] evaluated the activity coefficient of ethanol and acetone binary droplets with the empirical correlations. While the Universal quasi-chemical Functional Group Activity Coefficients (UNIFAC) had been applied for the computation of activity coefficients in the investigations of Brenn et al. [97] and Narasu et al. [98]. In addition, Bader et al. [99] incorporated another coefficient of the Poynting factor to modify the non-ideal behavior in the liquid phase. Apart from that, they adopted the fugacity coefficient to consider the non-ideal behavior in the vapor phase. Those modifications were implemented into an infinite conductivity evaporation model. The aforementioned literature demonstrated the influence of non-ideal behavior on the droplet size, temperature evolution, or the evaporation sequence of individual components in the blend. Especially, the results in [99] validated the importance of taking into account the impact of non-ideal behavior in the vapor phase. Nevertheless, the investigations by Bader et al. [99] were based on the homogeneous temperature and concentration in the liquid phase, which induces remarkable deviations under high-temperature situations [100].

In our previous study [101], the evaporation characteristics of acetone-butanol-ethanol and diesel blends droplet under high-temperature, high-pressure, and

convective conditions had been numerically investigated. The temperature-dependent physical properties of liquid fuel were considered. The non-ideal behavior of the ABE and hydrocarbons mixture were considered through the UNIFAC method. The real gas effect under high-pressure conditions was presented by the PR-EOS. The accuracy of the established model was validated against the experimental results. In addition, a comparative analysis was made by exploring the droplet evaporation process under different ambient temperature, pressure, and velocity conditions. The results revealed the reactions of different kinds of fuels on the variation of ambient conditions. A higher ambient temperature was especially beneficial for the mass reduction rate of less volatile components. The impact of ambient pressure on the evaporation rate was coupled with the ambient temperature. A higher pressure suppressed the evaporation rate under low-ambient temperature conditions yet enhanced the evaporation rate under high-ambient temperature conditions. In addition, each component showed a different sensitivity on the variation of pressure, which depends on the diffusion coefficient. In a nutshell, the model shows the potential in revealing the mechanism of the evaporation process.

1.4.4 The influence of non-sphericity on droplet evaporation

Most of the models describing the droplet evaporation are based on the assumption of a spherical droplet. Nevertheless, the shape of most droplets encountered in practical engineering applications is far from spherical [102]. The dynamic stress is prone to deform the droplet, while the surface tension forces the droplet to maintain a spherical shape, which is an equilibrium state [103]. A significant shape deformation can be induced from the relative motion between droplet and gas medium when the Weber number is larger than one [104].

Establishing the evaporation theory for arbitrary shape droplets is infeasible. In most cases, the variation of droplet shape is considered by assuming a prolate or oblate spheroids droplet [91]. The influence of shape change on the evaporation rate was discussed in [105] by assuming the same volume. It demonstrated that oblate spheroid droplet shape enhances the evaporation rate compared with the spherical droplet. This can be explained from the aspect of surface area. The surface area of a spherical droplet

is smaller than that of a spheroid droplet with the same volume. Li and Zhang [106] carried out a theoretical study of an oblate spheroidal droplet under forced convection conditions. They introduced the Sherwood number and Nusselt number for an oblate spheroid droplet. It stated that the oblate spheroidal droplet has a slower mass regression rate than a spherical droplet when the surface area is the same. The increase of aspect ratio decreases the Sherwood number and Nusselt number. Tonini and Cossali [107] theoretically investigated the evaporation process of an oscillating spheroidal drop by taking into account the influence of oscillations from oblate to prolate states on the evaporation rate. The evaporation mechanism from oblate to prolate droplets was revealed by this model. The results indicated that the average evaporation rate increases monotonically with the increment of maximum surface area. Later, they developed a general 1-D mathematical approach to analyze the steady-state evaporation of spheroidal droplets [108]. This model was capable of evaluating the information of evaporation rate, heat fluxes, and local vapor concentration. The evaporation rates of three kinds of droplets including the spherical, spheroidal, and triaxial ellipsoidal ones were analyzed. The results validated the impact of droplet shape on droplet evaporation. It revealed that the prolate droplet has the fastest evaporation rate whereas the oblate droplet has the lowest evaporation rate.

Additionally, mathematical modeling of spheroidal droplet evaporation was conducted by Zubkov et al. [109]. They considered the temperature distribution inside the droplet and the shape change of the droplet with a two-dimensional configuration. The results revealed that the droplet evaporation time is insensible to the droplet non-sphericity when the droplet eccentricity is in the range of 2/3 to 1.5. By contrast, the non-sphericity noticeably modifies the temperature evolutions. In both cases, the spheroidal droplets evolve to more spherical ones with time as a result of surface tension and evaporation. It can be inferred that the influence of non-sphericity was largely presented in the early heating period. This model can be regarded as one of the most advanced ones except for the models based on the analytical solutions [91]. Zaitone [7, 110] explored the evaporation behavior of an oblate droplet by combining the experimental and numerical methods. The acoustic technique was adopted to suspend the droplet and maintain the aspect ratio at approximately 0.7. The results

revealed an inverse proportion between the aspect ratio and evaporation rate.

Due to the aerodynamic force, the non-sphericity of droplets happens in a very short time in experimental conditions and spray, which makes it difficult to observe this phenomenon. However, the rainbow technique is capable to capture this variation as the change of droplet shape modifies the rainbow angle or scattering patterns as investigated in [111]. The oscillation of the rainbow patterns as a result of non-sphericity was observed by Li et al. [112] during a spark heating process. Similarly, Wu et al. [60] discovered the dramatic change of rainbow patterns during the spark heating process due to the strong disturbance of the flow field on the droplet shape. In some cases, the rainbow signal was completely distorted by the strong oscillation, which reveals the intense change of droplet morphology. Later, Wu et al. [113] explored the application of rainbow refractometry in measuring the surface tension and viscosity of droplets by taking advantage of the linkage between the droplet deformation amplitude and the angular shift of the rainbow signal. It is claimed that the angle position is extremely sensitive to the aspect ratio of a droplet. Changing the droplet shape from spherical to spheroidal with a non-sphericity of 1.01 shifts the angular position of the primary rainbow to 1°. They quantified the influence of droplet deformation on the rainbow patterns in the range of non-sphericity of 0.95-1.05. The results indicated that the scattering angle of the rainbow pattern keeps increasing when the droplet shape varies from oblate to round finally to prolate. The consideration of shape changes substantially improved the spatial resolution of the rainbow measurement.

1.5 Objective

Aiming at the accurate description of droplet evaporation behavior and the development of evaporation theory and measurement technique, the combination of the experimental method and simulation approach has been utilized for analyzing the evaporation behavior of mono and binary droplets under different conditions. From the perspective of simulation, the above literature demonstrated the necessity of adopting a simple yet reliable model regarding the incorporation into a spray scale with a great number of droplets. Therefore, an improved model based on the effective conductivity and diffusivity model has been proposed, which incorporates the impacts of convection,

the temperature-dependent physical parameters, the non-ideal vapor-liquid equilibrium of the mixture, and the effect of distance between neighbor droplets. On the other hand, a parallel experimental effort to get the evaporation behavior of moving droplets demands ingenuity. To be realistic, the droplets under testing should be small (of the order of 100 μm) and free from any suspension device. Accordingly, the combination of high accuracy rainbow technique with free-falling droplets has been utilized to simultaneously measure the droplet size, temperature, and concentration during the evaporation process. An algorithm considering the refractive index gradient in the liquid phase and shape change has been developed to retrieve the evaporation parameters from the scattering image, which substantially improves the accuracy of data processing. Then, the evaporation processes of mono and ethanol/heptane binary droplets with different conditions have been investigated with both experimental and simulation methods. The thesis mainly has six chapters:

Chapter 1 introduces the applications and background of droplet evaporation. The experimental researches and numerical studies widely adopted in the investigation of droplet evaporations have been described. The necessity to adopt the experimental configurations of the rainbow technique with the free-falling droplets is described. A review of the droplet evaporation simulation lays the fundamentals of the thesis.

Chapter 2 systematically describes the experimental methodology including the whole setup and each segment, the verification of the rainbow theory for post-processing. The physical parameter of the tested fuel and their dependence on temperature in the present work has been introduced as well. An inversion algorithm is proposed for the post-processing of experimental data. On the basis of this, the reliability and repeatability of the measurement method have been checked.

Chapter 3 narrates the details of the numerical method including the physical description, model assumptions, the solution of heat and mass transfer process, and the numerical algorithm. The impact of convection, the temperature-dependent physical parameters, the non-ideal equilibrium of the mixture, and the effect of distance between neighbor droplets are considered. Besides, the model is validated by experimental and simulation results in the literature.

Chapter 4 focuses on the transient evaporation behavior of ethanol and heptane

droplets by rainbow measurements. The retrieved droplet diameter and refractive index from the rainbow patterns have been compared with the model predictions. As a consequence, the temporal evolutions and spatial distributions of temperature are obtained. The difference between the model predictions and experimental results has been further investigated.

Chapter 5 gives an account of the evaporation behavior of ethanol and heptane binary droplet obtained by both experimental and simulation methods. The influence of non-ideal vapor-liquid equilibrium on the preferential behavior of binary droplet is observed and confirmed by the rainbow experimental results. The coupling influence of ambient temperature, pressure, and compositions in the liquid phase on the preferential evaporation of droplets is obtained.

Chapter 6 summarizes the main outcome of the present work and highlights the innovations. It also talks about the required effort in future work.

2. Experimental methodology

2.1 Rainbow technique

The rainbow system developed in this work together with the schematic diagram are shown in **Figure 2.1**. It mainly has three sections including a fuel supply and droplet generation system, a temperature and pressure control system, and a data acquisition system. When conducting the experiment, the temperature of the chamber is regulated to the expected point by a PID controller with an accuracy of ± 0.1 K. The temperature range in the present work is 373-473 K. Then, a free-falling droplet stream produced by a piezoelectric droplet generator (MTG-01-G1, FMP) vaporizes under a high-temperature environment. The initial temperature of the droplet stream is the same as the room temperature of 293 K by using a water cooling system surrounding the generator. Three pinholes with a diameter of 50 μm, 75 μm, and 100 μm are available to adjust the initial diameter of the droplet stream. Finally, a pulsed laser beam with a wavelength of 532 nm illuminates the droplet stream. An optical lens with a diameter of 75 mm and a focal length of 150 mm collects the scattering lights from droplets. A high-speed CCD camera with a resolution of 2048×2048 pixels records the scattering images of droplets at the vicinity of the rainbow angle. Noting that the frequency of laser illumination and the frame rate of the camera are synchronized with each other at 17 fps by the Insight 4G software in the computer. The explosion time of the camera is 500 μs. The measurement of droplets at different positions can be achieved by adjusting the vertical position of the illumination part and the image receiving part. A range of 37-44 mm and 47-54 mm from the vertical direction of the nozzle can be detected. An adjustment of 1 mm per time is adopted in this work to ensure a sufficient sample point. At least 100 images are recorded at each sample point for all the tests.

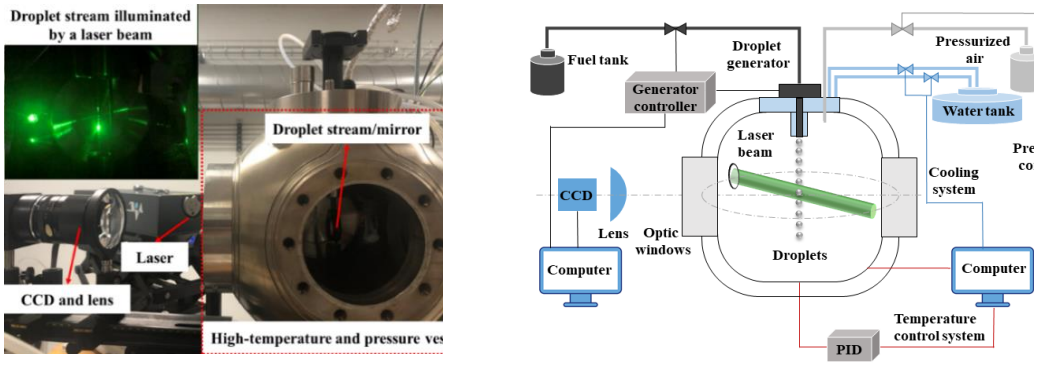

(a) Compositions of the setup **(b) Schematic plot**

Figure 2.1 Experimental setup.

2.1.1 Droplet generation

A piezoelectric droplet generator (MTG-01-G1, FMP) with different pinhole sizes produces the free-falling droplet stream. The mechanism of generating droplets from laminar fluid jets is based on the Rayleigh breakup theory. As stated, deformation appears at the jet surface when the interference is imposed on a continuous jet. The wavelength of the deformed jet can be calculated from the velocity and the interference frequency. The criteria for a jet decaying into droplets depends on the following equation:

$$\lambda = \frac{u_D}{f_G} \geq \pi D, \tag{2.1}$$

with λ is the wavelength of the deformed jet, u_D and f_G are the velocity of the jet and the excitation frequency, respectively. D is the diameter of the pinhole in μm. Noting that the jet velocity u_D is calculated by the Bernoulli's equation stated as:

$$u_D = \sqrt{\frac{2 \times (P_{inj} - P_{amb})}{\rho}}, \tag{2.2}$$

In order to generate a stable line of mono-dispersed droplets with the same size and spherical shape, the dimensionless wavelength of the excitation wave expressed as $k = \pi D / \lambda$ is in the range of 0.3-0.9. In this context, generator frequency f_G and the injection pressure P_{inj} are the main parameters in controlling the stability of the generator. Those parameters were controlled by adjusting the pulse generator together with the pressure of the pump. According to the theoretical formula, the frequency range used to generate monodisperse droplets is determined as below:

$$\frac{0.3u_D}{\pi D} \leq f_G \leq \frac{0.9u_D}{\pi D}, \tag{2.3}$$

The droplet size d can be coarsely predicted from the volume flow rate Q and exciting frequency f_G. The formula is provided as:

$$d = \left(\frac{6Q}{\pi f_G} \right)^{1/3}, \tag{2.4}$$

noting that the volume flow rate Q can be defined as:

$$Q = u_D \bullet A, \tag{2.5}$$

with A is the cross-section area stated as:

$$A = \frac{\pi D^2}{4}. \tag{2.6}$$

In this case, the diameter of the droplet stream can be evaluated from the pinhole diameter:

$$d = \left(\frac{3u_D D^2}{2 f_G} \right)^{1/3} = D \left(\frac{3\pi}{2k} \right)^{1/3}. \tag{2.7}$$

According to those theoretical calculations, the velocity, excitation frequency, and the diameter range for monodisperse droplets under different injection pressure are displayed in **Table 2.1**. The pinhole diameter is 100 μm. It indicated that the velocity and the range of excitation frequency are proportional to the injection pressure. A higher injection pressure means a faster movement of droplets, which needs a larger excitation frequency to produce a monodisperse droplet stream. For a fixed injection pressure, the adjustment of excitation frequency is critical to the stability of the droplet stream. A stable droplet stream generates a clear rainbow pattern with both primary peaks and ripple structures which is the criteria to ensure a stable working condition of the generator. In practical experiments, the excitation frequency is adjusted until a clear and stable rainbow pattern is observed. In addition, the range of exciting frequency to produce monodisperse droplets and the diameter of droplet stream with different pinhole sizes are compared in **Table 2.2**. Those data define a sparse range of working conditions for the generation of droplet streams.

Table 2.1 The variation of velocity, excited frequency, and droplet diameter under different injection pressure at the normal pressure and room temperature conditions.

D (μm)	A (μm^2)	P_{inj} (bar)	u_D (m/s)	Range of f_G (kHz)	Diameter of droplet (μm)
100	7850	1.2	6.11	5.84-17.51	131.29-330.52
100	7850	1.4	8.80	8.40-25.20	131.29-330.52
100	7850	1.6	10.83	10.34-31.03	131.29-330.52
100	7850	1.8	12.54	11.98-35.94	131.29-330.52
100	7850	2.0	14.05	13.42-40.24	131.29-330.52

Table 2.2 Range of excited frequency to produce monodisperse droplets and the diameter of droplet stream with different pinhole sizes.

D (μm)	A (μm^2)	P_{inj} (bar)	u_D (m/s)	Range of f_G (kHz)	Diameter of droplet (μm)
50	1960	1.2-2.0	6.11-14.05	11.67-40.51	82.70-165.26
75	4420	1.2-2.0	6.11-14.05	7.78-40.51	108.38-247.89
100	7850	1.2-2.0	6.11-14.05	5.83-40.51	131.29-330.52

2.1.2 Optical segment design

The schematic diagram of the collection unit is illustrated in **Figure 2.2**. The compositions of the system and positions of each part are as follows:

Lens 1: First optical lens in the imaging system with a diameter of 75 mm and focal length f_1 =150 mm. It mainly collects the scattering light from droplets.

S_1: The distance from the position of the droplet to the principal plane of the first lens. It can be calculated from this correlation: $M=f_1/(S_1-f_1)$, with M is the magnification ratio. An appropriate value of M=1.17 has been chosen coupled with a lens of f_1 =150 mm. The resulting S_1=278 mm.

Lens 2: The second small lens with a diameter of 50 mm and focal length of 50 mm. Adding this lens into the configuration principally shortens the focal length and the whole length of the imaging system. The position of the second lens is right next to the first lens. The interval between the two lenses is narrow at about 20 mm. The focal length after the combination of the two lenses can be calculated from the below equation.

$$\frac{1}{f} = \frac{1}{f_1} + \frac{1}{f_2} - \frac{L}{f_1 f_2}. \tag{2.8}$$

S_2: The distance between the camera and the first lens. One can change the quality

of the scattering pattern by adjusting the position of the camera. Accordingly, the distance producing the clearest scattering patterns is the desired value of S_2.

Noting that the camera in the rainbow system captures the out-of-focus image (scattering patterns) rather than the focused image of the droplet. Therefore, the position of each part is determined by whether a clear and suited scattering pattern can be visualized in the view of the camera. Once the optimum location of each part has been detected, it will remain unchanged ever since for all tests.

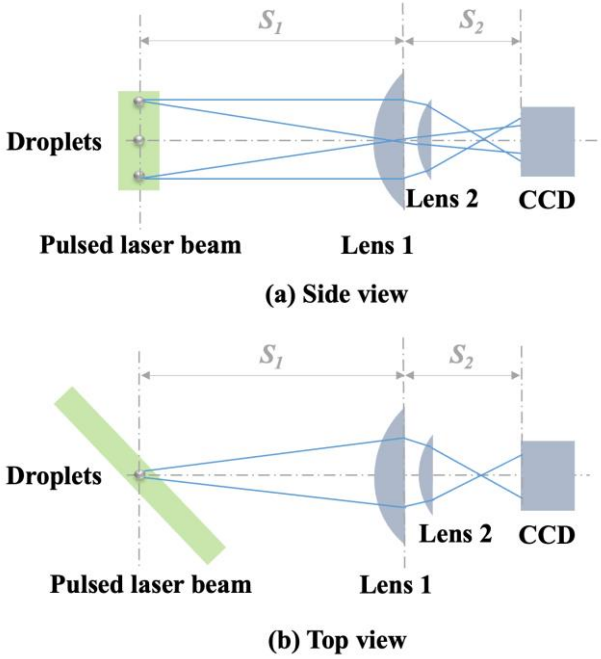

Figure 2.2 Optical setup of the rainbow system.

2.1.3 Rainbow simulation

The simulation of the light patterns nearby the rainbow angle is fundamental for the data inversion process. This work adopted the Airy theory to perform the post-processing procedure concerning the complicity of other simulation methods for data inversion [43]. The simplicity yet reliability of Airy prediction ensures the accuracy of the droplet size and refractive index extracted from the scattering light patterns by iteration.

2.1.3.1 Airy theory

The Airy theory is a scalar diffraction theory that describes the scattering of sine

waves after experiencing internal reflections and leaving the spherical particle, as was first done by George B. Airy [114]. The relationship between the scattered intensity and scattering angle is given by [37],

$$I(\theta,\alpha)=(\varepsilon_1)^2[\frac{81}{16\pi^2h^4}]^{1/6}\cos\tau_p\alpha^{7/3}Ai^2(-z)/\sin(\theta_{rg}), \tag{2.9}$$

where $\alpha=\pi d/\lambda$, θ_{rg} is the rainbow angle, which can be calculated by,

$$\theta_{rg}=\pi+2\cos^{-1}\left(\sqrt{\frac{n^2-1}{p^2-1}}\right)-4\cos^{-1}\left(\sqrt{\frac{p^2(n^2-1)}{(p^2-1)n^2}}\right), \tag{2.10}$$

with n is the refractive index of the droplet, A_i is the Airy integral. Normally, it has the form as defined by Abramowitz and Stegun [115],

$$Ai(-z)=\frac{1}{\pi}\int_0^\infty\cos(\frac{t^3}{3}-zt)dt, \tag{2.11}$$

the argument z is:

$$z=[\frac{12}{h\pi^2}]^{1/3}\alpha^{2/3}(\theta-\theta_R), \tag{2.12}$$

h and ε_i are as follows,

$$h=\left[\frac{(p^2-1)^2}{p^2(n^2-1)}\right]\left[\frac{p^2-n^2}{n^2-1}\right]^{1/2}, \tag{2.13}$$

$$\varepsilon_i=(1-r_i^2)(r_i)^{p-1}, \tag{2.14}$$

with

$$r_1=\frac{\sin(\tau_p-\tau_p')}{\sin(\tau_p+\tau_p')}, \tag{2.15}$$

$$r_2=\frac{\tan(\tau_p-\tau_p')}{\tan(\tau_p+\tau_p')}, \tag{2.16}$$

where τ_p and τ_p' are the complements of incident and refraction angles of the incident rainbow ray of p-1 internal reflections,

$$\tan\tau_p=\left[\frac{n^2-1}{p^2-n^2}\right]^{1/2}, \tag{2.17}$$

$$\tan \tau_p' = \left[\frac{p^2\left(n^2-1\right)}{p^2-n^2} \right]^{1/2}. \tag{2.18}$$

2.1.3.2 Verification of the Airy theory

To examine the ability of the Airy theory in simulating the rainbow patterns, the scattering light intensity curves predicted by the Airy theories are compared with the Lorenz-Mie theory because the Lorenz-Mie theory is the most rigorous method taking into account all the aspects. A software named MiePlot is adopted to simulate the light intensity curve based on the Lorenz-Mie theory. This software is able to predict the light intensity curves by using different kinds of theories including the Lorenz-Mie, Debye, Airy, and Descartes, etc. [116]. The results nearby the rainbow angle are displayed in **Figure 2.3**. The diameter and refractive index of the droplet are 100 μm and 1.3653, respectively. The wavelength of the incident light is 532 nm. Firstly, several peaks are presented in the primary rainbow region including one main rainbow peak and several Airy fringes. The difference between the two methods is the ability to simulate the ripple structure. Airy theory only shows the feature of main peaks compared with the Lorenz-Mie simulations. In addition, the results indicate that the Airy theory is as accurate as of the Lorenz-Mie simulations in predicting the rainbow positions of the first and second peaks. A visible deviation in the rainbow positions of the third and fourth peaks is observed. Considering the first and second peaks regions are critical for the rainbow technique, it can be concluded that the Airy theory is accurate enough for the application of rainbow measurement [117]. The accuracy and effectiveness of the Airy theory in predicting the scattering light intensity curves are systematically analyzed from the aspect of diameter, refractive index, and incident wavelength in detail.

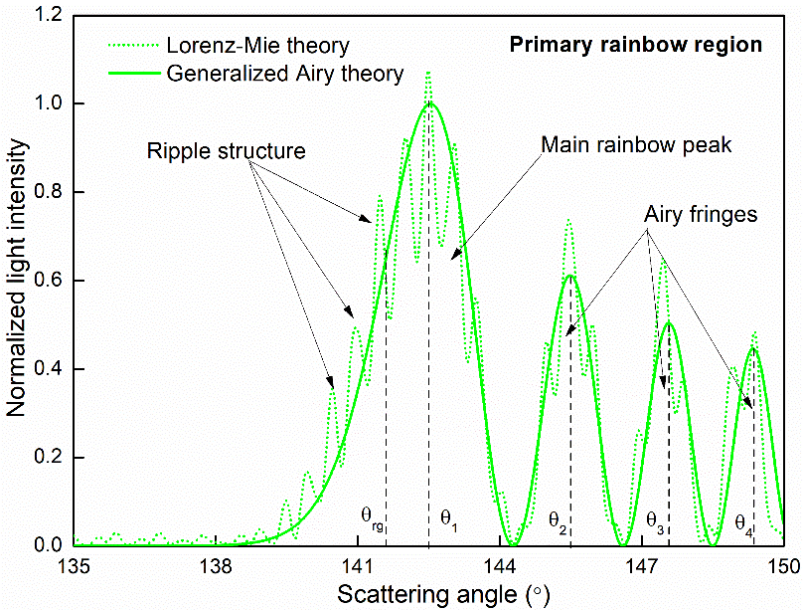

Figure 2.3 The comparison of the normalized light intensity curves predicted by two theories.

The effective diameter range of the Airy theory producing a satisfactory performance is checked with a droplet diameter range of 20-1000 μm. The wavelength of the incident light is 0.632 μm. The refractive index of the droplet is taken as 1.33. For each droplet, the scattering light intensity predicted by the Airy theory is compared with the corresponding Mie results, as displayed in **Figure 2.4**. In the first, the deviation of Airy theory in predicting the angular position of rainbow peaks is remarkable for small droplets with a diameter value of 20 and 40 μm. Under this circumstance, Airy prediction only has good performance over the angular region of the first peak. However, it is observed that the Airy simulation has a good agreement with Mie's prediction over the first two peaks for droplets with 100 μm, the first three peaks for droplets with 400 μm, the first four peaks for droplets with 1000 μm, and so on. That is to say, by increasing the droplet diameter, the accuracy of the Airy simulation has been intensively improved because more peaks are overlapping with the prediction of Mie theory. Overall, the Airy simulation can well predict the angular position of the first two peaks as long as the diameter of the droplet is larger than 100 μm.

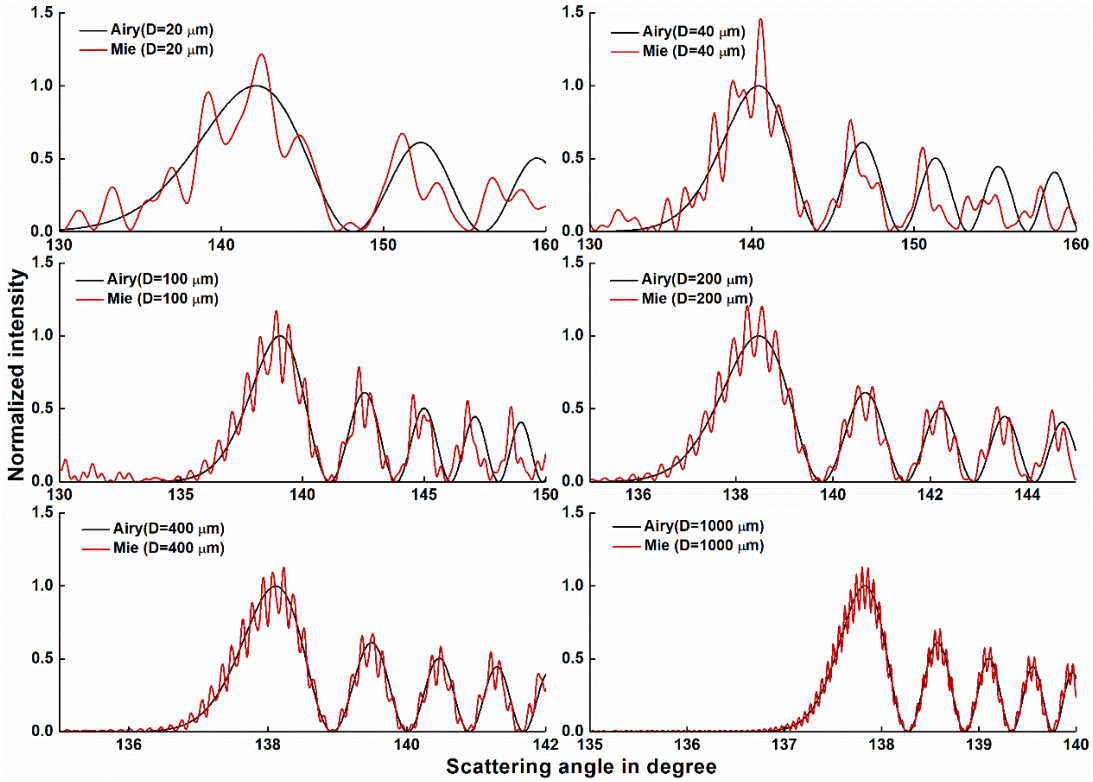

Figure 2.4 Scattering light intensities predicted by Mie and Airy theory with different droplet sizes.

Next, the impact of the refractive index on the Airy simulations is examined. The droplet diameter is taken as 100 μm. The wavelength of the illumination is 0.632 μm. The refractive index varies from 1.33 to 1.5 as it covers the refractive index values of most liquid fuels [118]. **Figure 2.5** demonstrates the negligible influence of the refractive index on the accuracy of Airy prediction. With the present simulation configuration, the angular positions of the first two peaks obtained by the Airy theory agree well with the Mie prediction regardless of the refractive index values. Therefore, the Airy theory can be applied to any refractive index values as long as the diameter range is satisfied.

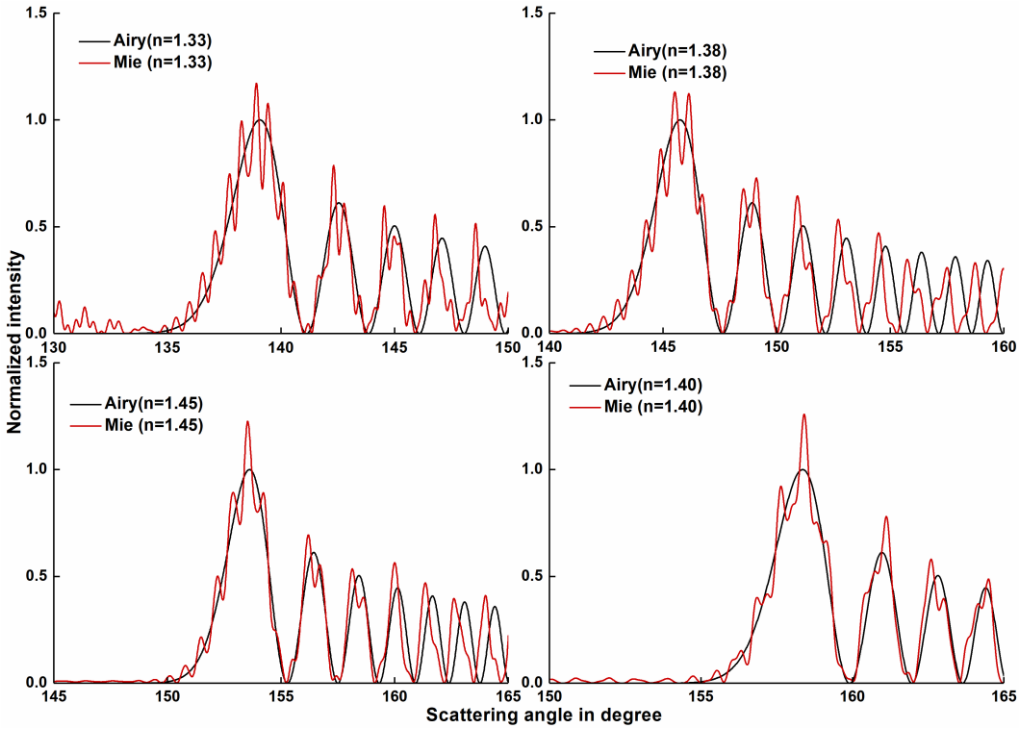

Figure 2.5 Influence of refractive index range on the accuracy of Airy prediction.

Finally, the sensitivity of incident wavelength on the scattering light patterns by the Airy and Mie theory is investigated with three wavelength values of 0.632, 0.582, and 0.532 μm. The particle diameter and refractive index values are 100 μm and 1.33, respectively. As indicated in **Figure 2.6**, the incident wavelength has a slight impact on the angular position of scattering patterns. More importantly, changing the wavelength does not alter the accuracy of the Airy theory in predicting the first two rainbow peaks.

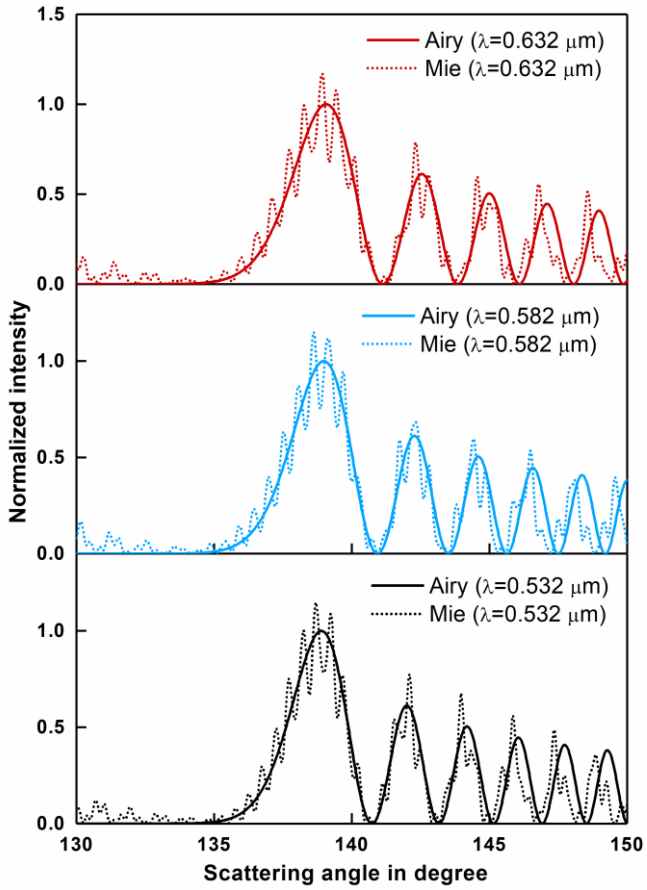

Figure 2.6 Comparison of Airy and Mie simulation under different wavelengths.

2.1.4 Impact of refractive index gradient and non-sphericity droplet

2.1.4.1 The Generalized Airy Theory (GAT) for non-uniform sphere

The rainbow simulation described in the previous section is designed for homogeneous droplets without a temperature gradient inside the droplet. Nevertheless, an inhomogeneous distribution of refractive index inside the droplet is general in practical situations as a result of heating and evaporation. The existence of temperature and composition gradient inside droplets leads to an inhomogeneous spatial distribution. The modification of the refractive index gradient on the light trajectory is displayed in **Figure 2.7**. Solid and dot lines represent the light paths by a homogeneous refractive index and inhomogeneous refractive index, respectively. It is observed that a straight line turns into a curve when a gradient occurs in the liquid phase. If the refractive index at the droplet center has a much higher refractive index in the liquid phase, the light path bends toward the center of the droplet, which leads to the increase of the rainbow

angle.

Regarding this, an inversion algorithm based on the Generalized Airy Theory (GAT) [68-70] has been developed by taking into account the influence of the inhomogeneous distribution of refractive index inside droplets on the rainbow angle. The refractive index in the liquid phase is assumed to be a polynomial distribution along the radial direction, which is an effective way to present the impact of the refractive index gradient on the rainbow position.

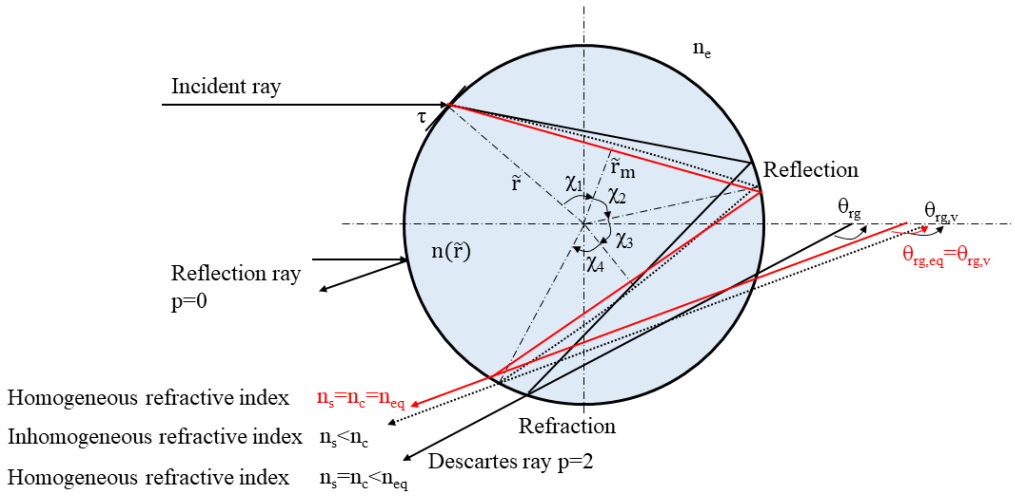

Figure 2.7 The light path corresponds to a homogeneous and inhomogeneous refractive index inside a spherical droplet.

The calculation process of this method is described hereafter. When the incident rays with an incident angle τ enter a transparent droplet, the scattering angle θ when it comes out of the droplet is calculated by [43],

$$\theta=2\tau\text{-}2p\tau', \tag{2.19}$$

with τ' stands for the refraction angle. When the refractive index inside the droplet is inhomogeneous, Eq.(2.19) can be generalized into,

$$\theta_v[\tau,\tilde{r}]=2\tau-2p\chi_1[\tau,\tilde{r}]. \tag{2.20}$$

It means a variable scattering angle by considering the influence of the refractive index gradient along the non-dimensional radius direction. $\tilde{r}$ is the non-dimensional droplet radius. The variation of χ_1 along the radius direction is considered through the integration of the light rays inside each layer,

$$\chi_1 = \int_1^{\tilde{r}_m} \frac{n_e \cos\tau}{r\sqrt{n(\tilde{\mathrm{r}})^2\,\tilde{\mathrm{r}}^2 - \left(n_e\cos\tau\right)^2}}\partial\tilde{\mathrm{r}}\,, \tag{2.21}$$

with n_e is the refractive index in the gas phase, $\tilde{r}_m$ means the minimal distance between the droplet center and light trajectory. The value of $\tilde{r}_m$ is one of the solutions of the cubic equation $n(\tilde{r})\tilde{r} = n_e\cos\tau$. The refractive index along the non-dimensional radius direction is regarded as a multi-layered distribution with a polynomial form,

$$n(\tilde{r}) = n_c - (n_c - n_s)\tilde{r}^m, \tag{2.22}$$

where $n(\tilde{\mathrm{r}})$ is the non-dimensional refractive index with a polynomial order m. n_c and n_s are the refractive indices at droplet center and surface, respectively. Under this context, the scattering light intensity by a droplet with a diameter d is calculated as,

$$I = \left|\int_0^{\infty} \cos\left[\frac{\pi}{2}\left(\left(-\left(\theta-\theta_{rg,v}\right)\left(\frac{16d^2}{h\lambda^2}\right)^{1/3}\right)\eta-\eta^3\right)\right]d\eta\right|^2, \tag{2.23}$$

with

$$h = \frac{2}{3}\frac{\partial^2\theta}{\partial\tau^2}\bigg|_{\tau=\tau_{rg}}\frac{1}{\sin^2\tau_{rg}}\,, \tag{2.24}$$

$$\theta_{rg,v} = \theta\left[\tau_{rg}\right], \tag{2.25}$$

where λ is the wavelength of the incident light. τ_{rg} and θ_{rg} are incident angle and scattering angle corresponding to the rainbow position, which can be solved from eq.(2.20).

2.1.4.2 Multilayered refractive indices and equivalent parameters

As stated before, the refractive index gradient directly changes the rainbow angle. Eq.(2.22) originates from the assumption that the distribution of refractive index is a multilayered sphere depending solely on radial location. Each layer has a different refractive index n_1, n_2,…, and n_i as schematically displayed in **Figure 2.8**. Theoretically, a layer value of 128 is enough to provide a continuous profile of the refractive index in the liquid phase. Regarding the practical case investigated in this work, the heating and evaporation of droplets lead to the decrease of refractive index with time. Technically, the refractive index at the droplet surface is smaller than the value at the droplet center. This behavior is because the heat conduction firstly happens at the droplet surface and

gradually transfers into the center, which creates a higher temperature at the surface of the droplet. Noting that the assumption of $n_c > n_s$ is not valid for all the cases such as the multicomponent droplets. The variation of the refractive index is affected by the temperature and compositions at the same time. Therefore, a larger refractive index at the droplet surface is possible under some situations.

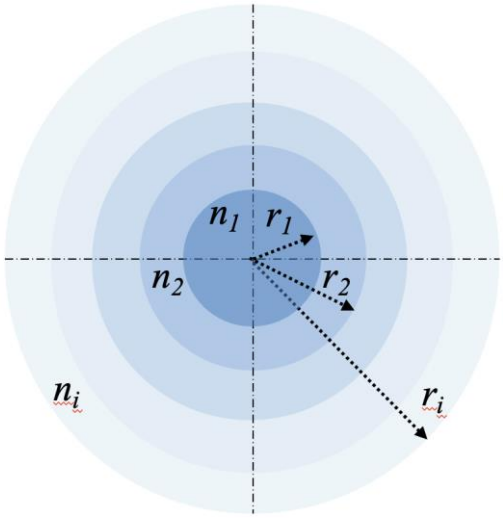

Figure 2.8 Schematic of multilayered sphere model.

The polynomial order controls the gradient profiles, which has been exemplified in **Figure 2.9**. The diameter adopted for simulation is 100 μm. The refractive indices to do the comparative study are taken as 1.365 and 1.357, respectively, which corresponds to a temperature of 10 °C and 30 °C [119]. Red and blue lines stand for the gradient distributions when m is positive and negative, while the black line is the case when m equals 1 or -1. It is found that a negative m leads to a stepper gradient at the center of the droplet. The overall gradient profile is closer to the surface refractive index as demonstrated by the negative extreme of m=-10. In contrast, a positive m value leads to a sharp refractive index gradient nearby the droplet surface. Moreover, a linear regression of the refractive index with non-dimensional radius is observed when m is 1 and -1.

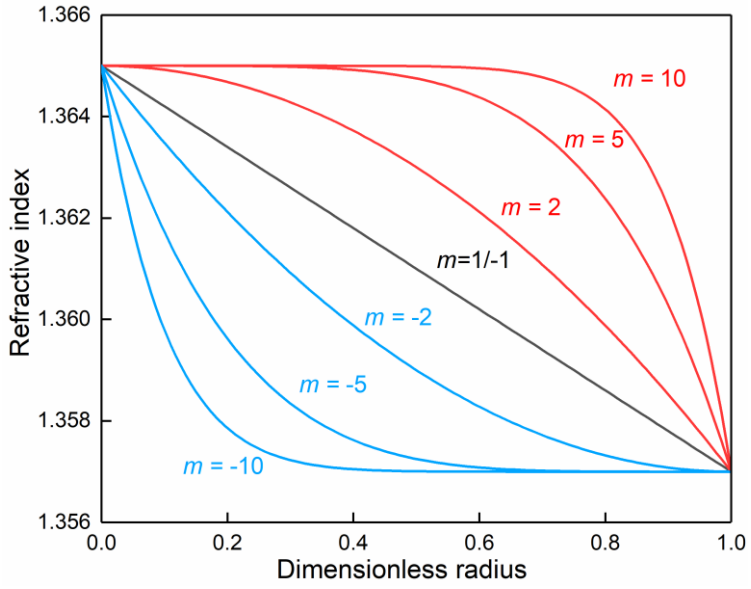

Figure 2.9 Example of gradient profiles affected by polynomial order m with n_c =1.365, n_s =1.357, 128 layers.

The normalized light intensity curves corresponding to the homogeneous and inhomogeneous droplets evaluated by the Airy theory are displayed in **Figure 2.10**. The polynomial order is 2 for the inhomogeneous droplet. As indicated, the deviations between the homogeneous and inhomogeneous predictions are apparent. The inhomogeneous refractive index moves the light intensity curve toward a larger scattering angle region. More importantly, the light intensity curves produced by a inhomogeneous droplet can be always fitted by the light intensity curves of a homogeneous droplet with almost the same size [71], as exemplified by the red dot line. It is noticed that the inhomogeneous refractive index has no influence on the value of diameter while having a huge impact on the refractive index. This provides an efficient way to interpret the recorded light intensity curves from the experiment measurement when considering the impact of the inhomogeneous refractive index. When conducting the data inversion process, the inversion code computed the light intensity curves in the framework of a homogeneous refractive index inside the droplet with the Airy theory. The optimum fitted light intensity curve simulated by a homogeneous refractive index can be obtained through the comparison with experimental measurements. As a consequence, the homogeneous refractive index corresponding to the optimum fitted light intensity curve is defined as the equivalent refractive index. Therefore, the

refractive index extracted from the experimental results during the post-processing is the equivalent refractive index. Under this context, the real temperature and temperature distribution inside the droplet can be further evaluated by analyzing the relationship between the equivalent refractive index and refractive index profile along the radius direction.

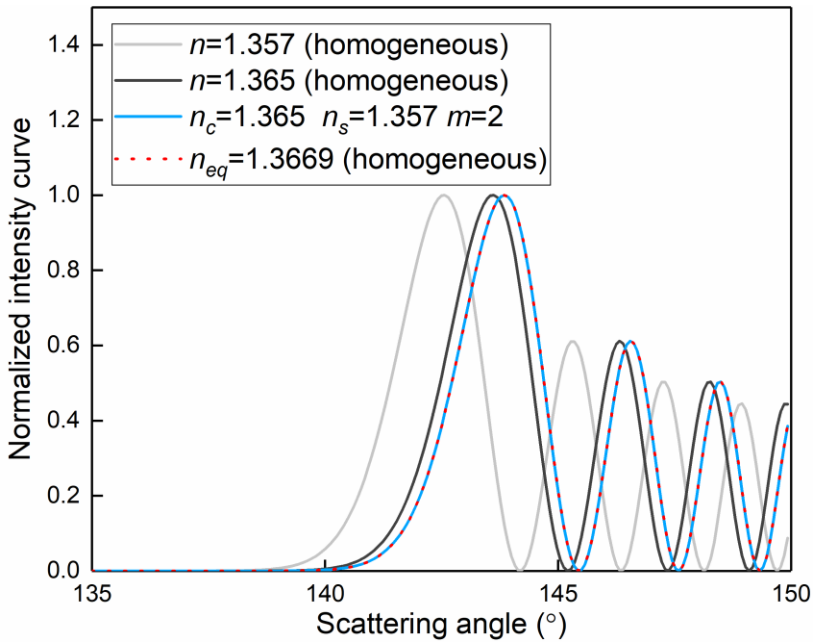

Figure 2.10 The simulated rainbow signals of homogeneous and inhomogeneous droplets.

2.1.4.3 The non-sphericity droplet shape

As demonstrated in [111, 113], a slight change in the aspect ratio leads to a noticeable angular shift of the rainbow signal. The scattering angle increases when the shape of the droplet varies from round to oblate, whereas it decreases when the shape of the droplet varies from round to prolate. An example of the light paths of an oblate and a spherical droplet is displayed in **Figure 2.11**. The modification of the shape change on the rainbow angle is considered as follows.

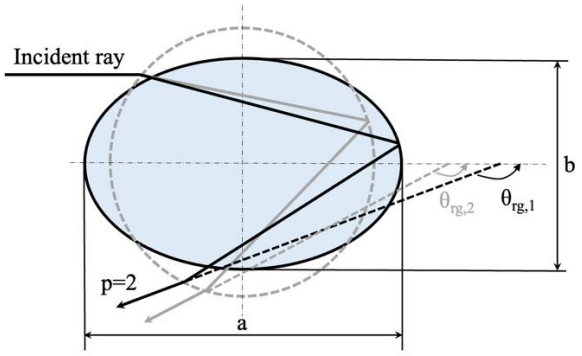

Figure 2.11 The light paths of an oblate and a spherical droplet.

The deviation of rainbow angle between the spheroidal and spherical droplets is given by [113, 120],

$$\Delta\theta_{\mathrm{rg}} = \theta_{\mathrm{rg},1} - \theta_{\mathrm{rg},2} = -16 \cdot \frac{\xi - 1}{\xi + 1} \cdot \sin\beta \cos^3\beta \times \cos\theta_{\mathrm{rg},2}, \quad (2.26)$$

where $\theta_{rg,1}$ and $\theta_{rg,2}$ are the rainbow angles for spheroidal and spherical particles, respectively. ξ is the droplet non-sphericity defined by $\xi = b/a$ with a is the equatorial length in the horizontal plane and b is the polar length in the vertical plane. For droplets with refractive index n, β is given by,

$$\beta = \sin^{-1}\sqrt{\frac{\left(4 - n^2\right)}{3n^2}}. \quad (2.27)$$

In some cases, the impact of shape change is significant on the accuracy of data inversion process. For instance, when performing the comparison between experimental data and simulation results, one can assume an appropriate non-sphericity to minimize the deviations and improve the accuracy of extracted data from experiment.

2.2 Physical properties and correlations with rainbow patterns

2.2.1 Basic physical properties

Ethanol and n-heptane have been chosen as test liquid in the present work. **Table 2.3** listed some of the main features of tested fuel.

Table 2.3 Major parameters of tested liquids.

	Ethanol	Heptane
Formula	C2H6O	C7H16
Molecular Weight (g/mol)	46.07	100.2

Boiling point (°C)	78.2	98.5
Critical temperature (°C)	240	266
Critical pressure (bar)	61.48	21.1
Density 20 °C (g/mol)	790	680
Latent heat (kJ/mol)	42.32	36.57
Refractive index at 20 °C	1.3611	1.3855

2.2.2 Refractive index range of ethanol

Evaluating the refractive index under different temperatures, pressure, wavelength, or other parameters is critical for extracting the information of the temperature and composition. It has a decisive role in the rainbow measurement methods. Understanding the variation of refractive indices of common liquid and fuels is helpful for data processing.

Taking ethanol for an example, to investigate the variation of the refractive index under different ambient conditions, three sets of reference data by Rosen [121], Chen and Vedam [122], and Jiménez Ricobóo [123] are compared here. Additionally, the relationship between the refractive index n and the temperature T proposed by Smith et al. [119] is plotted for comparison as well,

$$n = 1.36929 - 0.000400T\,, \tag{2.28}$$

The results and the corresponding data are shown in **Figure 2.12** and **Table 2.4**, respectively. First of all, it shows that increase temperature leads to a smaller refractive index, while larger pressure slightly increases the refractive index. This relates closely to the density variation as enhancing temperature normally leads to the reduction of density while increasing pressure induces a larger density. Besides, a linearly decreasing trend of the refractive index with a higher temperature is observed. By contrast, a non-linear variation trend of the refractive index with increasing pressure is presented. A variation of the refractive index with 0.001 corresponds to a change of temperature of about 2.5 K.

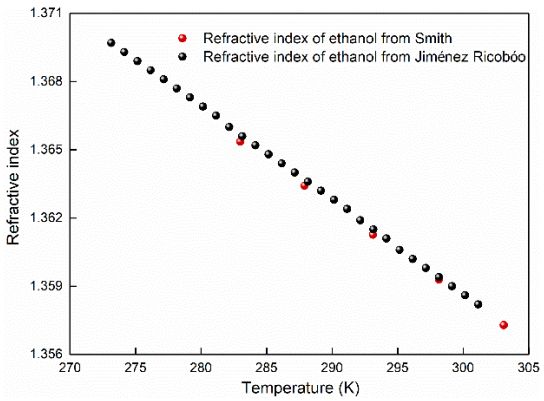

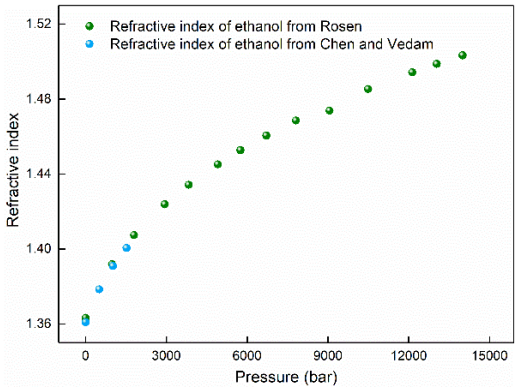

(a) Effect of temperature on refractive index **(b) Effect of pressure on refractive index**

Figure 2.12 Variation of the refractive index with pressure and temperature for ethanol: (a) data obtained by Jiménez Ricobóo and Smith [123] [119]; (b) data obtained by Rosen [121], Chen and Vedam [122].

Table 2.4 Refractive index of ethanol [119].

Temperature (K)	Refractive index value	Rainbow angle
283.15	1.36536	142.4047
287.15	1.36342	142.148
293.15	1.36126	141.8604
298.15	1.35929	141.5966
303.1	1.35729	141.3271

2.2.3 Refractive index of alkane fuels

K.Kerl and H.Varchmin [124] measured precisely the real refractive index of water and the alkanes cyclohexane, pentane, hexane, heptane, and octane with the wavelength and temperature of 326- 644 nm and 293-333 K. They fitted the measured data with the formula [124]:

$$n(\lambda,T) = a_1 + b_1 T + \frac{a_2 + b_2 T}{\lambda} + \frac{a_3 + b_3 T}{\lambda^2}, \tag{2.29}$$

with a_1, a_2, a_3, b_1, b_2, b_3 are constants. Their values are listed in **Table 2.5**.

Table 2.5 Fitting constants of above equation [124]**.**

Parameters	n-Hexane	n-Heptane	n-Octane
a_1	1.52157227	1.53032446	1.53411519
a_2	-4.6005	-4.9283	-5.9374
a_3	6159.3	6338.7	6615.0
$10^4 \times b_1$	-5.5035	-5.0456	-4.8297
$10^3 \times b_2$	2.2803	2.9848	4.9412
b_3	-5.9360	-5.9876	-6.2085

Take the incident wavelength of 0.532 μm as an example, the dependence of the refractive index on temperature for different alkanes fuels is displayed in **Figure 2.13**. The results reveal an inverse relationship between the refractive index and temperature. Overall, a linearly decreasing trend of refractive index with higher temperature is observed for all three alkane fuels. In addition, the sensitivity of three alkane fuels with temperature is almost the same. A variation of refractive index with 0.001 means a temperature difference of about 2 K for hexane, heptane, and octane. Moreover, the heavier the fuel, the larger the refractive index, which holds under all temperatures. Apart from that, the refractive indices together with the rainbow angle under different temperatures for heptane are listed in **Table 2.6** to provide a coarse range of the rainbow angle region.

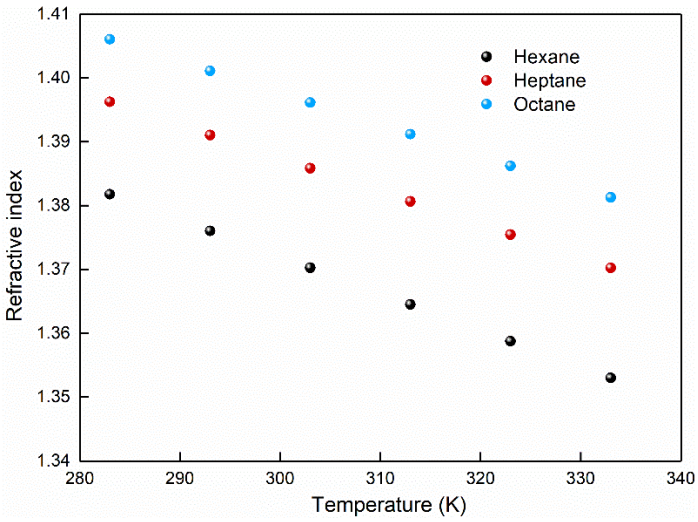

Figure 2.13 The dependence of the refractive index with temperature for three alkane fuels.

Table 2.6 Refractive index and rainbow angle of heptane.

Temperature (K)	Refractive index (heptane)	Rainbow angle (heptane)

283.15	1.396267	146.3038
293.15	1.391066	145.6719
303.15	1.385865	145.0304
313.15	1.380664	144.3792
323.15	1.375463	143.718
333.15	1.370262	143.0468

2.2.4 Refractive index of binary mixture

The prediction of the refractive index of the binary droplet is based on the refractive index of each component. The group contribution method is adopted for the evaluations of binary droplets. According to this method, the specific refraction $r^{(LL)}$ is calculated by the following equation [125-127],

$$r^{(LL)} = r_1^{(LL)} Y_1 + r_2^{(LL)} Y_2 , \tag{2.30}$$

where *Y* stands for the mass fraction. The subscripts *1* and *2* are the component number. The specific refraction of individual component *i* is computed by the Lorentz-Lorenz equation [127],

$$r_i^{(LL)} = \left(\frac{n_i^{\,2} - 1}{n_i^{\,2} + 2} \right) \frac{1}{\rho_i} , \tag{2.31}$$

Following this equation, the refractive index of the mixture is,

$$r = \sqrt{\frac{1 + 2\rho_l r^{(LL)}}{1 - \rho_l r^{(LL)}}} . \tag{2.32}$$

2.2.5 Dependence of scattering patterns on individual particle

The dependence of scattering patterns on the refractive index and droplet size has been exemplified in **Figure 2.14**. As indicated, variation of particle size does not change the primary rainbow position but alters the frequency of the supernumerary rainbows. That is the bigger the particle is, the higher the peak frequency is. Therefore, the distance between two neighboring peaks is smaller by increasing the droplet diameter. In contrast, the refractive index affects the angular position of the scattering light patterns. A larger refractive index moves the whole light intensity curve to a larger

scattering angle region. Therefore, it is reasonable to conclude that by measuring the rainbow position, we can predict the refractive index, while the relative angular distance between supernumerary rainbows relates to the particle diameter.

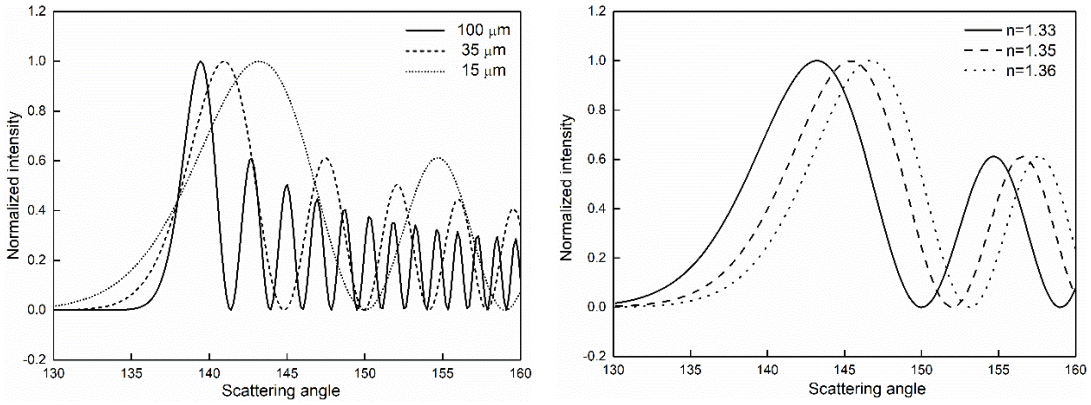

(a) *n*=1.33 **(b) d=15 μm**

Figure 2.14 The scattering intensity distribution with different particle sizes and refraction index.

The relationship between the rainbow angle θ_{rg} and the refractive index is quantitatively evaluated from Descartes theory. Theoretically, the rainbow angle depends on the refractive index and the types of rays. A given number of p=2 induces eq. (2.10). The correlation is presented in **Figure 2.15**. As indicated, the rainbow angle is proportional to the refractive index for a given rays type.

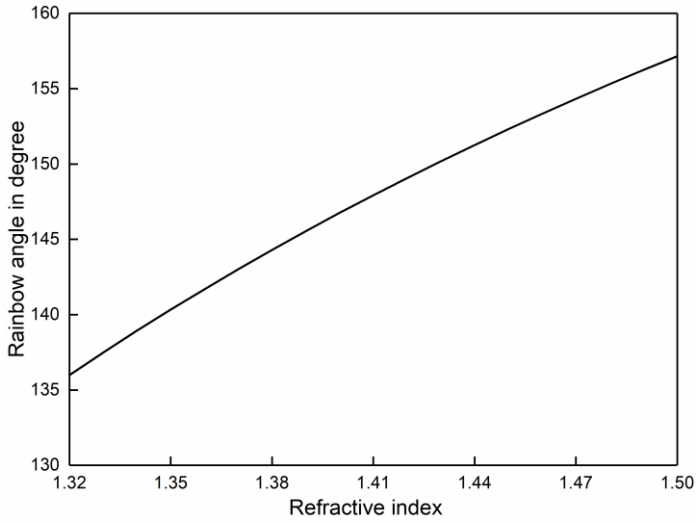

Figure 2.15 The relationship between the scattering rainbow angle and the refractive index.

2.3 Post-processing process

The recorded signal from the experiment contains the information of refractive index and diameter. To interpret the rainbow measurements, the theoretical prediction of the scattering field distribution from droplets is necessary. The procedure is to choose the optimum simulated curve with the experimental results, which is the so-called post-processing process. **Figure 2.16** illustrates the procedures and operations of the post-processing. In the first, the recorded scattering images with good quality are chosen to compute the candidate light intensity curves by averaging 20 lines of light intensity curves in the center of scattering images. Those candidate light intensity curves are calibrated by angular to convert the pixels into angle values. After that, the preprocessing process is operated on the calibrated candidate curves. This leads to a smoothed light intensity curve without any ripple structure yet maintaining the features of the first and second peaks, from which the angular position of the first and second main peaks of θ_1 and θ_2 can be obtained. Finally, the optimization process of the simulated light intensity curve is conducted by comparing it against the experimental results. The details of each process are described as follows.

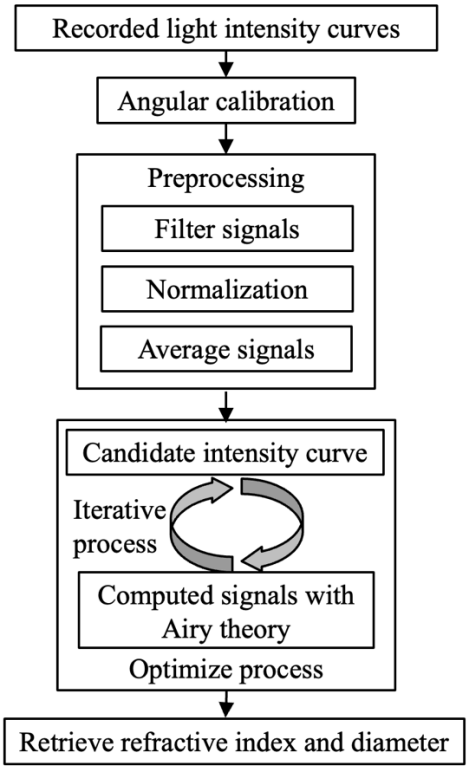

Figure 2.16 The flow chart of the post-processing.

2.3.1 Typical scattering light patterns by experiment

Figure 2.17 compares the typical scattering light patterns at the rainbow angle of the droplet stream. The primary peak together with the first Airy fringes is recorded in the visualization area. In addition, the images present clear and stable high-frequency ripple structures inside each peak, which indicates the stability of the droplet stream. Compared with the rainbow signal recorded under a continuous laser, the horizontal structure appears in the image illuminated by a pulsed laser. This behavior is due to the interference of the scattering light between the neighboring droplets inside the measurement volume. It has been proved that the particle size and the refractive index are independent of illumination type. In addition, the discontinuous aspect in the scattering image can be used to estimate the numbers of the particle as well as the relative distance between the particles in the control volume [128].

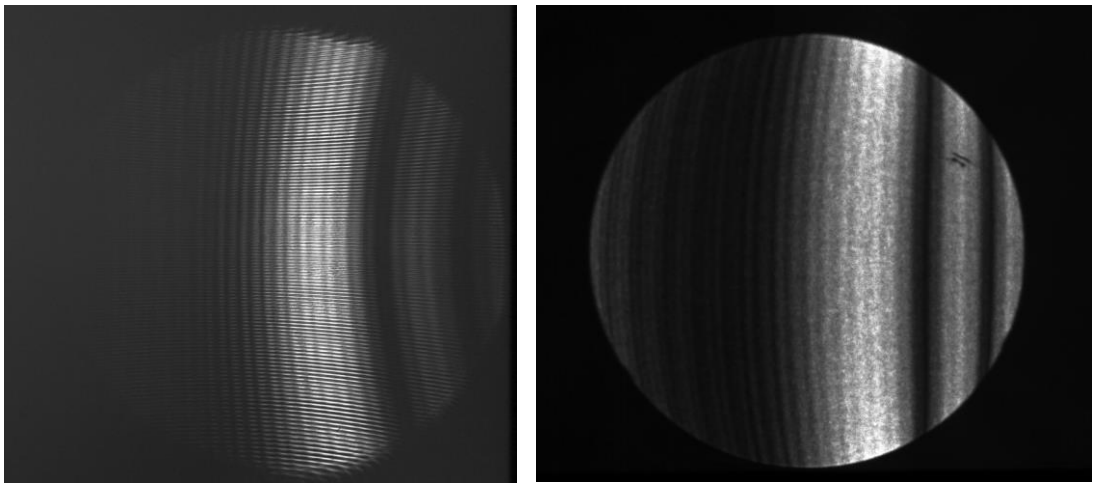

(a) Image by a pulsed laser **(b) Image by a continuous laser**

Figure 2.17 Rainbow signal of ethanol droplets at the atmospheric pressure and temperature condition; (a) illuminated by a pulsed laser; (b) by using continuous illumination. (The diameter of the pinhole is 100 μm, the excitation frequency and injection pressure are 13.39 kHz and 1.2 bar respectively).

After obtaining the scattering image, the light intensity curves can be extracted by averaging a given number of 20 horizontal lines over the central region of the pattern, as indicated in **Figure 2.18**a. This process aims to reduce the noise of the intensity curve and get a relatively smooth curve in **Figure 2.18**b.

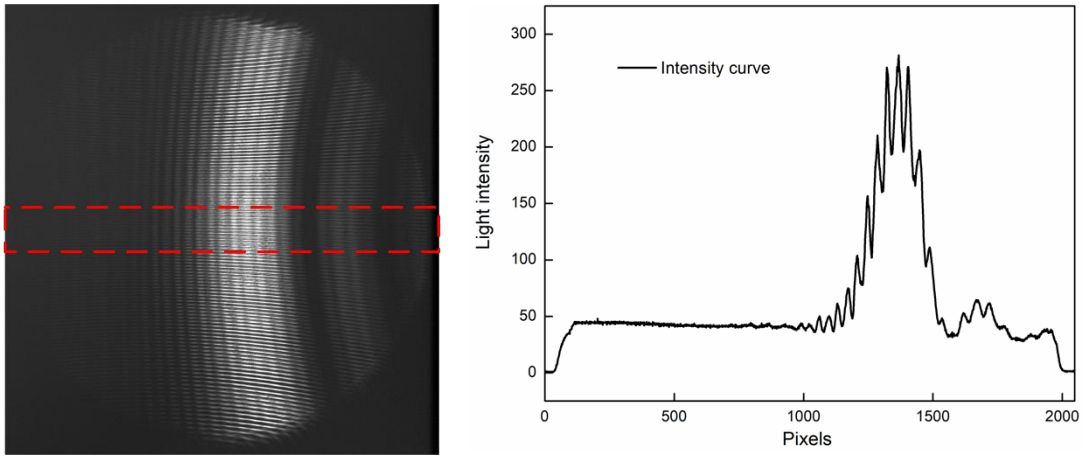

(a) Image patterns **(b) Intensity curve with pixels**

Figure 2.18 The intensity curve averaged over 20 lines along the center.

2.3.2 Angular calibration

Before conducting the data inversion process, it is necessary to perform the angular calibration by converting the pixels into the angles. The accuracy of the calibration process directly determines the precision of the extracted information from droplets. The principle of this method is the collection of the reflected images of the laser beam by a mirror. The mirror is placed at the same position as the droplet stream. The camera records the reflections of the laser beam at different angles by changing the angles of the mirror. Accordingly, the dependence of the image pixels on the angles can be derived through the plateau in the scattering light intensity curve. Restricted by the visualization area, four or five angle points are measured for each calibration.

The light intensity curves at four angles are displayed in **Figure 2.19**a. The pixels corresponding to the highest light intensity for each case are extracted from those curves. The scatters are plotted in **Figure 2.19**b with the horizontal axis of pixels and a vertical axis of scattering angle. A linear formula is adopted to fit those scatters, which reveals the relationship between the scattering angle and the pixel. In this way, the pixels become angle information that can be utilized for the following post-processing. It is necessary to conduct the calibration before or after each experiment to ensure the reliability of the measured data.

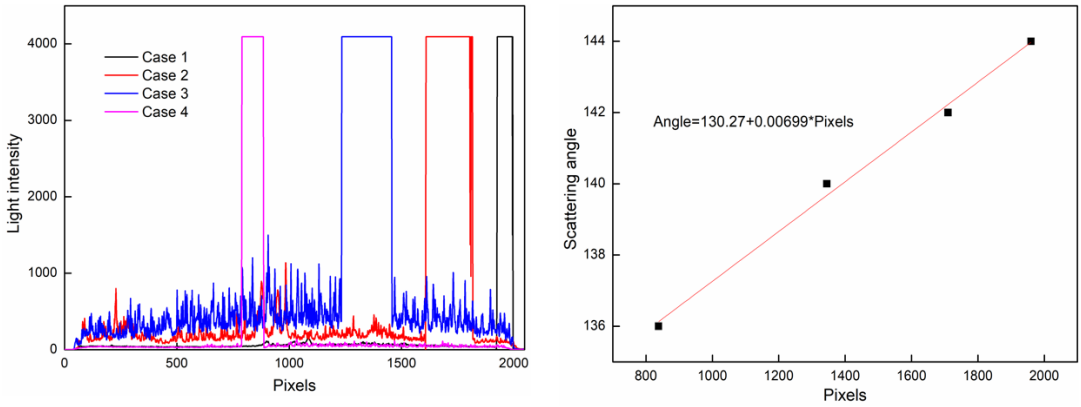

(a) Light intensity curve at four angles. **(b) The calibrated angle-pixels relation.**

Figure 2.19 Typical rainbow calibration signal; (a) The light intensity curves at four angles; (b) The relationship between angle and pixels.

2.3.3 Preprocessing

The pre-processing contains a series of operations. The first step is the filtering process, which aims to remove the ripple structure from the intensity curve and get the smooth Airy curves. This can be done by using the 'Local Regression Smoothing' in Matlab, which is based on the locally weighted linear regression method to get a smooth curve. The smoothed value is calculated from the adjacent data points inside the span by a regression weight function. Finally, the values are differentiated with appropriate regression functions, for instance, lowess scheme or loess scheme. The 'loess' scheme is adopted in this work as the quadratic fit has a better prediction of the intensity curve. The original intensity curve and the filtered curve are compared in **Figure 2.20**a. It is noted that the smoothed curve can be different according to the span. In literal, the span means the percentage of the total number of data points in the data set. Therefore, it has an impact on the accuracy of later procedures. The dependence of the filtered curves on the span value is shown in **Figure 2.20**b. It indicates that the value of span is paramount to the filtering curve. If the span is limited to an extremely small value, the high-frequency oscillation will be removed. While a larger value of span leads to a remarkable deviation of main peaks. By contrast, the spans with the value of 0.1 and 0.2 generate agreeable patterns with the experiment curve. They do not modify the position of main peaks and remove the ripple structure at the same time. Thus, it is reasonable to define the span range of 0.1-0.2.

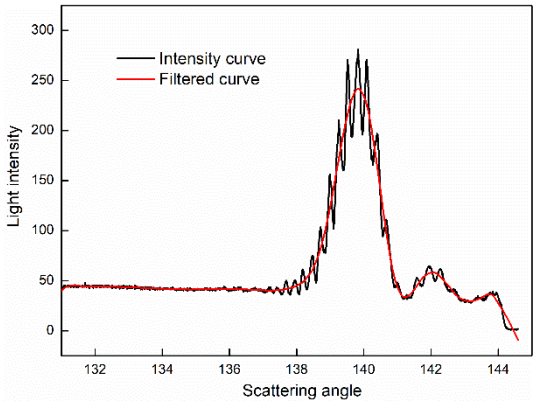

(a) The original signal pattern and filtered curve

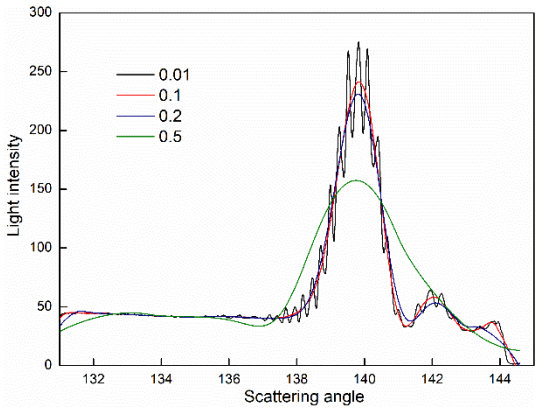

(b) The influence of different spans on the filter curves

Figure 2.20 An example of the smooth process by using different spans.

Noting that the normalized intensity curve can also provide a good avenue to check whether the condition of the generator is good enough to produce a stable droplet stream. As we use the pulsed laser as the illumination, the scattering patterns would be extremely sensitive to the shape as well as the position of droplets. Each tested condition records at least one hundred images to ensure that we get enough good data for each case. For example, the influence of injection pressure on the normalized intensity curves is compared in **Figure 2.21**. The normalized intensity curves generated by the injection pressure of 1.2 bar fit well with each other. By contrast, although each intensity curve with the injection pressure of 1.1 bar has the main peaks features, the angular position of each peak in each curve are not overlapped with each other. This means that either the droplet generator works under unstable conditions or this image is abnormal. In this case, those poor-quality data will be removed from the sample pool of further analysis. Likewise, the impact of excitation frequency on the intensity curve is checked in **Figure 2.22**. Four excitation frequencies ranging from 12 kHz to 17 kHz are compared. The excitation frequencies of 12 and 13.5 kHz produce good results, while higher frequency leads to the unstable main peaks positions. A reasonable agreement between the sampled intensity curves under each condition confirms the stability of the droplet generator under the present working condition, which also helps us choose the suitable data and dismiss the incorrect ones. In general, 10 images with good repeatability are chosen from the data set for further analysis.

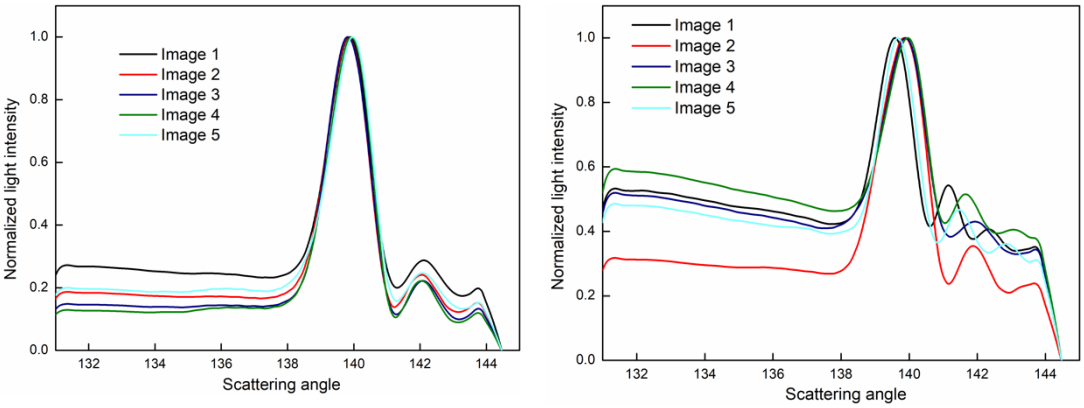

(a) Injection pressure of 1.2 bar **(b) Injection pressure of 1.1 bar**

Figure 2.21 The influence of injection pressure on the normalized intensity curves.

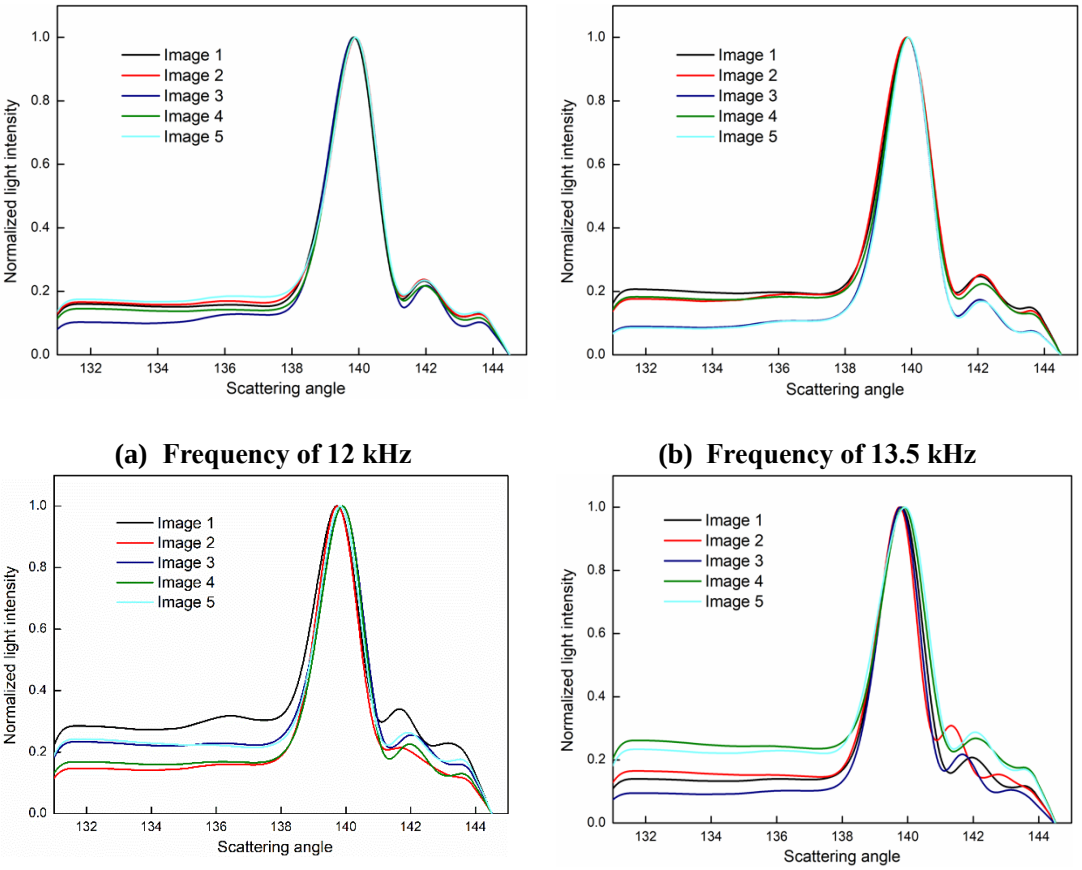

(a) Frequency of 12 kHz **(b) Frequency of 13.5 kHz**

(c) Frequency of 14 kHz **(d) Frequency of 17 kHz**

Figure 2.22 The influence of excitation frequency on the normalized intensity curves.

2.3.4 Optimization process

Extracting the droplet diameter and refractive index from the experimental measurements needs the help of the optimization process. Firstly, the smoothed intensity curves from the experiment are chosen as candidate data, from which the

angular position of the first and second main peaks of θ_1 and θ_2 can be obtained. The rainbow angle θ_{rg} can be computed from the θ_1 and θ_2 [43]:

$$\theta_{rg} = \left(\theta_1 - c\theta_2\right) / \left(1 - c\right), \tag{2.33}$$

with

$$c = \alpha_1 / \alpha_2, \tag{2.34}$$

where α_1=1.0874, α_2=3.4668.

Meanwhile, the rainbow angle also relates to the refractive index as follows:

$$\theta_{rg} = \pi + 2\cos^{-1}\left(\sqrt{\frac{n^2-1}{p^2-1}}\right) - 4\cos^{-1}\left(\sqrt{\frac{p^2(n^2-1)}{(p^2-1)n^2}}\right). \tag{2.35}$$

Therefore, the refractive index can be implicitly computed from the above equation after obtaining the rainbow angle from experimental measurements. Finally, the optimization process of the simulated light intensity curve is conducted by iteration. Taking the smoothed candidate curve as an object, a series of light intensity curves are computed with Generalized Airy Theory by changing the value of diameter. The values of θ_1 and θ_2 are the criteria to present the differences between the candidate curve and the simulated one, denoted as $\Delta\theta_1$ and $\Delta\theta_2$ respectively. When $\Delta\theta_1$ and $\Delta\theta_2$ are less than 0.0001, the corresponding simulated curve can be regarded as the optimum fitting curve. As a consequence, the droplet size and refractive index are simultaneously retrieved.

An example of the filtered experimental curve, the optimum fitting curve, and the other patterns are compared in **Figure 2.23**. Ethanol is chosen as the test liquid. The experiment is conducted at normal temperature and pressure conditions. The results indicate that even a small change of diameter or refractive index can be reflected in the shape or position of the rainbow patterns. The optimum fitting curve has the most satisfactory results with the experimental data. As a consequence, the corresponding information of refractive index and size are simultaneously retrieved with a diameter and refractive index of 206.74 μm and 1.359, respectively. Additionally, the rainbow patterns simulated by the Mie theory are compared with the original experimental data containing ripple structure to verify the accuracy of the predicted parameter. As shown in **Figure 2.23**b, the intensity curve predicted by the Mie theory with the optimum fitted diameter and the refractive index has a satisfactory prediction on the Airy fringes and

the ripple structure of experimental data. While some deviations can be observed for the other two cases. This proves the accuracy of the optimization process.

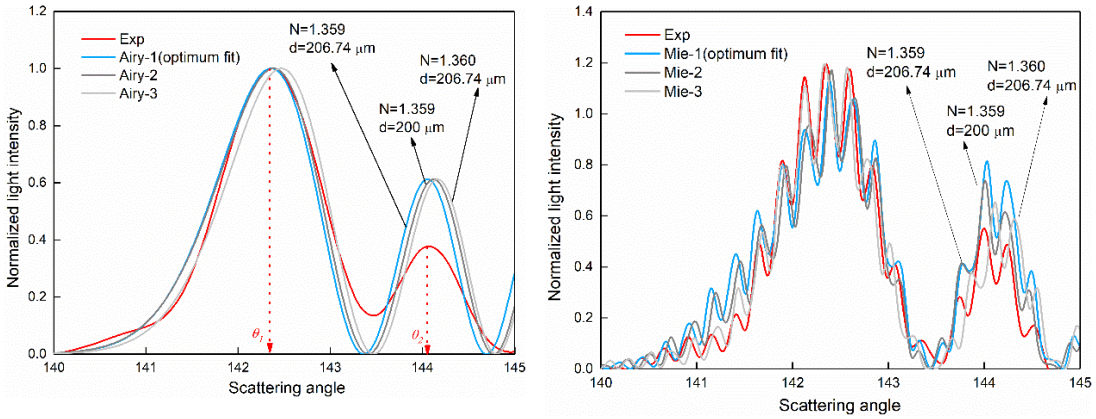

(a) Optimum fit of airy patterns **(b) Optimum fit of Mie patterns**

Figure 2.23 An example of the optimum simulated pattern and the comparison with the other patterns.

2.4 Stability and repeatability of measurement

2.4.1 Airy diameter and ripple diameter

Apart from the aforementioned iterative process to obtain the particle diameter, the other two diameter values named airy diameter D_{airy} and ripple diameter D_{ripple} could also be calculated from the experimental data. The airy diameter predicted by the airy peaks D_{airy} can be calculated by:

$$D_{airy} = \frac{\lambda}{4}\left[\left(\frac{(p^2-1)\sqrt{(p^2-N^2)}}{(N^2-1)^{3/2}}\right)^{1/2}\left(\frac{\alpha_1-\alpha_2}{\theta_1-\theta_2}\right)^{3/2}\right] \tag{2.36}$$

On the other hand, the ripple structure laying over the Airy fringes can be clearly identified from the experimental data as well as the corresponding peaks. It is believed that those ripple structures contain useful information on the particle diameter. The angular frequency spectrum of scattering light patterns is remarkably paramount for analyzing the relationship between the particle diameter and the ripple structure. An example of the spectrum of the monochromatic rainbow in **Figure 1.6** is depicted in **Figure 2.24**. The angular frequency F means the number of light intensity oscillations per degree. Each of the labeled peaks stands for the interference between two kinds of

geometric rays. Among them, we only focus on the three dominant peaks at frequencies F_1, F_2, and F_3 as they result from rays of external reflection and one internal reflection. Frequency F_1 is generated by the interference between the paralleled incident rays with the same scattering angle when they leave the droplet. F_2 and F_3 correspond to the interference between one-internally reflected rays and the external reflected ray. Peaks F_1 contributes to the Airy fringes while peaks F_2 and F_3 account mainly for the ripple structure laying over the Airy fringes [39].

According to Yong's fringe analysis, the ripple frequency can be found from the distance between the geometric rainbow ray at θ_{rg} and the externally-reflected ray at infinity [129]. It is believed that ripple frequency can be related to the droplet diameter in the following way:

$$F_{ripple} = \frac{D_{ripple}}{2\lambda}\left(\cos\tau_{rg} + \cos\frac{\theta_{rg}}{2}\right)\frac{\pi}{180^{\circ}}. \tag{2.37}$$

Noting that in practical case the spectrum comes from the Fourier transform over a finite range of scattering angles near the rainbow angle θ_{rg}. In this case, we could not judge the F_{ripple} directly from the rainbow spectrum as the peak at F_{ripple} will split into two peaks at angular frequencies F_2 and F_3. The ripple frequency has to be solved implicitly from angular frequencies F_2 and F_3. Subsequently, F_2 and F_3 hold:

$$\begin{aligned} F_2 &= F_{ripple} - 1/2\, F_{Airy}, \\ F_3 &= F_{ripple} + 1/2\, F_{Airy}, \end{aligned} \tag{2.38}$$

with F_{Airy} is the Airy frequency defined as:

$$F_{Airy} = \frac{1}{\theta_2 - \theta_1}. \tag{2.39}$$

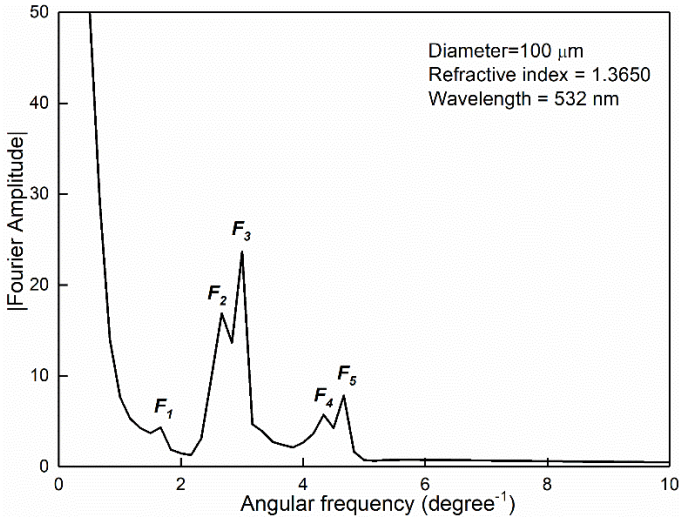

Figure 2.24 The spectrum of the monochromatic rainbow.

The validity of predicting the droplet diameter by eq.(2.37) is checked with Lorenz-Mie computations. **Figure 2.25** depicts the dependence of F_{ripple} on droplet diameter by varying the diameter from 20 to 400 μm. The incident wavelength and the refractive index are λ=532 nm and 1.3650, respectively. A near-linear relationship between the droplet diameter and ripple frequency is presented. In addition, the difference between two computations never exceeds 1% in the present range of diameter, which validates the accuracy of eq. (2.37) in evaluating the variation of ripple frequency against droplet size. Moreover, it is demonstrated that the ripple structure is an effective way to extract the droplet diameter, from which the ripple diameter is solved implicitly.

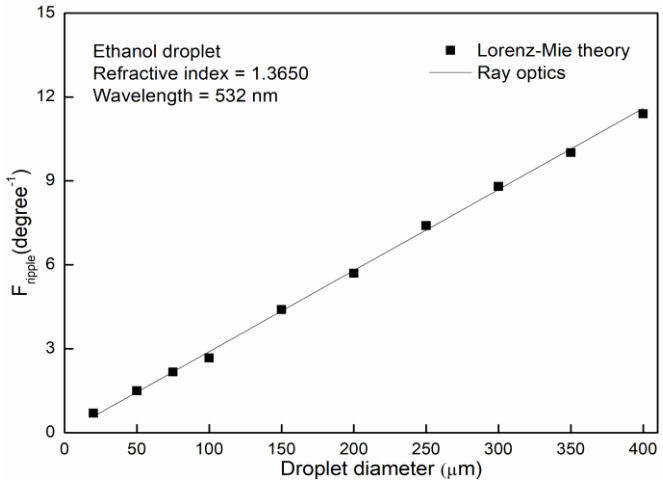

Figure 2.25 The ripple frequency evaluated by eq. (2.37) and the Lorenz-Mie theory as a function of the droplet diameter with a refractive index n=1.3650 and λ=532 nm.

2.4.2 Diameters evaluated by three methods

The possibility of obtaining three diameter values from the intensity curve has been validated previously. Theoretically, the diameters computed by three methods should be uniform with each other. As displayed in **Figure 2.26**, the predicted diameter values by ripple frequency and airy peaks are compared with the reference diameters. The sampled diameter varies from 20-400 μm with a constant refractive index of 1.3650. The scattering light patterns of droplets illuminated by an incident wavelength of 532 nm are computed with the Lorenz-Mie theory and Airy theory, respectively. Subsequently, the ripple diameter and airy diameter are derived from the ripple patterns and airy peaks. It is observed that the diameter values evaluated by the ripple frequency and airy peaks are in good agreement with the theoretical diameters, especially when the particle diameter is larger than 100 μm. In a practical case, the derived values by three methods might not be exactly the same with a limited error range. Regarding this, the diameter values predicted by two methods provide a good avenue to ensure the accuracy of the object diameter by iteration.

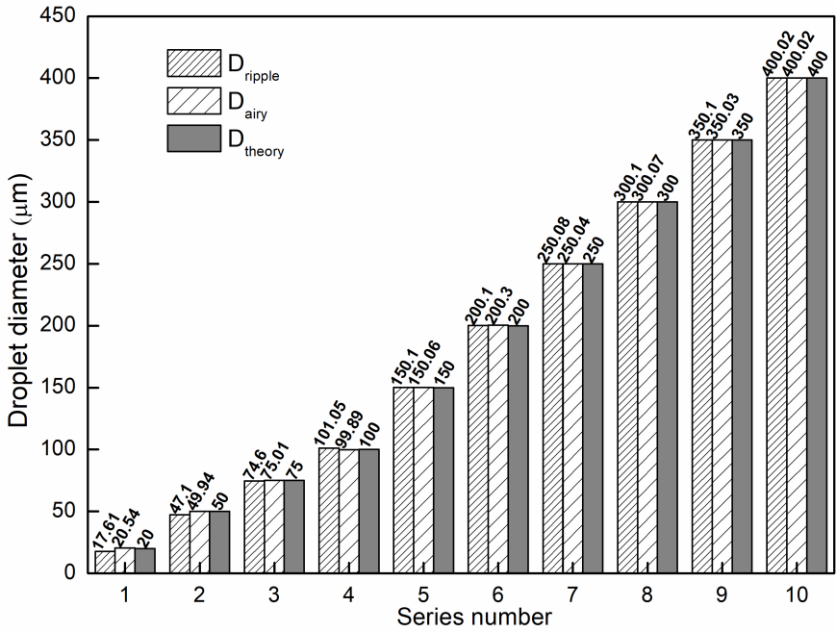

Figure 2.26 The comparison of the particle diameter derived by different methods and theoretical values.

The calculation of three diameters based on the experimental measurements is examined in **Figure 2.27**. The measurements are conducted over a vertical range of 20-

50 mm away from the nozzle under normal pressure and room temperature conditions. Ethanol droplet stream is produced from a pinhole with a diameter of 100 μm. In the first, the diameters evaluated by iteration, ripple frequency, and airy peaks are compared. As expected, the droplet size evaluated by three methods differs slightly when it comes to the experimental situation. Despite that, the ripple diameter and airy diameter offer a good reference for the iteration diameter as the final diameter obtained by iteration always lies between those two diameter values. The relative difference of ripple and airy diameter against the iteration diameter is also checked with no more than 3% of errors. This ensures the accuracy of diameter measurement by the present post-processing process.

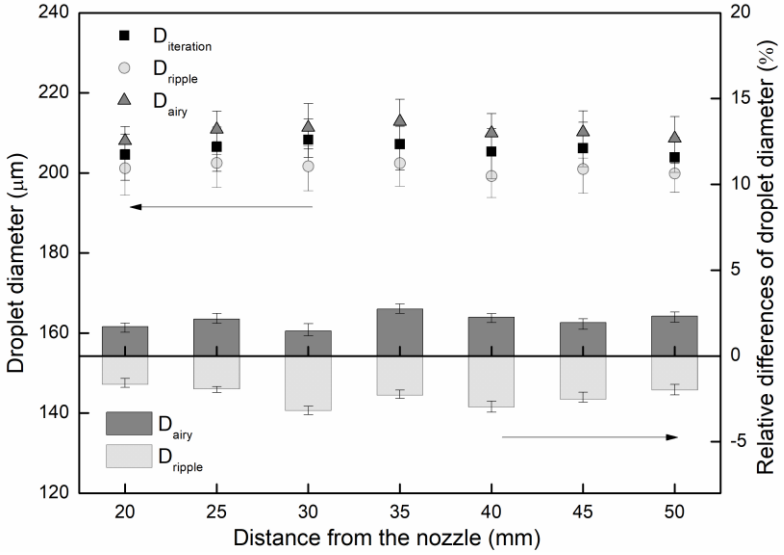

Figure 2.27 The diameter values by different methods with the pinhole size of 100 μm.

2.4.3 Droplet parameters under different conditions

Following that, the diameter and refractive index of ethanol droplets generated from three pinhole diameters of 50 μm, 75 μm, and 100 μm are compared in **Figure 2.28**. Firstly, as indicated, the diameter of droplets at different vertical positions conforms well to each other as the evaporation can be neglected under room temperature conditions. Apart from that, the refractive index of droplets at different locations is almost uniform. This proves the stability of the droplet stream and generator. Secondly, the uncertainty of the predicted droplet diameter is in the range of ±1 μm, which is quite small and almost invisible in the figures. Meanwhile, the refractive indices of droplets

at different vertical positions derived from the data inversion process have an average uncertainty of 0.002. The evaluation of both droplet size and the refractive index has a reasonable deviation range. Furthermore, the average diameters of droplets at different positions obtained by the post-processing are close to the theoretical values computed by eq. (2.7). **Table 2.7** compares the measured diameters and the theoretical predictions of the diameter according to the volume flow rate and the excitation frequency of the generator. Moreover, the temperature value computed from the refractive index consents well with the room temperature condition with a deviation of no more than 1 °C. Those insignificant discrepancies validate the precision of the data extraction method together with the stability of the droplet generation.

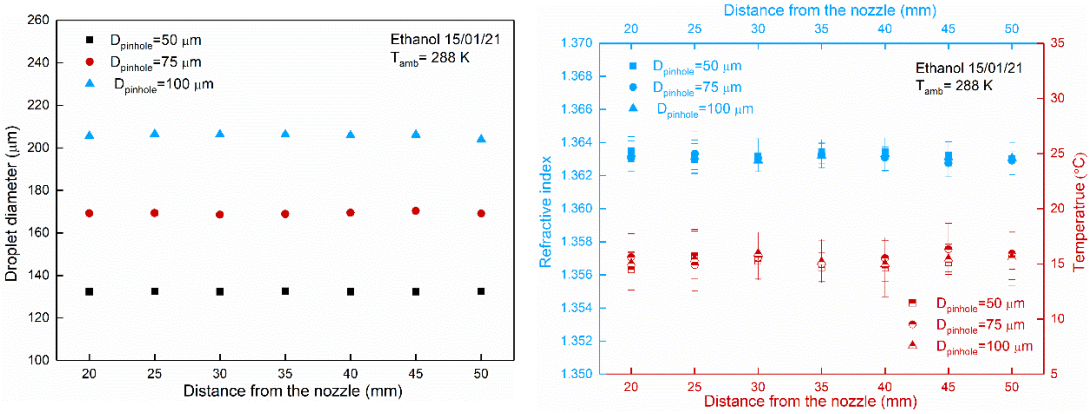

(a) Comparison of droplet size **(b) Comparison of refractive index**

Figure 2.28 Comparison of the diameter and refractive index by different nozzles of 50 μm, 75 μm, and 100 μm; (a) diameter; (b) refractive index and temperature.

Table 2.7 Comparison of the diameter value.

D (μm)	P_{inj} (bar)	Flow rate Q (m^3/s)	f_G (kHz)	Predicted droplet size (μm)	Measured droplet size (μm)
50	1.2	6.11	13.14	130.2671	132.62913
75	1.2	6.11	13.14	170.6982	168.35749
100	1.2	6.11	13.14	206.7861	205.57124

Besides ethanol, the impact of the pinhole diameter on the diameter and refractive index of heptane droplets have also been tested. Three pinhole diameters of 50 μm, 75 μm, and 100 μm are applied. The results and data are compared in **Figure 2.29** and **Table**

2.8. Similarly, an overall agreement of the stability of heptane droplets at different vertical positions is observed. This validates again the stability of the generator and measurement method.

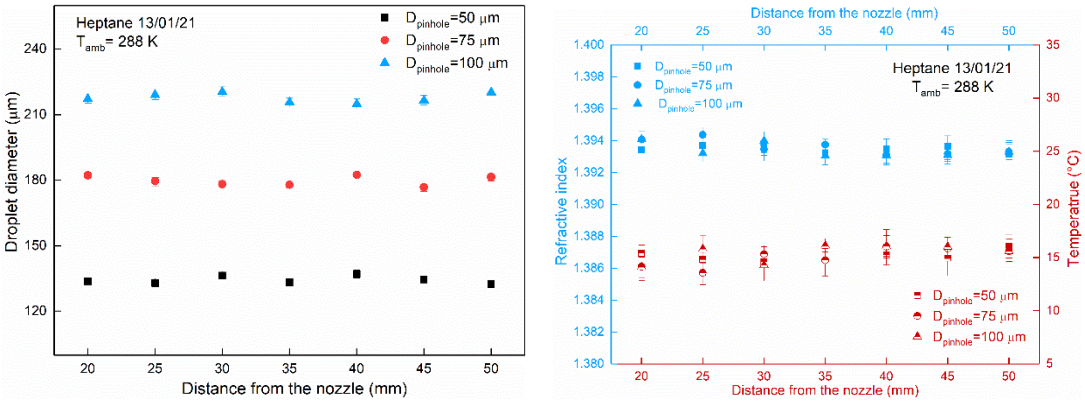

(a) Comparison of droplet size **(b) Comparison of refractive index**

Figure 2.29 Comparison of the diameter and refractive index of heptane by different nozzles of 50 µm, 75 µm, and 100 µm; (a) diameter; (b) refractive index.

Table 2.8 Comparison of the diameter value of heptane.

D (µm)	P_{inj} (bar)	Flow rate Q (m^3/s)	f_G (kHz)	Predicted droplet size (µm)	Measured droplet size (µm)
50	1.2	6.11	13.14	136.6181399	134.29593
75	1.2	6.11	13.14	179.0204072	179.77031
100	1.2	6.11	13.14	216.867779	217.708

2.4.4 Repeatability check

The repeatability of the rainbow measurement is checked by performing the experiment on three different days. The droplet streams of ethanol are produced under room temperature and normal pressure conditions by using three pinhole diameters of 50 µm, 75 µm, and 100 µm, respectively. **Figure 2.30** compares the variation of droplet diameter of three tests. The results indicate good repeatability of the experiment since the discrepancies of diameter values measured on different days are fairly small. In fact, the slight differences in the results could be interpreted from the aspects of different humidity and temperatures on different days. Apart from the diameter, the refractive indices and the resulting temperature values are compared in **Figure 2.31** as well. The

measured temperature value confirms well with the actual room temperature on that day. It can be concluded that the present rainbow measurement method is reproducible and reliable.

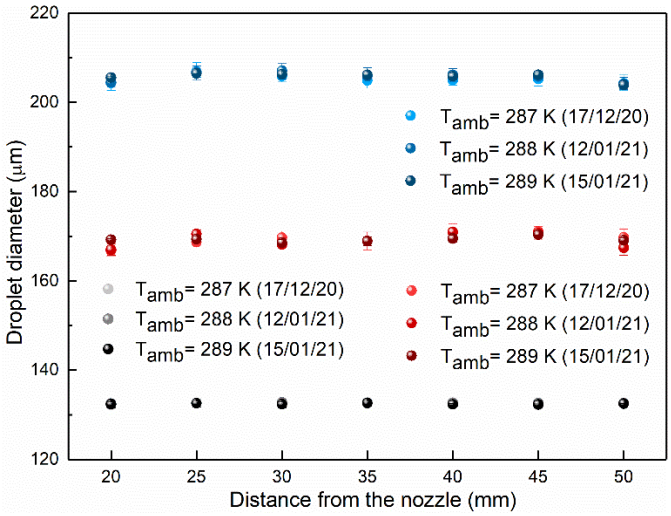

Figure 2.30 Comparison of the diameter of ethanol generated with three pinhole sizes on different days. (The black, red, and blue colour series of spheres are produced by the pinhole size of 50 μm, 75 μm, and 100 μm, respectively)

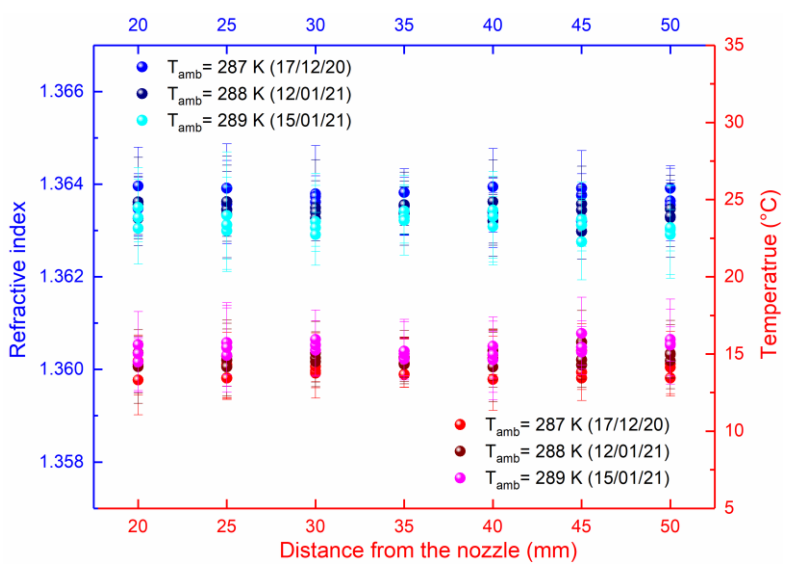

Figure 2.31 Comparison of the refractive indices and temperature values of ethanol on different days.

2.5 Summary

This chapter systematically describes the experimental methodology including the composition of the whole setup, the operation of each segment, the algorithm for data extraction. The physical parameters of the tested fuel and their dependence on temperature in the present work are introduced as well. The post-processing procedures are critical to extracting the droplet diameter and the refractive index from the scattering light intensity curve. The accuracy of the data inversion method is examined. The reliability and repeatability of the measurement method have been checked as well. The concluding remarks are summarized as below:

1. The droplet evaporation experimental system based on the rainbow technique has been designed and established, which is mainly composed of droplet generation, the high-temperature chamber, and the rainbow image system. A stable droplet stream can be obtained by adjusting the injection pressure and excitation frequency of the generator.
2. An inversion algorithm has been proposed to simultaneously extract the droplet diameter and temperature distributions from the scattering light patterns for the first time. The method improves the accuracy of the post-processing process by considering the impact of refractive index gradient and the modification of shape change on the rainbow angle.
3. The dependence of scattering patterns on diameter and refractive index has been revealed. The results indicate that the refractive index determines the angular position of the scattering light patterns while the diameter controls the frequency of main peaks.
4. The reliability and repeatability examinations have been made to ensure the accuracy of the rainbow measurement. The airy diameter and ripple diameter evaluated from the airy patterns and ripple structures are compared with the diameter obtained by iteration to verify the inversion algorithm.

3. Droplet evaporation model

3.1 Physical description and assumptions

Droplet evaporation theory is the description of the physical process of a liquid droplet in a high-temperature gas environment composed of the mixture of air and fuel vapor, as schematically presented in **Figure 3.1**. In order to analyze this physical process theoretically, the following assumptions have also been made:

1) The droplet is treated as spherically symmetric all the time. The influence of instability on droplet shape is neglected. Accordingly, the evaporation process is simplified into a one-dimensional issue. All of the parameters such as temperature, radius, and mass fraction change along the radial direction with time. This assumption is validated for the vaporization of small droplets under a quiescent environment [130]. Respecting that the case investigated in this work is the droplets with a diameter of 50 μm, it is reasonable to take it as spherically symmetric.
2) The heat and mass transfer processes in the gas phase are in quasi-steady-state. The fact is that the magnitude of characteristic time for gas diffusion is two or three orders less than the value for liquid heat up and mass diffusion [131]. Consequently, it is justified to regard the heat and mass transportations in the gas phase as quasi-steady. By contrast, those processes inside the droplet are unsteady.
3) The liquid and gas phases at the droplet interface maintain the thermodynamic equilibrium state. The fuel vapor at the interface between the liquid and gas phase is assumed to be at the saturated state. Accordingly, the mass transfer at the droplet surface is at the diffusion-controlled mode [132].
4) The solution of the gas phase into the liquid phase is neglected, which is reasonable for the subcritical condition.

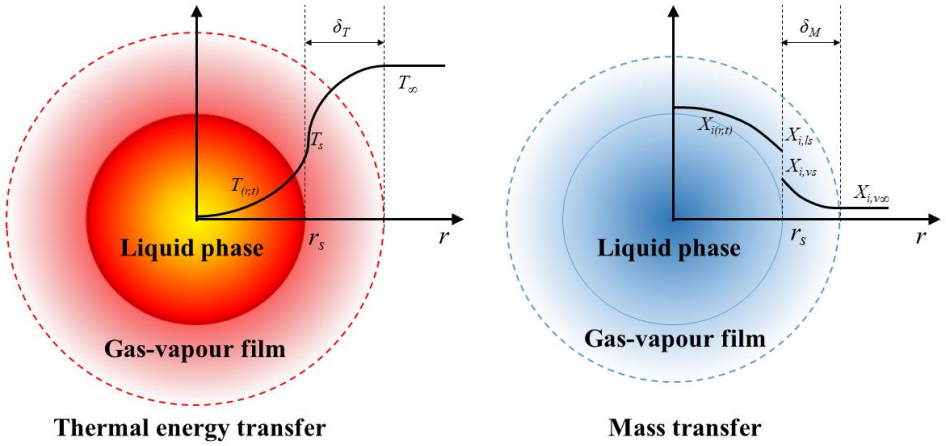

Figure 3.1 Schematic representation of an evaporating droplet.

3.2 Simulations of the evaporation process

3.2.1 Spalding mass transfer number

Mass regression rate is originated from the Maxwell equation:

$$\dot{m}_{\mathrm{d}} = 4\pi r^2 D_{\mathrm{v}} \frac{d\rho_{\mathrm{v}}}{dr}, \tag{3.1}$$

$$\dot{m}_{\mathrm{d}} \frac{dr}{r^2} = 4\pi D_{\mathrm{v}} d\rho_{\mathrm{v}}, \tag{3.2}$$

with $\dot{m}_{\mathrm{d}}$ is the mass diffusion rate and ρ_v is the vapor density. An integral of this equation from droplet surface to infinity leads to:

$$\dot{m}_{\mathrm{d}} = -4\pi r_{\mathrm{s}} D_{\mathrm{v}} (\rho_{\mathrm{vs}} - \rho_{\infty}), \tag{3.3}$$

When considering the diffusion induced by the velocity of vapors, the Maxwell equation is formulated as:

$$\begin{aligned} \dot{m}_{\mathrm{d}} &= 4\pi r^2 (D_{\mathrm{v}} \frac{d\rho_{\mathrm{v}}}{dr} - \rho_{\mathrm{v}} U) \\ &= 4\pi r^2 (D_{\mathrm{v}} \frac{d\rho_{\mathrm{v}}}{dr} - D_{\mathrm{g}} \frac{\rho_{\mathrm{v}}}{\rho_{\mathrm{g}}} \frac{d\rho_{\mathrm{g}}}{dr}) \end{aligned}, \tag{3.4}$$

Assuming $D_{\mathrm{v}} = D_{\mathrm{g}}$, and $\rho_{\mathrm{g}} = \rho_a + \rho_{\mathrm{s}} = const$, it derives:

$$\dot{m}_{\mathrm{d}} = -4\pi r_{\mathrm{s}} D_{\mathrm{g}} \rho_{\mathrm{g}} \ln(1 + B_{\mathrm{M}}), \tag{3.5}$$

with B_M stands for the Spalding mass number.

3.2.2 Spalding heat transfer number

According to the energy conservation law, the energy coming from the environment is mainly classified into three sections, i.e., the heating in the liquid phase, the heating in the gas phase, and the latent heat.

$$4\pi r^2 k_{\mathrm{g}} \frac{dT}{dr} = Q_l - \dot{m}_{\mathrm{d}} c_{p,\mathrm{v}} \left(T - T_{\mathrm{s}}\right) - \dot{m}_d L\left(T_{\mathrm{s}}\right), \tag{3.6}$$

$$\int_{T_s}^{T_{\mathrm{inf}}} 4\pi k_{\mathrm{g}} \frac{dT}{c_{p,\mathrm{v}} \left(T - T_{\mathrm{s}}\right) + L\left(T_{\mathrm{s}}\right) - Q_l / \dot{m}_{\mathrm{d}}} = \int_{R_d}^{\infty} -\dot{m}_{\mathrm{d}} \frac{dr}{r^2}\ , \tag{3.7}$$

with k_g is the conductivity of the gas-vapor mixture in the boundary layer. Q_l is the instantaneous heat flux absorbed by the liquid phase. $C_{p,v}$ is the specific heat capacity of vapor at the droplet surface. L is the latent heat of vaporization.

Setting $B_{\mathrm{T}} = \dfrac{c_{p,\mathrm{v}} \left(T_\infty - T_{\mathrm{s}}\right)}{L\left(T_{\mathrm{s}}\right) - Q_l / \dot{m}_{\mathrm{d}}}$ is the heat transfer number, the evaporation rate evolves into:

$$\dot{m}_{\mathrm{d}} = -\frac{4\pi k_{\mathrm{g}} r_{\mathrm{s}}}{c_{p,\mathrm{v}}} \ln(1 + B_{\mathrm{T}})\,, \tag{3.8}$$

For stationary droplet:

$$Sh = Sh_0 = 2\,, \tag{3.9}$$

$$Nu = Nu_0 = 2\,. \tag{3.10}$$

Finally, for non-vaporization stationary droplets, the evaporation rate follows:

$$\dot{m}_{\mathrm{d}} = \begin{cases} -\pi d \rho_{\mathrm{g}} D_{\mathrm{g}} Sh \ln(1 + B_{\mathrm{M}}) \\ -\pi d k_{\mathrm{g}} Nu \ln(1 + B_{\mathrm{T}}) / c_{p,\mathrm{v}} \end{cases}. \tag{3.11}$$

3.2.3 Evaluation of interfacial evaporation

Evaluation of interfacial evaporation aims to solve the heat and mass transfer rate between a single droplet and the environment. The evaporation rate for a multi-

component droplet is formulated as [132]:

$$\dot{m}_d = \sum_{i=1}^{n} \dot{m}_i = \begin{cases} -2\pi r \rho_v D_v Sh^* \ln(1+B_M) \\ -2\pi r k_v Nu^* \ln(1+B_T)/c_{p,v} \end{cases}, \tag{3.12}$$

with $\dot{m}_d$ is the evaporation rate. the subscript i denotes component i. The ρ_v, D_v, k_v, and $c_{p,v}$ are density, diffusion coefficient, conductivity coefficient, and specific heat of fuel vapor mixture at droplet surface, respectively. B_M and B_T stand for the Spalding mass and heat transfer number [133]:

$$B_M = \frac{Y_{vs} - Y_{v\infty}}{1 - Y_{vs}}, \tag{3.13}$$

$$B_T = \frac{c_{p,v}(T_\infty - T_s)}{(L - \dot{Q}_l/\dot{m}_d)}, \tag{3.14}$$

where Y_{vs} and $Y_{v\infty}$ represent the mass fraction of the vapor mixture at droplet surface and ambient, respectively. L is the latent heat. In general, the relationship between the Spalding heat and mass transfer number is [82],

$$B_T = (1+B_M)^{\phi} - 1, \tag{3.15}$$

where

$$\phi = \left(\frac{c_{p,v}}{c_{p,g}}\right)\left(\frac{Sh^*}{Nu^*}\right)\frac{1}{Le}. \tag{3.16}$$

Noting that the Sh^* and Nu^* appeared in the equations above are the modified Sherwood number and Nusselt number mentioned above. Le is the Lewis number [82]:

$$Le = \frac{k_g}{\rho_g D_g c_{p,g}}. \tag{3.17}$$

3.2.4 The heat and mass transfer in the liquid phase

The temporal and spatial advancement of temperature and mass fraction can be calculated by solving the following transient heat conduction and mass diffusion equations [134]:

$$\begin{aligned}\rho_l c_{p,l}\frac{\partial T_l}{\partial t}&=\frac{1}{r^2}\frac{\partial}{\partial r}(k_{eff}r^2\frac{\partial T_l}{\partial r})\\ \frac{\partial Y_{i,l}}{\partial t}&=\frac{1}{r^2}\frac{\partial}{\partial r}(D_{eff}r^2\frac{\partial Y_{i,l}}{\partial r})\end{aligned}, \tag{3.18}$$

where ρ_l is the liquid density, T_l is the liquid temperature, $c_{p,l}$ is the specific heat of the liquid phase, r is the droplet radical coordinate values. k_{eff} and D_{eff} denote the effective thermal conductivity coefficient and diffusivity coefficient, $Y_{i,l}$ is the liquid mass fraction of each component.

The initial and boundary conditions provided for the above equations are as follows,

$$T_l(r,0)=T_0,\ Y_{i,\mathrm{l}}(r,0)=Y_{i,l}(0)\,, \tag{3.19}$$

$$\left.\frac{\partial T_l}{\partial r}\right|_{r=0}=0,\ \left.\frac{\partial Y_{i,l}}{\partial r}\right|_{r=0}=0\,, \tag{3.20}$$

$$\left.\frac{\partial T_l}{\partial r}\right|_{r=r_s}=\frac{\dot{Q}_l}{4\pi r^2 k_{eff}},\ \left.\frac{\partial Y_{i,l}}{\partial r}\right|_{r=r_s}=\frac{\dot{m}_d(Y_{i,ls}-\varepsilon_i)}{4\pi r^2 D_{eff}}\,, \tag{3.21}$$

where $\dot{Q}_l$ is the instantaneous heat flux absorbed by the liquid phase, and $\varepsilon_i=Y_{i,vs}\big/\sum_i Y_{i,vs}$. To account for the effects of droplet internal circulation, thermal conductivity k_l and diffusion coefficient D_l are multiplied by correction factor χ_k and χ_D to calculated effective conductivity k_{eff} and effective diffusivity D_{eff}, as $k_{\mathrm{eff}}=\chi_k k_{\mathrm{l}},\ D_{\mathrm{eff}}=\chi_D D_{\mathrm{l}}$. The correction factors range from 1 to 2.72 and are calculated as followed:

$$\begin{aligned}\chi_k&=1.86+0.86\tanh[2.245\log_{10}(Pe_{\mathrm{l}}/30)]\\ \chi_D&=1.86+0.86\tanh[2.245\log_{10}(Re_{\mathrm{l}}Sc_{\mathrm{l}}/30)]\end{aligned} \tag{3.22}$$

3.2.5 The vapor-liquid equilibrium (VLE)

Considering the case of a single cold droplet evaporating in a hot environment, it is assumed that the evaporation process at the interface is thermodynamically equilibrium. With this assumption, we can evaluate the species molar fraction in the vapor phase at the interface from the liquid phase parameters, as stated in Raoult's law [135],

$$X_{i,vs} = X_{i,ls} \cdot p_{i,sat} / p\,, \tag{3.23}$$

where $X_{i,vs}$ and $X_{i,ls}$ present the vapor and liquid molar fraction of component i at the droplet surface. $p_{i,sat}$ is the saturated vapor pressure. However, the above equation treats the gas phase as the ideal gas, and the liquid phase is an ideal mixture. Some non-ideal factors have to be taken into consideration when it comes to practical conditions.

3.3 Correction factors

3.3.1 Convective evaporation and heating

The airflow is taken as one dimension to implement into the model. The flow direction is parallel to the free-falling direction of the droplet. The motion of droplet is evaluated by [82]:

$$\frac{dU}{dt} = \frac{3C_{\mathrm{D}}}{2r_{\mathrm{s}}}\left(\frac{\rho_{\infty}}{\rho_{l}}\right)|U_{\infty} - U|(U_{\infty} - U)\,, \tag{3.24}$$

where U and ρ_l are the droplet velocity and density in the liquid phase. U_∞ and ρ_∞ are the velocity and density of airflow. r_s is the droplet radius. C_D is the drag coefficient relating with Reynolds number [79]:

$$C_{\mathrm{D}} = \frac{24}{\mathrm{Re}_{g}}\left(1 + \frac{\mathrm{Re}_{g}^{\,2/3}}{6}\right), \tag{3.25}$$

$$\mathrm{Re}_{g} = \frac{2r_{s}\left|U_{\infty} - U\right|\rho_{\infty}}{\mu_{g}}, \tag{3.26}$$

with Re_g is Reynold number in the gas phase and μ_g is the viscosity of the vapor.

The modification is necessary for the convective evaporation situation to consider the impact caused by the relative motion between droplet and ambient gas. The ‘film theory’ is adopted to consider the influence of airflow on the transport process. It assumes a thermal and concentration boundary layer surrounding the droplet to account for the resistance of heat and mass transfer between the liquid phase and the airflow [82]. The heat and mass transport in the boundary layer is at a balanced state. For the heat transfer process, the energy transfer occurred in the boundary layer equals to the heat transfer between droplet surface and environment:

$$\frac{Q_{\mathrm{L}}}{4\pi r_{\mathrm{s}}^2}\frac{k_{\mathrm{g}}(T_\infty - T_{\mathrm{s}})}{r_{\mathrm{s}} - \dfrac{r_{\mathrm{s}}^2}{r_{\mathrm{s}} + \delta_{\mathrm{T0}}}} = h(T_\infty - T_{\mathrm{s}}). \tag{3.27}$$

Consequently, the thickness of the thermal boundary layer is defined as:

$$\delta_{\mathrm{T0}} = \frac{2r_{\mathrm{s}}}{Nu_0 - 2}. \tag{3.28}$$

Similarly, the thickness of the mass boundary layer is calculated as:

$$\delta_{\mathrm{M0}} = \frac{2r_{\mathrm{s}}}{Sh_0 - 2}, \tag{3.29}$$

where Sh_0 and Nu_0 stand for the Sherwood number and Nusselt number of droplets without evaporation. The thickness of the boundary layer affected by the Stefan flow is considered by the following factors [82]:

$$F_{\mathrm{T}} = \delta_{\mathrm{T}} / \delta_{\mathrm{T0}}, \tag{3.30}$$

$$F_{\mathrm{M}} = \delta_{\mathrm{M}} / \delta_{\mathrm{M0}}. \tag{3.31}$$

They can be calculated with the Spalding heat and mass transfer number [82]:

$$F(B_M) = (1 + B_M)^{0.7}\frac{\ln(1 + B_M)}{B_M}, \tag{3.32}$$

$$F(B_T) = (1 + B_T)^{0.7}\frac{\ln(1 + B_T)}{B_T}. \tag{3.33}$$

Finally, the corrections are made into the Sherwood and Nusselt number [82]:

$$Sh^* = 2 + \left(Sh_0 - 2\right)/F_{\mathrm{M}}, \tag{3.34}$$

$$Nu^* = 2 + \left(Nu_0 - 2\right)/F_{\mathrm{T}}. \tag{3.35}$$

That is:

$$Sh^* = 2 + \frac{(Sh_0 - 2)B_M}{(1 + B_M)^{0.7}\ln(1 + B_M)}, \tag{3.36}$$

$$Nu^* = 2 + \frac{(Nu_0 - 2)B_T}{(1 + B_T)^{0.7}\ln(1 + B_T)}. \tag{3.37}$$

The calculation of the Sherwood number and Nusselt number for non-evaporating droplet are as follows:

$$\begin{aligned} Sh_0 &= 2 + f(\mathrm{Re},\mathrm{Sc}) \\ Nu_0 &= 2 + f(\mathrm{Re},\mathrm{Pr}) \end{aligned}, \tag{3.38}$$

$$f(\mathrm{Re},\mathrm{Sc}) = \begin{cases} (1+\mathrm{ReSc})^{1/3} - 1 & \mathrm{Re} < 1 \\ (1+\mathrm{ReSc})^{1/3}\,\mathrm{Re}^{0.077} - 1 & \mathrm{Re} > 1 \end{cases}, \tag{3.39}$$

$$f(\mathrm{Re},\mathrm{Pr}) = \begin{cases} (1+\mathrm{RePr})^{1/3} - 1 & \mathrm{Re} < 1 \\ (1+\mathrm{RePr})^{1/3}\,\mathrm{Re}^{0.077} - 1 & \mathrm{Re} > 1 \end{cases}. \tag{3.40}$$

It should be noted that when the convection is absent, the Sherwood and Nusselt number reduce to 2, that is $Sh^*=Nu^*=2$.

3.3.2 The non-ideal vapor-liquid equilibrium (VLE)

In this work, the non-ideal VLE is evaluated by the γ-φ approach. That is, the non-ideal behavior in the liquid phase is presented by the activity coefficient γ_i and the Poynting factor Ψ_i, whereas the non-ideal vapor phase is denoted by the fugacity coefficient φ_i. With the above correction, the VLE of component *i* at the interface results [136],

$$X_{i,vs}\hat{\varphi}_{i,vs}\,p = \gamma_i \hat{\varphi}_{i,sat} X_{i,ls}\,p_{i,\mathrm{sat}} \exp\left(\int_{p_{i,\mathrm{sat}}}^{p} \frac{V_{i,sat}}{R_g T}\,dp \right), \tag{3.41}$$

where γ_i is the activity coefficient calculated in the liquid phase. The last term on the right side of the above equation is the Poynting factor. $\hat{\varphi}_{i,sat}$ and $\hat{\varphi}_{i,vs}$ are the fugacity coefficient at the condition of vapor state and saturated vapor state, respectively.

The fugacity coefficients $\hat{\varphi}_{i,sat}$ and $\hat{\varphi}_{i,vs}$ are evaluated from the Virial equation stated as [136],

$$\hat{\varphi}_{i,vs} = \exp\left(\frac{p}{R_g T} \left(2\sum_j B_{ij} X_{Vj} - B_{M,V} \right) \right), \tag{3.42}$$

$$\hat{\varphi}_{i,\mathrm{sat}} = \exp\left(\frac{B_{ii}}{R_g T}\,p_{i,sat} \right). \tag{3.43}$$

The index *i* and *j* indicate the different species in the mixture. B_{ii} and B_{ij} stands for two different types of Virial coefficients. In principle, B_{ii} (or B_{jj}) is used for the calculation of pure species. By contrast B_{ij} (or B_{ji}) is a cross-section coefficient and denotes the interaction between two molecules. In this context, the $B_{M,V}$ is a parameter that links the pure and cross coefficients mentioned previously. Those terms are provided as [136],

$$B_{ii} = \frac{R_g T_{c,i}}{p_{c,i}} \left(f^{(0)}\left(T_{r,i}\right) + \omega_i f^{(1)}\left(T_{r,i}\right) \right), \tag{3.44}$$

$$B_{ii} = \frac{R_g T_{c,i}}{p_{c,i}} \left(f^{(0)}\left(T_{r,i}\right) + \omega_i f^{(1)}\left(T_{r,i}\right) + f^{(2)}\left(T_{r,i}\right) \right), \tag{3.45}$$

$$B_{ij} = 0.125\left(\sqrt[3]{B_{ii}} + \sqrt[3]{B_{jj}}\right)^3, \tag{3.46}$$

$$B_{M,V} = \sum_i \sum_j X_{Vi} X_{Vj} B_{ij}\ , \tag{3.47}$$

It should be noted that two options appear here for the estimation of B_{ii}. It is suggested that the first one is designed for the non-polar gas situation, an example here is nitrogen gas. The other one is normally adopted by polar gases, ethanol, and methanol for instance.

The Poynting factor can be calculated by,

$$\Psi_i = \exp\left(\int_{p_{i,\mathrm{sat}}}^{p} \frac{V_{i,sat}}{R_g T} dp \right) \approx \exp\left(\frac{V_{i,sat}}{R_g T} \left(p - p_{i,\mathrm{sat}} \right) \right). \tag{3.48}$$

The last one, the activity coefficient γ_i is critical for the calculation of the vapor-liquid equilibrium, which can be separated into two sections: one is the contribution of the diversity of molecules size and shape. Another one is the impact of molecular interactions among different pairs of molecules [136]. The UNIFAC method is commonly used for computing the activity coefficient γ_i, which gives [136],

$$\ln \gamma_i = \ln \gamma_i^C + \ln \gamma_i^R \tag{3.49}$$

As indicated, its value is regarded as the combination of two separated and independent parts, i.e., the combinatorial section $\ln^{\gamma_i{}^C}$ and the residual section $\ln^{\gamma_i{}^R}$, which denotes the influence of each molecule and interactions among different

molecules, respectively. The combinatorial section $\ln \gamma_i^C$ is calculated as:

$$\ln \gamma_i^C = \ln \frac{\psi_i}{X_{i,1}} + 5q_i \ln \frac{\vartheta_i}{\psi_i} + l_i - \frac{\psi_i}{X_{i,1}} \sum_{j=1}^{N} X_{j,1} l_j \,, \tag{3.50}$$

with

$$l_j = 5(r_i - q_i) - (r_i - 1),\ \vartheta_i = \frac{q_i X_{i,1}}{\sum_{j=1}^{N} q_j X_{j,1}},\ \psi_i = \frac{r_i X_{i,1}}{\sum_{j=1}^{N} r_j X_{j,1}}, \tag{3.51}$$

where $X_{i,l}$ is the molar fraction of component *i*. *N* is the component number, r_i and q_i is the relative Van-der-Waals volume and surface area:

$$r_i = \sum_{k=1}^{M} v_k^{(i)} R_k,\ q_i = \sum_{k=1}^{M} v_k^{(i)} Q_k \,, \tag{3.52}$$

with $v_k^{(i)}$ stands for the number of k-type structural groups in component *i*, *M* is the group number. R_k and Q_k is the volume and surface area of each group.

The residual section $\ln \gamma_i^R$ is evaluated by:

$$\ln \gamma_i^R = \sum_{k=1}^{M} v_k^{(i)} \left[\ln \Gamma_k - \Gamma_k^{(i)} \right], \tag{3.53}$$

with Γ_k and $\Gamma_k^{(i)}$ is the active coefficient of group *k* in the mixture and pure liquid, respectively.

$$\ln \Gamma_k = Q_k \left[1 - \ln \left(\sum_{m=1}^{M} \vartheta_m \chi_{mk} \right) - \sum_{m=1}^{M} \frac{\vartheta_m \chi_{km}}{\sum_{n=1}^{M} \vartheta_n \chi_{nm}} \right], \tag{3.54}$$

where

$$\vartheta_m = \frac{Q_m X_m}{\sum_{n=1}^{M} X_n},\ X_m = \frac{\sum_{j=1}^{N} v_m^{(j)} X_{j,1}}{\sum_{j=1}^{M} \sum_{n=1}^{M} v_n^{(j)} X_{j,1}},\ \chi_{nm} = e^{-a_{nm}/T}, \tag{3.55}$$

with a_{nm} is the interaction parameters between group *n* and group *m*.

3.3.3 The separation factor

In the multicomponent system, individual components normally have different evaporation behaviors. Every component in the mixture has a preferential evaporation stage. To present the order evaporation, the separation factor is used to interpret the relative volatility between two species [99]:

$$\alpha_{ij} = \frac{K_i}{K_j}, \tag{3.56}$$

where K_i and K_j are the equilibrium constant of species i and j, which are presented as:

$$K_i = \frac{X_{i,vs}}{X_{i,ls}} = \frac{\gamma_i \hat{\varphi}_{i,\mathrm{sat}} p_{i,\mathrm{sat}} \Psi_i}{\hat{\varphi}_{i,vs} p}. \tag{3.57}$$

Substitute it into the above equation, the separation factor has the following form,

$$\alpha_{ij} = \frac{K_i}{K_j} = \frac{X_{i,vs} X_{j,ls}}{X_{i,ls} X_{j,vs}} = \frac{\gamma_i p_{i,\mathrm{sat}}}{\gamma_j p_{j,\mathrm{sat}}} \frac{\Psi_i}{\Psi_j} \frac{\hat{\varphi}_{j,vs} \hat{\varphi}_{\mathrm{i,sat}}}{\hat{\varphi}_{i,vs} \hat{\varphi}_{j,\mathrm{sat}}} = f(T, X_l, p). \tag{3.58}$$

It should be noted that for the ideal case, the correction factor of γ, Ψ and φ are equal to 1, then the former equation reduces to the ratio of vapor pressure,

$$\alpha_{ij} = \frac{K_i}{K_j} = \frac{X_{i,vs} X_{j,ls}}{X_{i,ls} X_{j,vs}} = \frac{p_{i,\mathrm{sat}}}{p_{j,\mathrm{sat}}} = f(T). \tag{3.59}$$

By definition, $\alpha_{ij}>1$ denotes that species i vaporizes faster than species j, and vice versa. The separation factor is paramount for analyzing the non-ideal evaporation behavior because it relies on temperature, pressure, and liquid phase composition for non-ideal cases. While it only depends on the temperature for ideal equilibrium.

3.3.4 Influence of droplet spacing

For a free-falling droplet stream, the distance between droplets is small, which would induce droplet interactions [137]. There are some empirical correlations available for evaporating and combusting droplet streams provided by Atthasit et al. [138] and Virepinte et al. [139]. In addition, Castanet et al. [137] investigated the heating and evaporation of mono-sized droplets in a single row under high ambient temperature conditions. It indicated that droplet spacing has a strong impact on the reduction of the Nusselt and Sherwood numbers. A new correlation had been proposed to represent the effect of the droplet spacing with the help of the experimental results.

Recently, the effect of interactions between droplets in the stream had also been quantified by Li et al. [32] with the phase rainbow refractometry and high-speed shadowgraph. A refined regression curve had been suggested to relate the evaporation rate to the spacing parameter. The evaporation rate ratios of the droplet stream and the isolated droplets at different spacing parameters C is defined as follows [32]:

$$\eta(C) = \frac{k_{\mathrm{e}}}{k_{\mathrm{iso,model}}} = 1 - A_1\left[1 + \frac{\exp(-A_2 \times (C - A_4)) - \exp(A_3 \times (C - A_4))}{\exp(-A_2 \times (C - A_4)) + \exp(A_3 \times (C - A_4))}\right] \quad (3.60)$$

with A_1=0.431, A_2=0.179, A_3=0.5, and A_4=5.076. C is the dimensionless spacing parameter $C=\left(\pi D^2 V_{\mathrm{drop}}\right)/(6Q)$. Accordingly, the influence of droplet interactions between droplets is considered by incorporating the dimensionless ratio into the simulation model.

3.3.5 Calculation of the physical properties

The physical properties of the vapor-gas mixture are evaluated based on the '1/3 rule' [140], which calculates all the parameters at the reference state:

$$\Omega_{\mathrm{ref}} = \Omega_{\mathrm{s}} + (\Omega_{\infty} - \Omega_{\mathrm{s}})/3 \quad (3.61)$$

$$\Phi_{\mathrm{g}} = Y_{a,\mathrm{ref}}(\Phi_a|_{at,T_{\mathrm{ref}}}) + Y_{\mathrm{v,ref}}(\Phi_{\mathrm{v}}|_{at,T_{\mathrm{ref}}}), \quad (3.62)$$

where Ω is temperature and Y mass fraction in the gas phase, Φ stands for the dynamic viscosity μ, specific heat at constant pressure c_p, heat conductivity k. subscript a and v represent air and vapor, respectively. For multi-component droplet, the calculation of dynamic viscosity μ, specific heat at constant pressure c_p, heat conductivity k can be evaluated by:

$$c_{p,\mathrm{g}} = \sum_i (Y_{i,\mathrm{ref}} c_{p,\mathrm{v}i}) + (1 - \sum_i Y_{i,\mathrm{ref}}) c_{p,a}. \quad (3.63)$$

The density of multicomponent mixture is:

$$\rho_{\mathrm{g}} = [\sum (Y_{i,\mathrm{ref}} / \rho_{i,\mathrm{v}}) + (1 - \sum_i Y_{\mathrm{i,ref}}) / \rho_a]^{-1}. \quad (3.64)$$

The diffusion coefficient of the mixture is based on Blanc Law [141]

$$D_{\mathrm{g}} = [\sum (X_{i,\mathrm{v}} / D_{i,\mathrm{v}})]^{-1}, \quad (3.65)$$

with $X_{i,\mathrm{v}}$ and $D_{i,\mathrm{v}}$ are the molar fraction in the gas phase and diffusion coefficient.

3.4 Model solution and validation

3.4.1 Numerical solution procedure

The evaporation model is established with MATLAB. **Figure 3.2** displays the flow chart of the solution procedure. It is mainly composed of five sections including boundary conditions, initial conditions, the equilibrium between gas and liquid phase, gas phase, and liquid phase. The governing equations of energy and species of the liquid phase are solved by the implicit finite difference discretization method. The liquid phase properties like density, specific heat capacity, viscosity, thermal conductivity, etc. have been updated at each time step based on the average composition of the mixture droplet at the previous time step. The changing droplet radius and temperature are calculated iteratively as follows.

1) First, input the boundary conditions of environment temperature and pressure;
2) Set the initial diameter, temperature, and composition of species in the liquid phase;
3) Calculate the molar fraction and mass fraction in the gas phase through the vapor-liquid equilibrium;
4) Evaluating the mass fraction and temperature of the boundary layer by 1/3 rule, and then obtain average physical parameters. In addition, solving gas-phase heat and mass transfer, obtaining dimensionless parameters as Nusselt number, Sherwood number, Spalding mass transfer number, and evaporation rate $\dot{m}_d$. Calculate Spalding heat transfer number iteratively.
5) According to the liquid phase heat and mass transfer model, calculate liquid-phase absorption heat, droplet temperature, and concentration distribution.

$$Q_L = \dot{m}_d \left\{ \frac{c_{p,v}(T_\infty - T_s)}{B_T} - \frac{\sum \dot{m}_i L_i}{\dot{m}_d} \right\} \tag{3.66}$$

$$\frac{dr_s}{dt} = \frac{\dot{m}_d}{4\pi\rho_l r_s^2} + \frac{r_s^{old}}{\Delta t}\left[\left(\frac{\rho_l^{old}}{\rho_l} \right)^{1/3} - 1 \right] \tag{3.67}$$

with r_s^{old} and ρ_l^{old} are the droplet radius and liquid density at the previous time step.

6) Regard the values obtained in step 5 as the initial conditions at the next time step. Repeat steps 1-5 until $r<0.1\times r_0$.

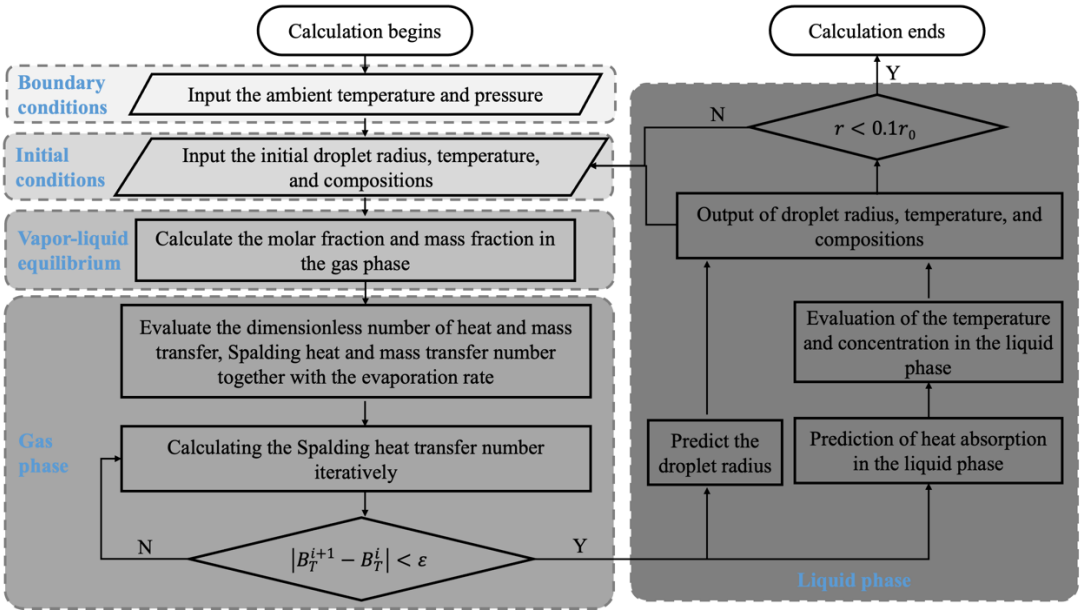

Figure 3.2 The flow chart of the calculation procedure.

3.4.2 Model validation the experimental data

Model validation is paramount for the simulation process before conducting the prediction trial. In this section, the accuracy of the established model is verified with the experimental results available in the literature. Firstly, the experimental research of diesel, ABE, and 20% ABE compound diesel (ABE 20 vol.%, diesel 80 vol.%, also ABE20) conducted in [22] provides a benchmark for multi-component model validation. The experimental data of ABE diesel blends under atmospheric pressure at 523 K and 723 K ambient conditions in reference [22] are selected to perform the validation of the multi-component droplet evaporation model. The initial droplet temperature is taken as 300 K with a diameter of 0.89 and 0.92 mm, respectively.

Figure 3.3 compares the variation of normalized squared droplet diameter (d^2/d_0^2) of numerical and experimental results. It is observed that the numerical results show a reasonable agreement with experimental results for diesel and ABE droplets. The maximum differences between the two groups of curves are less than 7.8%. For the cases of ABE20 droplets, the experiment curve displays obvious fluctuations during evaporation which represents the phenomenon of bubbles formation, droplet distortion, and partial rupture, as shown in **Figure 3.3**c. The numerical results of the ABE20 droplet can not express the fluctuation phase observed in the experiment, but the numerical

results can explain the occurrence mechanism of the fluctuation by comparing droplet temperature and component boiling temperature, which has been analyzed in the previous study [142]. Except for the fluctuation evaporation process, the variation tendency of droplet diameter between numerical and experimental results matches well.

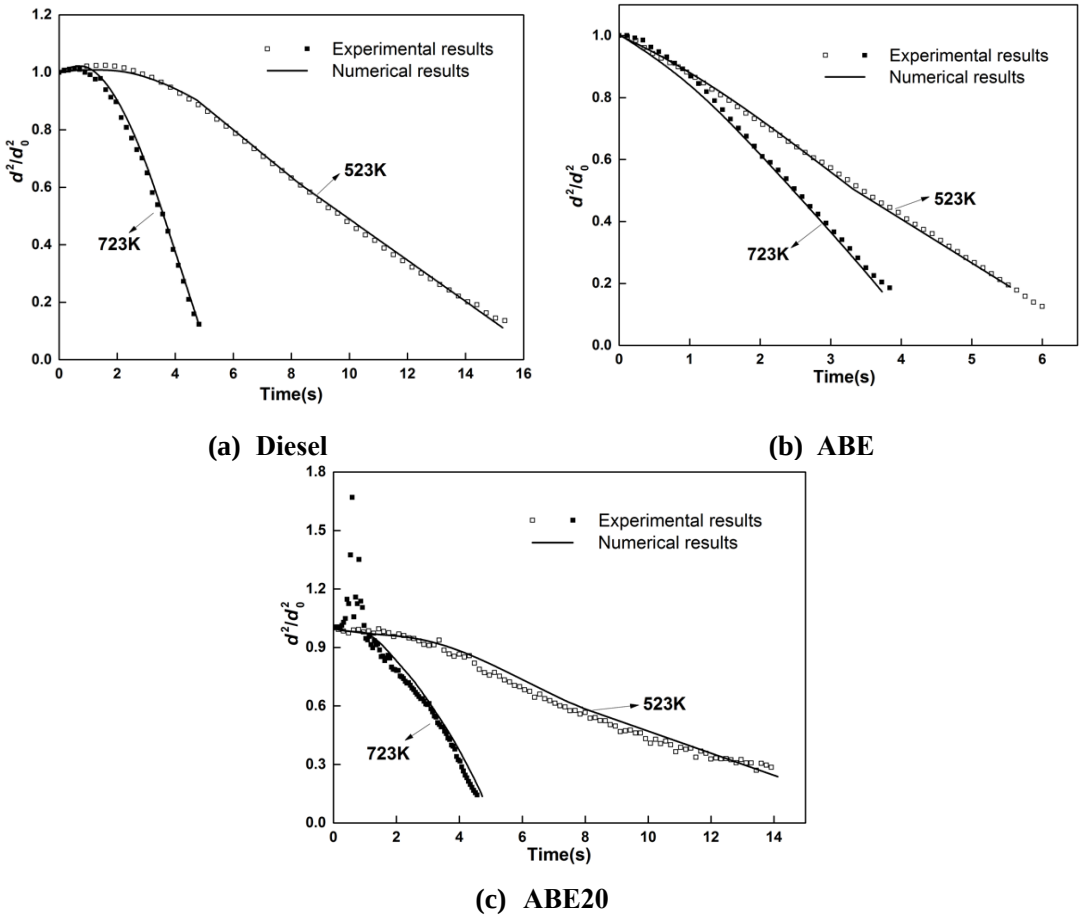

Figure 3.3 Variation of normalized droplet diameter of numerical and experimental results [142].

The accuracy of the model is also checked by another group of experimental data from Borodulin et al. [143]. They captured both the diameter and temperature information by using high-speed microphotography and infrared thermography. The same evaporation cases of ethanol/water droplets with the initial ethanol mass fraction of 25%, 50%, and 75% (denoted as E25, E50, and E75 hereafter) were simulated in this study. The initial droplet diameter and ambient temperature were taken as 2.125 mm and 24°C, respectively. The results are compared in **Figure 3.4**. It is indicated that the droplet lifetime evaluated by the model tends to be longer than that obtained in the experiment. This is perhaps attributed to the influence of the thread adopted in the

experiment, which introduces additional conduction heat transfer into the droplet and accelerates the evaporation rate [14]. Besides, the model cannot predict the sharp increase of droplet temperature at the final evaporation stage observed in the experiment. This is restricted by the peculiarity of the present pure diffusion evaporation model [144]. The predicted droplet temperature keeps constant after arriving at the adiabatic evaporation temperature of the water. Despite those discrepancies, the simulation results show a good agreement with the experiment in presenting the tendency of diameter and temperature.

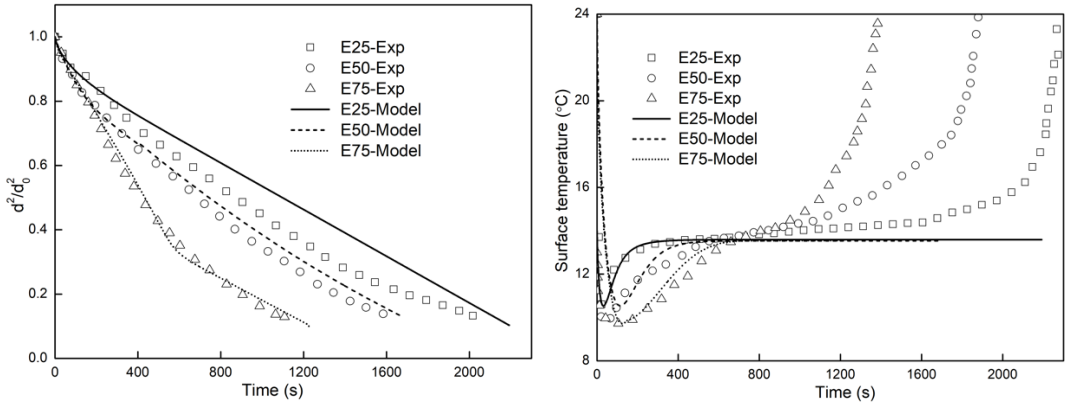

(a) The squared normalized diameter **(b) Variation of surface temperature**

Figure 3.4 Comparison of the normalized squared diameter and surface temperature for three kinds of water/ethanol droplets and the validation with the experimental data in [143].

3.4.3 Validation with the simulation results

The numerical validation is made by mimicking the same evaporation process of ethanol/iso-octane fuel droplets simulated by Al-Esawi et al. [145]. The initial droplet radius and the temperature were taken as 12 μm and 296 K, respectively. The relative velocity between the droplet and ambient flow was 24 m/s. The ambient pressure and temperature were 9 bar and 545 K, respectively. The term EM5 and EM85 denote that the ethanol volume fraction in the mixture is 5% and 85%. **Figure 3.5** compares the simulation results obtained in this work and the reference data. The results indicate that the variation of droplet radius and surface temperature obtained by those two models show good agreement both for EM5 and EM85 droplets. The small deviation that appeared in those curves can be attributed to the difference in calculating the physical parameters.

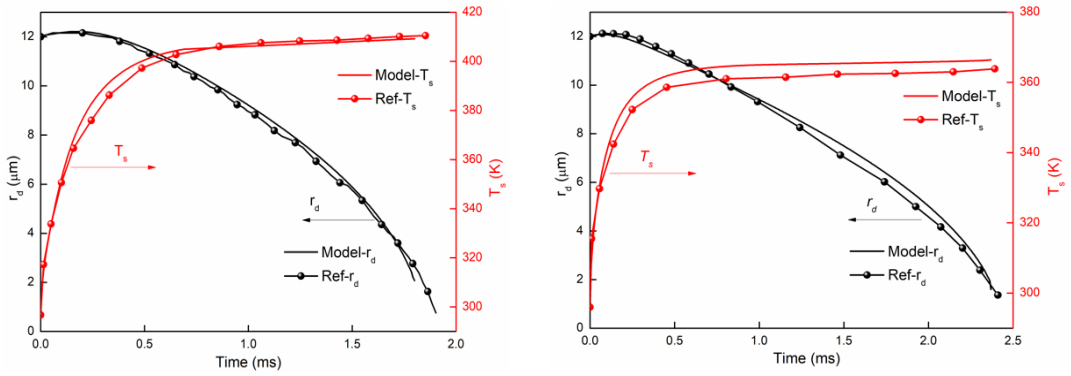

(a) EM5 **(b) EM85**

Figure 3.5 Temporal variation of droplet surface temperature and droplet radius evaluated by this work and the numerical results obtained by Al-Esawi et al. [145] for (a) EM5 and (b) EM85.

In addition, the ability of the established model in presenting the impact of ambient vapor concentration is validated with the results of Gavhane et al. [131]. Reference [131] reported the coupling influence of fuel properties in the liquid phase and fuel vapor concentration in the gas phase on the droplet evaporation process in normal pressure and high-temperature condition by simulating the bi-component fuel droplet with different volatility. The temperature was 750 K and 1500 K, respectively. The carrier phase was regarded as a mixture of air and fuel vapor at a non-convection state. In the present work, the comparison is made at the condition of the ambient temperature of 750 K and ambient pressure of 1 bar. The initial droplet diameter is 50 μm and 300 K, separately. The initial liquid phase is composed of 50% heptane and 50% dodecane by mass. The second component, i.e., dodecane is taken as one of the components in the gas phase and its mass fraction Y_{2g} varies in the range of 0.0-0.6.

Figure 3.6 compares the temporal variation of normalized droplet mass obtained by Gavhane et al. [131] and the simulation in this paper with various ambient fuel vapor concentrations. It is observed that at the initial period of droplet evaporation, the droplet mass exhibits an increasing tendency to a different extent when the background vapor is non-zero. This phenomenon is caused by the condensation at the droplet surface concerning the higher concentration in the free stream during the heat-up period. The fuel droplet is cold during this period and the temperature difference between the vapor and liquid phase leads to the condensation of vapor on the droplet surface. The greater

concentration of ambient vapor leads to a higher increment in diameter. Besides, in the context of ambient temperature 750 K and pressure of 1 bar, the appearance of background vapor before droplet evaporation inhibits droplet mass depletion and increases droplet lifetime. From the above aspects, the results obtained by our model show good agreement with that in reference. The small deviation between those two models occurs in the early stage of the evaporation process, and the maximum difference of mass reduction between those two models is 5.1%. This might attribute to the different equations in calculating some physical parameters such as saturated pressure and enthalpy of the vaporization. After that, both the tendency and the value are consistent with each other at the equilibrium stage.

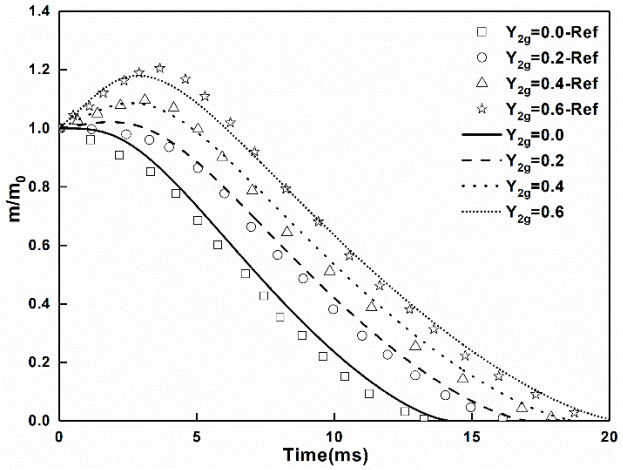

Figure 3.6 The temporal histories of normalized droplet mass with dodecane vapor in background obtained by this model for 50%heptane-50%dodecane droplet at T_∞=750 K and P_∞=1 bar compared with reference [131].

The temporal evolutions of droplet temperature with different vapor concentrations in ambient for 50%heptane-50%dodecane droplet at T_∞=750 K and P_∞=1 bar are illustrated in **Figure 3.7**. An increase in heating rate is evidenced at higher dodecane vapor concentration. It is due to the lower mass reduction rate with higher vapor concentration. This, in turn, increases the conductive energy into the liquid phase to heat the droplet. Furthermore, the steady-state temperature in the liquid phase increases evidently with more dodecane vapor in the gas phase. The increasing percentage under different fuel vapor conditions compared with the state without fuel vapor are 2.06%, 3.71%, and 8.28%, respectively. This indicates that the evaporation

of droplets needs a higher temperature to maintain enough vapor mass concentration at the droplet interface so that it can balance with the vapor concentration in the ambient field.

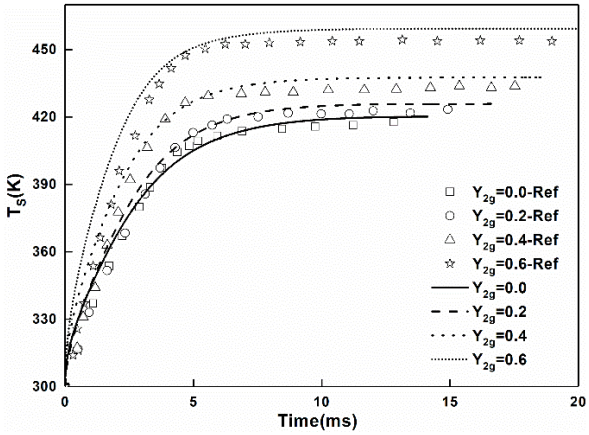

Figure 3.7 Variation of droplet temperature of with different ambient dodecane vapor concentrations for 50%heptane-50%dodecane droplet at T_∞=750 K and P_∞=1 bar and comparison with reference [131].

3.5 Summary

This chapter talks about the details of the numerical method. Starting from the physical description and assumptions, the numerical algorithm mainly contains the heat and mass transfer in the liquid phase, the mass diffusion in the gas phase, and the equilibrium between liquid and gas phases. The model is validated by experimental and simulation results in references. The concluding remarks are as follows:

1. A non-ideal vapor-liquid equilibrium model based on the effective conductivity and diffusivity model has been created. The method incorporates the impact of convection, the interactions between neighboring droplets, temperature-dependent physical parameters, and the polarity differences between different components.
2. Experimental validation of the established model is made from the aspects of diameter and temperature. The evaporation process of multi-component ABE-diesel blends (acetone-butanol-ethanol and diesel) and the binary mixture of ethanol/water droplets is simulated and compared with the literature.
3. The numerical validation is made by mimicking the same evaporation process

of ethanol/iso-octane droplets from the literature. Besides, the ability of the model in presenting the impact of ambient vapor concentration is examined by performing the evaporation process of heptane-dodecane binary droplets.

4. Characterization of mono droplet stream

The transient evaporation characteristics of free-falling ethanol and n-heptane droplets stream under ambient temperatures of 373-473 K are investigated with the rainbow technique in this chapter. By analyzing the rainbow patterns captured in the vicinity of the rainbow angle, the droplet size and the equivalent temperature of the droplet have been simultaneously extracted. Then, the diameter and temperature retrieved from rainbow signals are quantitatively compared with the numerical predictions to examine the differences over the test results. Finally, the temperature gradient and temperature values inside the droplet under different ambient temperature conditions are evaluated.

4.1 Typical evaporation behavior

The experimental parameters for all the cases are given in **Table 4.1**. The measurement volume spans the vertical distance of 37-44 mm and 47-54 mm away from the nozzle of the droplet generator, with an interval of 1 mm. Simulation has the same boundary and initial conditions as the experiment. The initial droplet velocity from the nozzle is about 9.5 m/s for ethanol and 6.7 m/s for heptane. As a consequence, the velocities along the measured volume of 37-54 mm away from the nozzle of the droplet generator are 9.54-9.55 m/s and 6.75-6.77 m/s due to the gravity acceleration. The distance turns into a time range of 0.0039-0.0056 s and 0.0052-0.0077 s. Three pinhole sizes of 50 μm, 75 μm, and 100 μm have been adopted to control the initial droplet diameter.

Table 4.1 Key parameters of experiment cases.

	Ethanol			Heptane		
Initial temperature (K)	293			293		
Initial velocity (m/s)	9.5			6.7		
Injection pressure (bar)	1.4			1.2		
Injection frequency (kHz)	25	27	27.15	25	26.22	28.56
Pinhole diameter (μm)	50	75	100	50	75	100
Initial diameter (μm)	123	156	188	114	147	173

Ambient temperature (K)	373	423	473	373	423	473

4.1.1 Scattering patterns and light intensity curves

Figure 4.1 and **Figure 4.2** show the typical rainbow images of ethanol and heptane droplet streams under different conditions. The images are captured nearby the primary rainbow region to ensure that the first several peaks are recorded and displayed. As indicated, the clear and stable scattering patterns of both main peaks and ripple structures are visible, which come from the interference between first internal reflections and the interference between the external reflection and internal reflection light [50]. This ensures the stability of the droplet stream. Additionally, a horizontal structure is captured as the droplets stream is illuminated by a pulsed laser with a short exposition time of 7.5 ns. This discontinuous aspect in the scattering image results from the interference between the light scattered by particles located in the control volume. It is believed that the discontinuous aspect in the scattering image relates to the information of the particle numbers as well as the relative distance between the particles in the control volume [128].

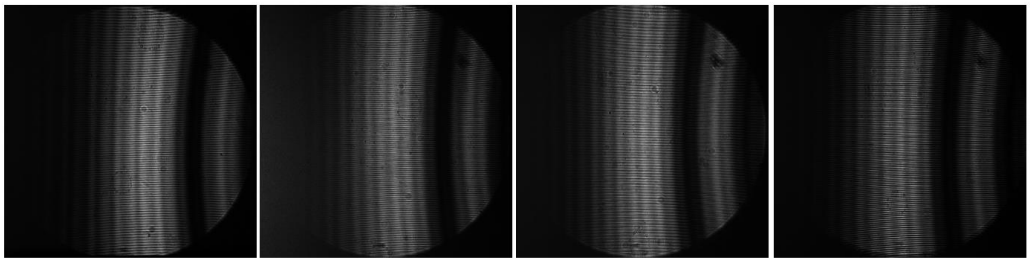

(a) Ethanol droplets generated from the pinhole size of 50 μm

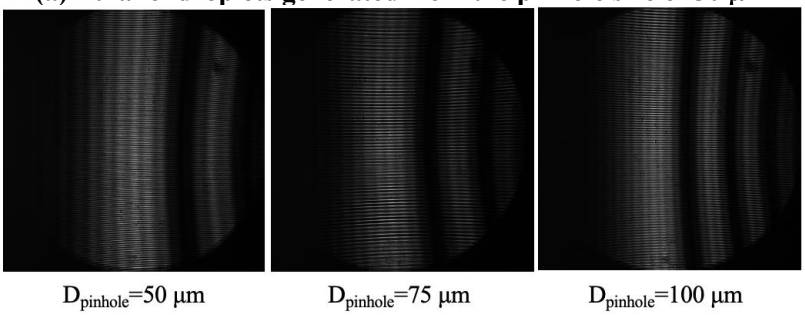

(b) Ethanol droplets under the ambient temperature of 473 K

Figure 4.1 Typical rainbow signal of ethanol droplets illuminated by a pulsed laser of different cases.

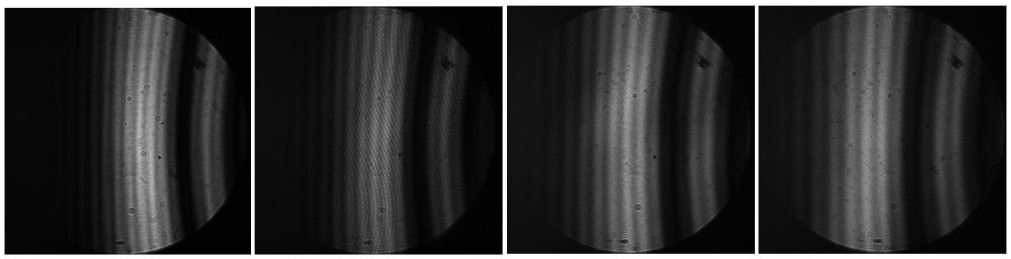

(a) Heptane droplets generated from the pinhole size of 50 μm

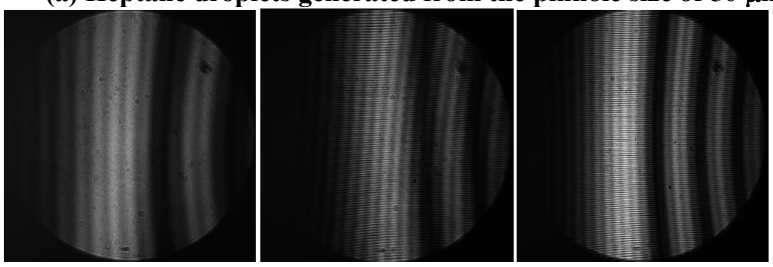

(b) Heptane droplets under the ambient temperature of 473 K

Figure 4.2 Typical rainbow signal of heptane droplets illuminated by a pulsed laser of different cases.

The normalized intensity curves averaged over 20 lines along the center of each rainbow signal are further plotted in **Figure 4.3**. Both the primary peak and Airy fringes are distinctly presented together with the ripple structures superimposing on those peaks. Apart from that, **Figure 4.3**a and **Figure 4.3**c reveal that the rainbow signal shifts to lower scattering angles by enhancing ambient temperature. This indicates a reduction of the refractive index corresponding to an increased temperature in the liquid phase. Theoretically, changing the refractive index directly shifts the geometrical rainbow position and primary rainbow position [55]. Additionally, **Figure 4.3**b and **Figure 4.3**d display the influence of particle size on the intensity curve. The droplets generated by a larger pinhole size tend to have more peaks within the same scattering angle range, which leads to a smaller angular distance between neighboring Airy peaks [55].

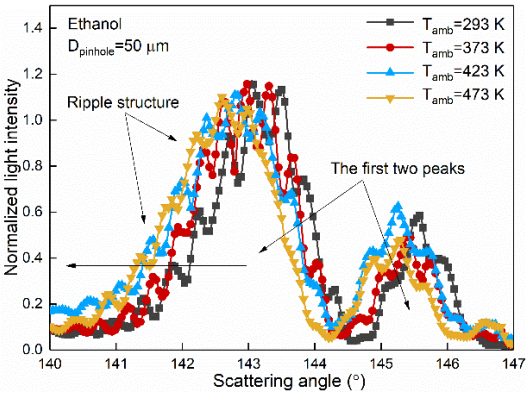

(a) $D_{pinhole}$=50 μm (ethanol droplet)

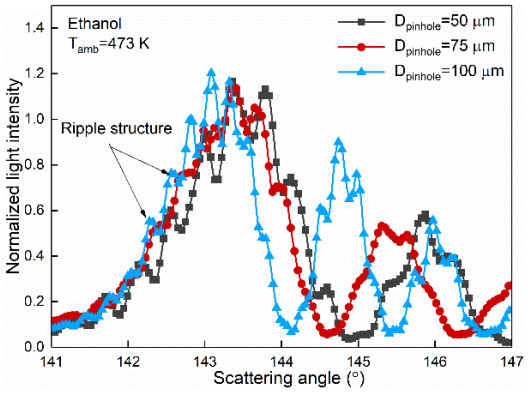

(b) T_{amb}=473 K (ethanol droplet)

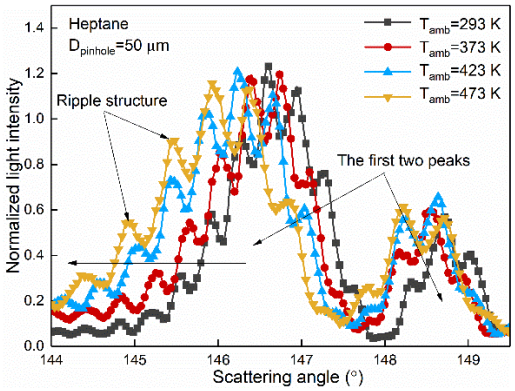

(c) $D_{pinhole}$=50 μm (heptane droplet)

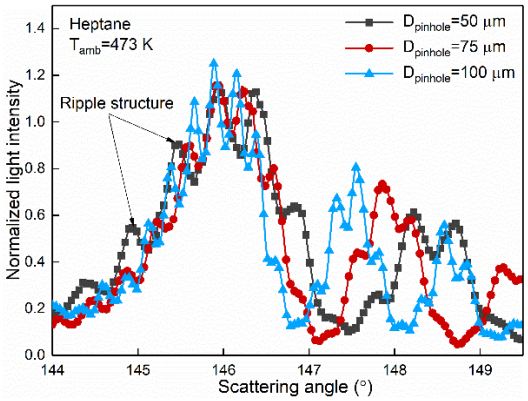

(d) T_{amb}=473 K (heptane droplet)

Figure 4.3 The normalized light intensity curves averaged over 20 lines along the center of the rainbow signals under different conditions.

4.1.2 Diameter and temperature of droplets

After the data inversion process, the droplet diameter and refractive indices under different temperature conditions are obtained and compared in **Figure 4.4**. As displayed in **Figure 4.4**a and **Figure 4.4**c, the diameters of both ethanol and heptane droplets gradually reduce with time during the present research range. A higher ambient temperature leads to smaller droplet size. Additionally, the variations of refractive index and temperature are plotted in **Figure 4.4**b and **Figure 4.4**d. The temperature is inversely proportional to the refractive index, i.e., a small refractive index means a high temperature and vice versa. The results present a heating process in droplet temperature and a linearly decreasing of refractive index with time, which holds for both ethanol and heptane droplets. Enhancing the ambient temperature gives rise to a higher temperature in the liquid phase.

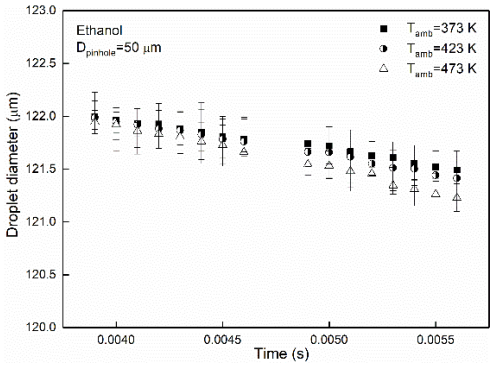

(a) Diameter of ethanol

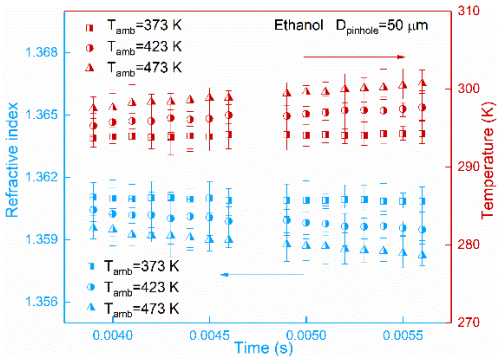

(b) Refractive indices and temperatures of ethanol

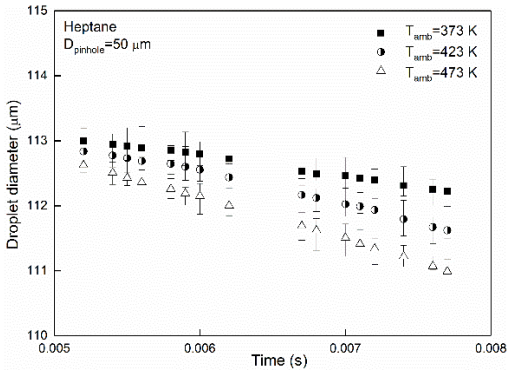

(c) Diameter of heptane

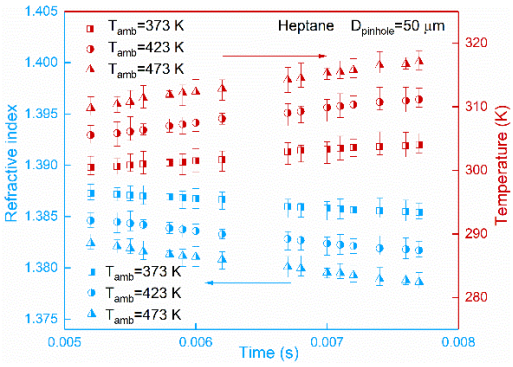

(d) Refractive indices and temperatures of heptane

Figure 4.4 Variation of the droplet diameter, refractive indices, and the corresponding temperature under different ambient temperatures.

Figure 4.5 compares the evaporation characteristics of ethanol and heptane droplets from the aspects of normalized squared diameter and temperature. The time is normalized by the squared diameter for the sake of comparison. In the first, the size change of heptane droplet is remarkably larger than that of ethanol. As quantified in **Figure 4.6**a, the reduction percentage of the normalized squared diameter for heptane droplet is greater than the value of the ethanol droplet under three ambient temperature conditions. Enhancing the ambient temperature from 373 K to 473 K, the reduction percentage of droplet size increases from 1.37 % to 2.88 % for heptane. On the other hand, the temperature of heptane droplets is higher than the one of ethanol droplets for all cases. As presented in **Figure 4.6**b, the heptane droplets have a larger increment in temperature with a maximum value of 7.27 K in contrast to the maximum value of 3.23 K for ethanol. Also, a higher ambient temperature means a larger heating rate of droplets. Taken together, those results suggest that heptane droplet is more sensitive to

environmental change. One possible explanation for this might be that the latent heat of ethanol is significantly larger than that of heptane. Therefore, the heat transferred into the liquid phase and the quantity of vaporized liquids are less for ethanol droplets under the same temperature conditions.

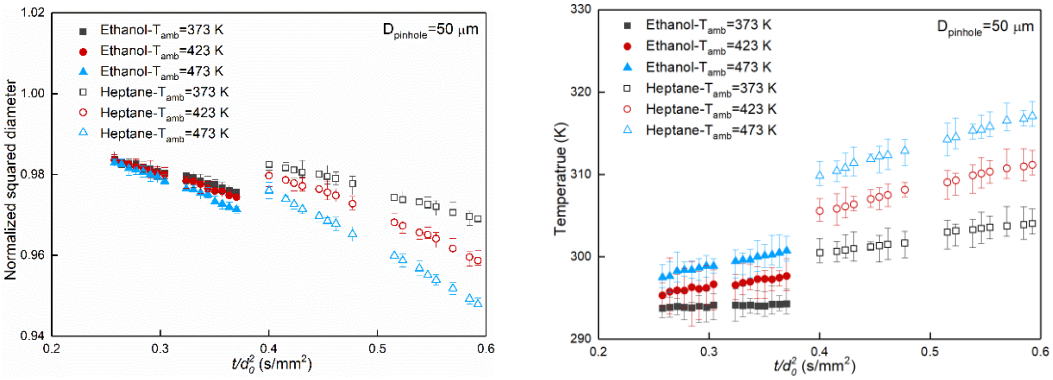

(a) Normalized diameter **(b) Droplet temperature**

Figure 4.5 Comparison of the normalized diameter and temperature values of ethanol and heptane.

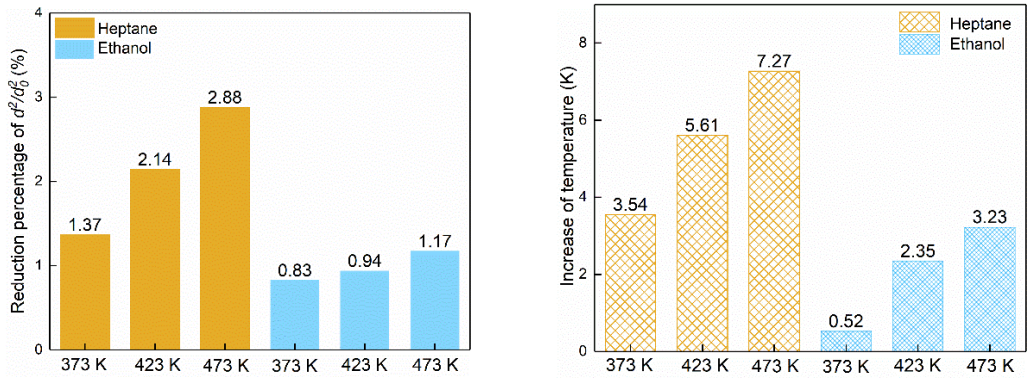

(a) Reduction percentage of normalized squared diameter **(b) Increase of droplet temperature**

Figure 4.6 The variation of droplet size and temperature of ethanol and heptane in the measurement volume.

4.2 Comparison between experimental and simulations

In this section, the measured data are compared with simulation results to ensure the accuracy of the experimental method as well as provide a further benchmark for model validation. The droplet evaporation model established in chapter 3 is adopted to do the comparison study, which takes into account the temperature-dependent physical

parameters and the effective thermal conductivity and diffusivity inside the droplet. The simulation adopted the same boundary and initial conditions as the experiment. Additionally, the theoretical spatial distributions of droplet streams generated by three different pinhole sizes are schematized in **Figure 4.7**.

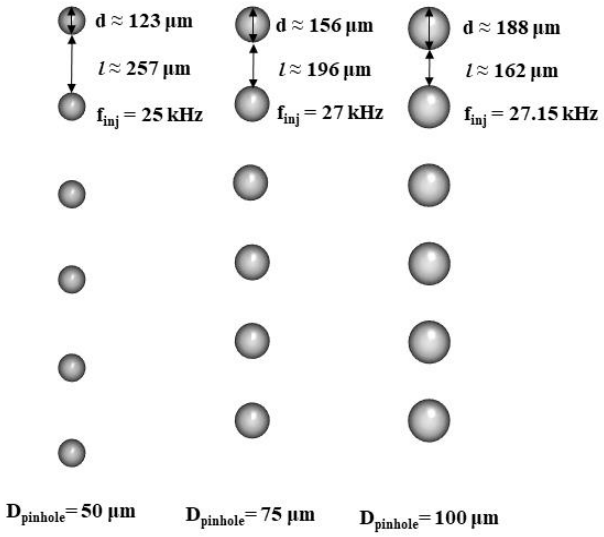

Figure 4.7 Schematic illustration of the spatial distributions of ethanol droplet stream produced by three different pinholes with the same injection pressure of 1.4 bar.

It is noticed that the distance between neighboring droplets is small under this condition, which might induce an additional impact on the evaporation process. The influence of droplet spacing on the variation of diameter and temperature has been exemplified in **Figure 4.8**. The results validate the negative effect of the neighboring droplet on the evaporation and heating rate. Larger droplet experiences more reduction as a result of smaller spacing. Therefore, the simulations of droplet evaporation have taken the spacing parameter into consideration.

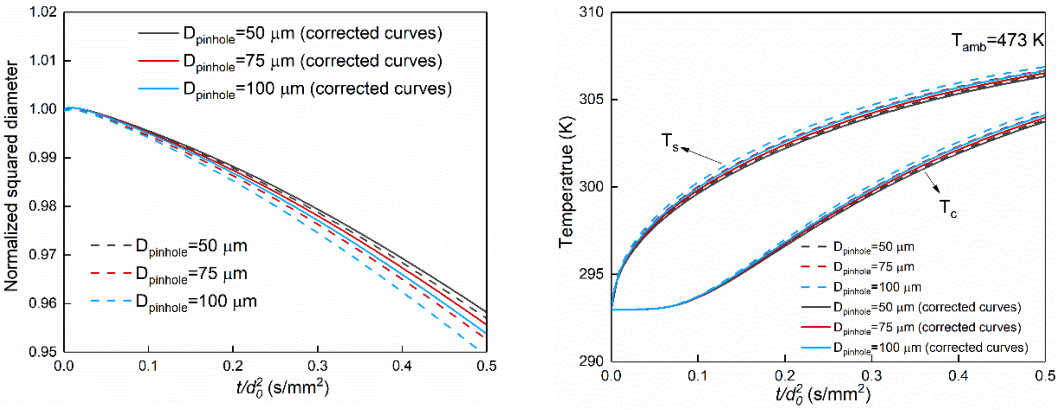

(a) Normalized squared diameter **(b) Temperature**

Figure 4.8 Corrections of the droplet interaction on the evaporation process.

4.2.1 Variation of diameter and temperature under different conditions

Following this, the temporal variation of the normalized squared diameter and temperature obtained by the experiment and simulation methods are compared in **Figure 4.9**. The investigations are performed with ethanol and heptane droplets under three ambient temperature conditions varying from 373 K to 473 K. To eliminate the influence of discrepancy of initial diameter, the results are presented in a normalized manner. As indicated, for the present research range, the variation trend of normalized squared diameter confirms well with the simulation results. Heptane droplet has a non-near reduction trend in the normalized diameter especially under the condition of 473 K. This can be attributed to the impact of thermal expansion during this transient stage. **Figure 4.9**b and **Figure 4.9**d display the temperature variations of ethanol and heptane droplets, respectively. Noting that the uncertainty of the temperature measurement is less than 5 K, which consents well with the literature [146]. Firstly, for simulation, the temperatures at the droplet surface are always higher than the ones at the droplet center since it is more sensitive to the change in the gas phase. Besides, both the numerical and experimental results exhibit an increasing tendency of temperature. Furthermore, the measured droplet temperatures are neither identical to the predicted temperature at the droplet surface nor to that at the droplet center. It is observed that the measured temperatures locate at outside of the predicted values with a more approximation to the temperature at the droplet center. These differences can be explained by the temperature gradient in the liquid phase.

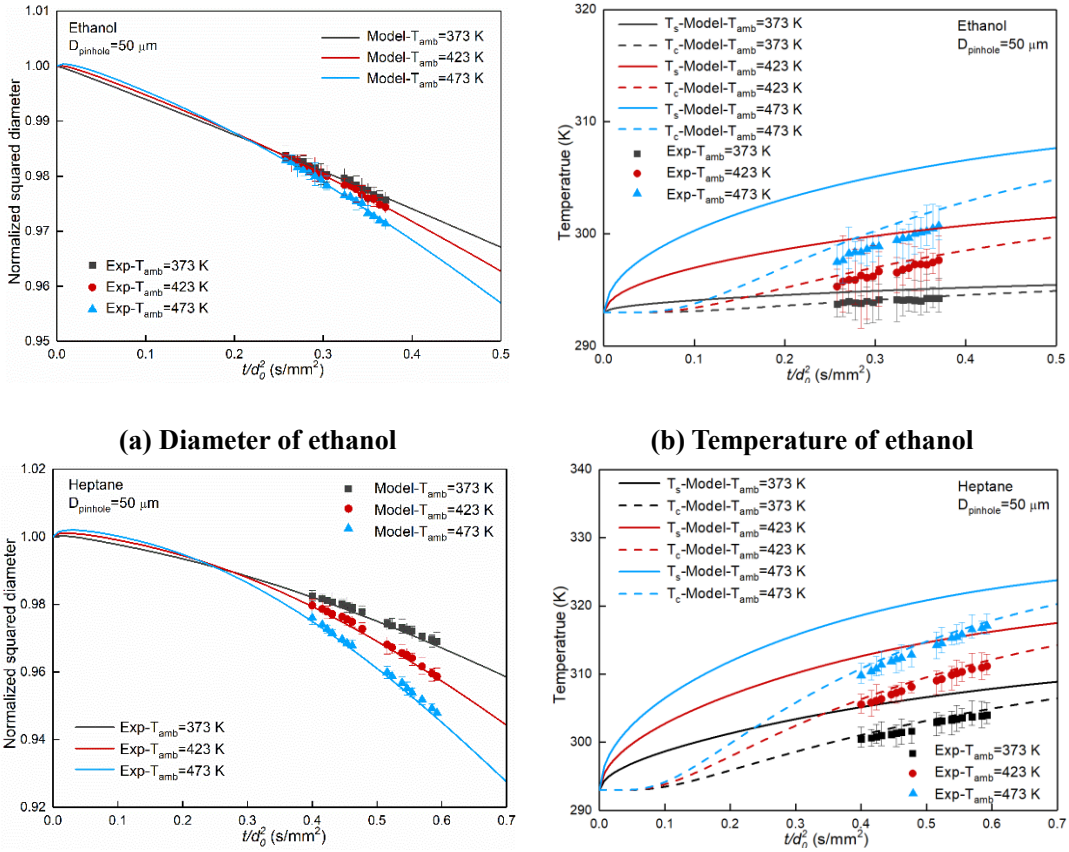

(a) Diameter of ethanol **(b) Temperature of ethanol**

(c) Diameter of heptane **(d) Temperature of heptane**

Figure 4.9 Variation of the droplet diameter and temperatures under different ambient conditions by experiment and model for the $D_{pinhole}$=50 μm.

Figure 4.10 presents the experimental measurements and simulation results of ethanol and heptane droplets with different initial diameters under the ambient temperature of 473 K. Firstly, the variations of droplet size show good agreement between experiment and model. It indicates that the evaporation rate slows down with the increase of the initial droplet size as displayed in **Figure 4.11**a. Also, heptane droplets experience more suppression than ethanol droplets regarding the reduction rate of normalized diameter. Apart from the droplet size, the temperature variations of ethanol and heptane droplets are plotted in **Figure 4.10**b and **Figure 4.10**d, respectively. For smaller droplets generated with a pinhole size of 50 μm, the equivalent temperatures from the experiment are lower than the simulation values. When the droplet streams have a relatively larger size, the measured temperatures locate between the simulated ones at the droplet surface and center. It is also noticed that the measured temperature of the heptane droplet approximates the predicted temperature at the droplet center.

Likewise, the differences in the temperatures can be attributed to the impact of the temperature gradient. Furthermore, the negative impact of increasing the initial droplet diameter on the heating process is confirmed in **Figure 4.11**b. The increment of droplet temperature reduces from 7.27 K to 4.78 K for heptane droplets and 3.23 K to 2.13 K for ethanol droplets by changing the pinhole size from 50 μm to 100 μm.

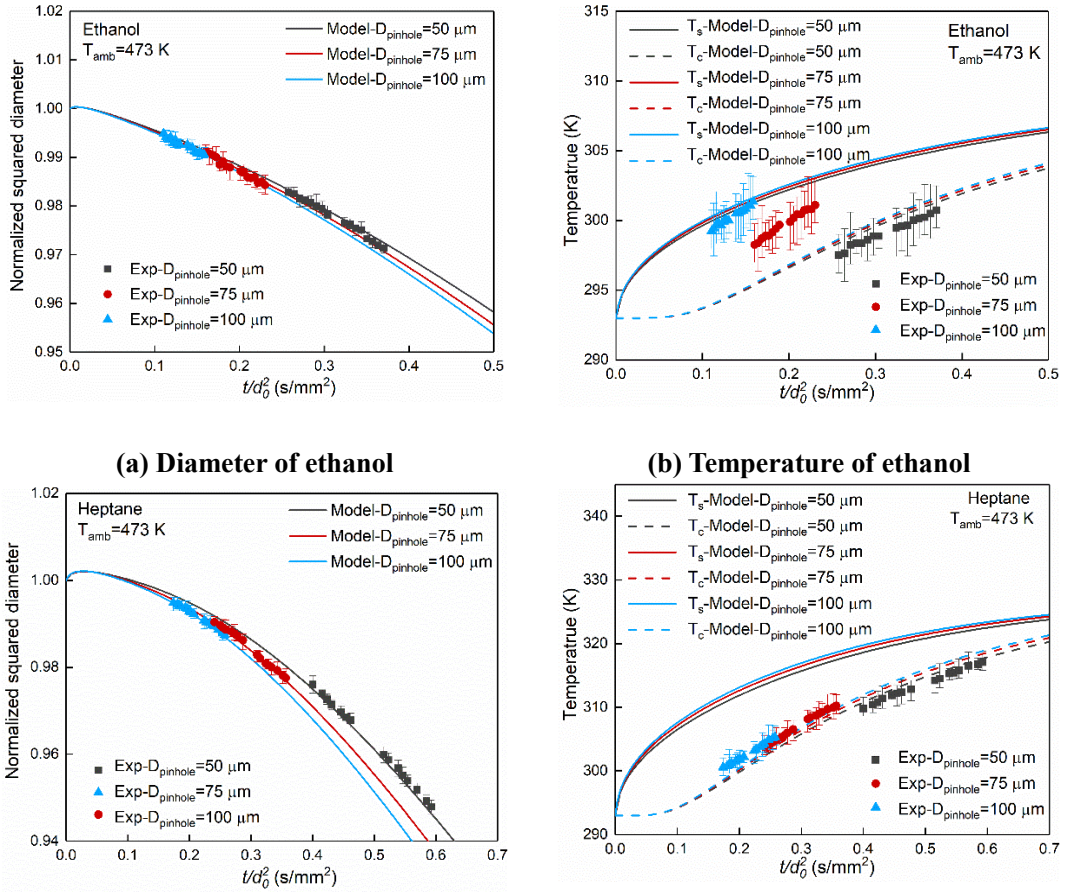

(a) Diameter of ethanol **(b) Temperature of ethanol**

(c) Diameter of heptane **(d) Temperature of heptane**

Figure 4.10 Evolutions of the normalized squared diameter and temperatures of ethanol and heptane droplets under T_{amb}=473 K.

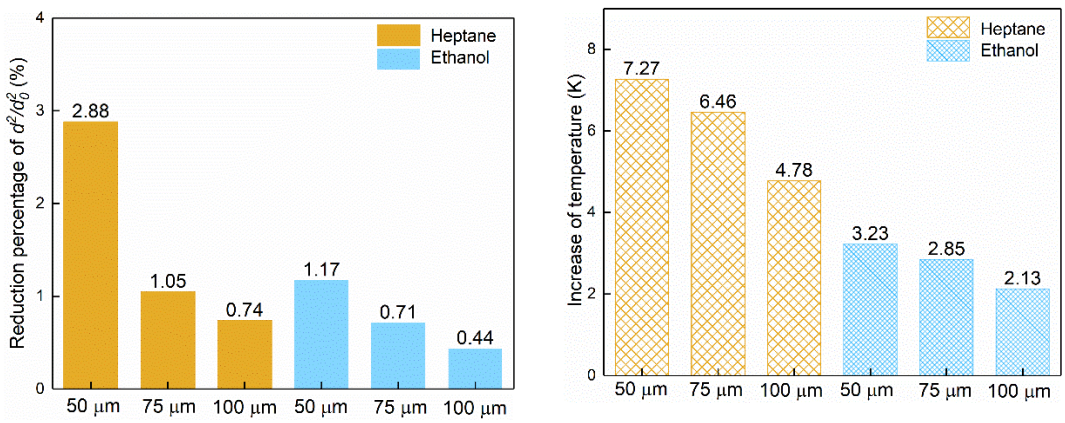

(a) Reduction percentage of normalized squared diameter **(b) Increase of droplet temperature**

Figure 4.11 Comparison of the reduction rate of droplet size and heating rate of ethanol and heptane droplets with different initial sizes.

4.2.2 Analysis of the refractive index gradient

As stated before, the gradient of the refractive index is taken as a polynomial form that depends solely on radial location to account for the influence of the refractive index gradient inside the droplet. The refractive index curves from models are compared with the refractive index profiles resulting from different polynomial orders to select the optimum polynomial orders. **Figure 4.12**, **Figure 4.13**, and **Figure 4.14** systematically present the refractive index profiles of ethanol and heptane droplets from the aspects of different instants, different temperature conditions, and different initial droplet sizes. In each plot, the refractive indices at the center and surface of the droplet are also displayed for comparison. It is found that a larger polynomial order value means a sharp gradient at the droplet surface, accordingly, the refractive index at the droplet center dominates the overall gradient profiles. The results of ethanol and heptane droplets indicate that the parabolic profiles of refractive index are most similar to the theoretical curves during the present research range no matter of the instance, ambient temperature, and initial droplet size.

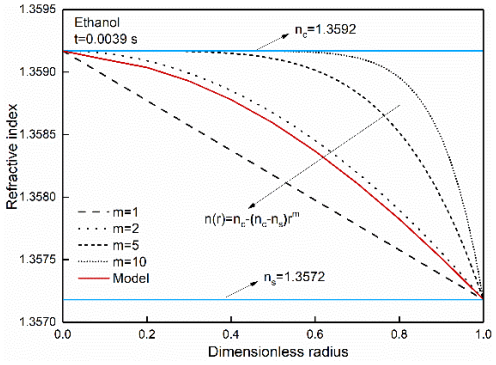

(a) t=0.0039 s (ethanol droplet)

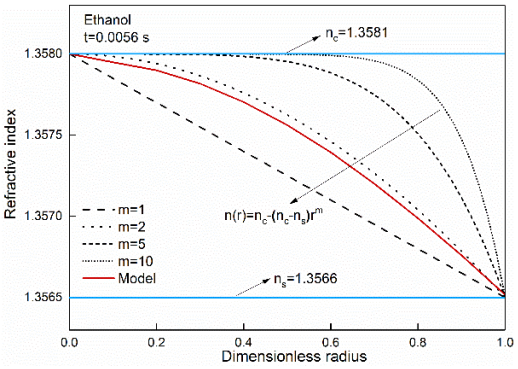

(b) t=0.0056 s (ethanol droplet)

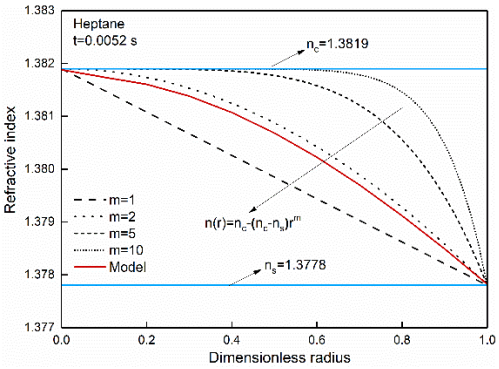

(c) t=0.0052 s (heptane droplet)

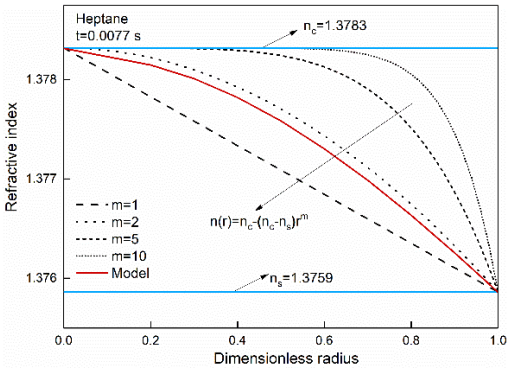

(d) 0.0077 s (heptane droplet)

Figure 4.12 The refractive index profiles of ethanol and heptane droplets at two instants (T_{amb}=473 K, $D_{pinhole}$=50 µm).

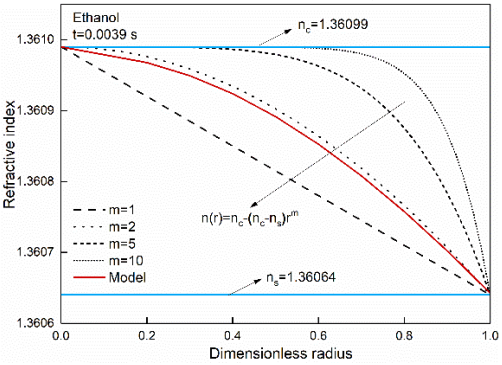

(a) t=0.0039 s (ethanol droplet)

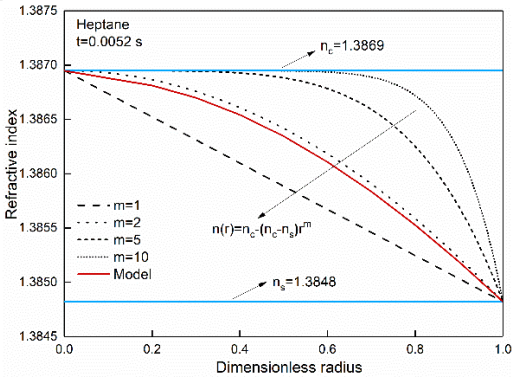

(b) t=0.0052 s (heptane droplet)

Figure 4.13 Variation of the refractive index profiles of ethanol and heptane droplets by changing the ambient temperature (T_{amb}=373 K, $D_{pinhole}$=50 µm).

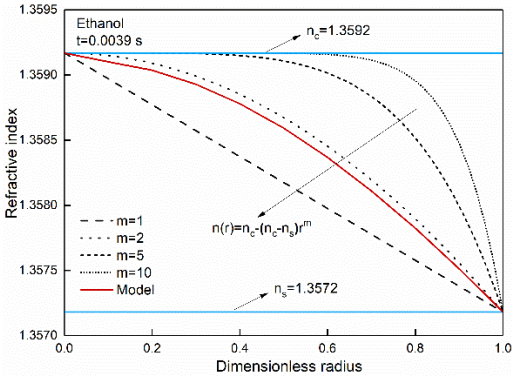

(a) $D_{pinhole}$=50 µm (ethanol droplet)

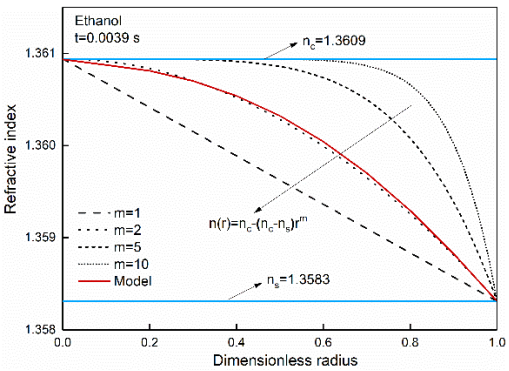

(b) $D_{pinhole}$=100 µm (ethanol droplet)

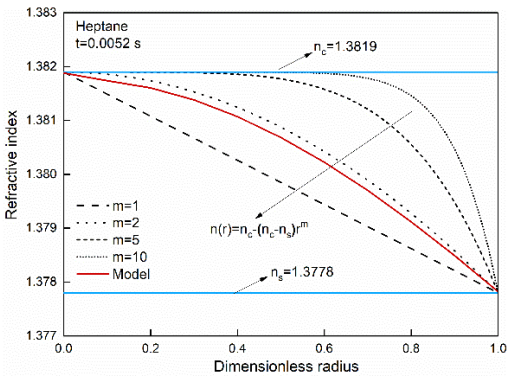

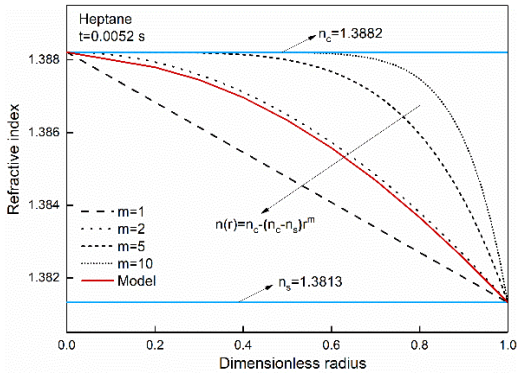

(c) $D_{pinhole}$=50 µm (heptane droplet) **(d) $D_{pinhole}$=100 µm (heptane droplet)**

Figure 4.14 The refractive index profiles of ethanol and heptane droplets with different initial sizes (T_{amb}=473 K, $D_{pinhole}$=50 µm and 100 µm).

Next, the underlying mechanism between the measured refractive index and the refractive indices at droplet surface and center is revealed by considering the impact of refractive index gradient in the liquid phase. Taking the cases under the ambient temperature of 473 K as an example, the dependence of the resulting refractive index on the polynomial order for a given refractive index at the surface and core is displayed in **Figure 4.15**. Two pinhole diameters of heptane and ethanol are chosen for comparison. The result presents a surprisingly increasing trend of the refractive index when the polynomial order is between 1 and 4. Then the refractive index decreases approaching the value of the refractive index at the droplet core for large polynomial orders. Following a parabolic order of m=2, the resulting refractive index is theoretically larger than both values in the liquid phase, therefore, producing a much lower temperature. This well explains the behavior that the temperature derived from the experiment measurement is outside of the simulated ones with a more approximation to the temperature at the droplet center.

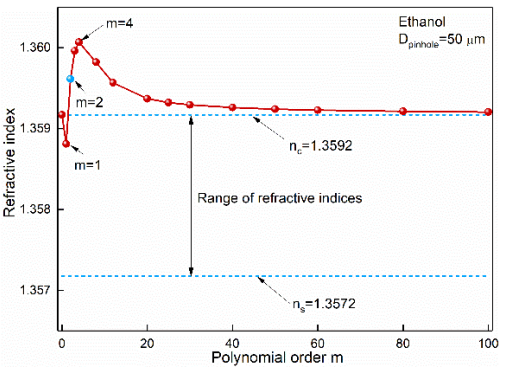

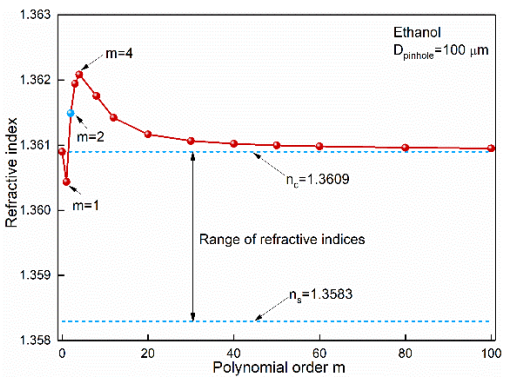

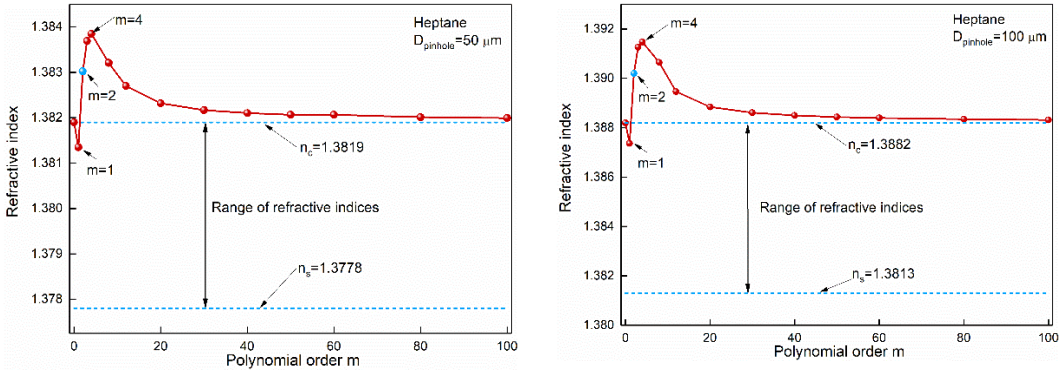

(a) $D_{pinhole}$=50 μm (ethanol droplet) **(b) $D_{pinhole}$=100 μm (ethanol droplet)**

(c) $D_{pinhole}$=50 μm (heptane droplet) **(d) $D_{pinhole}$=100 μm (heptane droplet)**

Figure 4.15 The variation of the refractive index with polynomial orders.

4.3 Temperature evaluations of inhomogeneous particles

The equivalent refractive index is the function of the refractive index profile and the indices at the droplet surface and center. Thinking it in a reverse manner, the temperature value at the droplet surface and core together with the temperature distribution can be predicted from the equivalent temperature. As we have supposed the profile inside the liquid phase with a polynomial order of 2, the dependence of the equivalent refractive index on the refractive indices at droplet surface and center is examined in **Figure 4.16**. The refractive indices at droplet surface and center vary in the range of 1.352-1.359. A surprising result is that any couple [n_c, n_s] gives rise to only one equivalent refractive index, which provides the possibility of the data inversion process. Consequently, taking n_s and n_c as fitting parameters, the optimum value of n_s and n_c as well as the refractive index distribution can be retrieved based on the least square fit method.

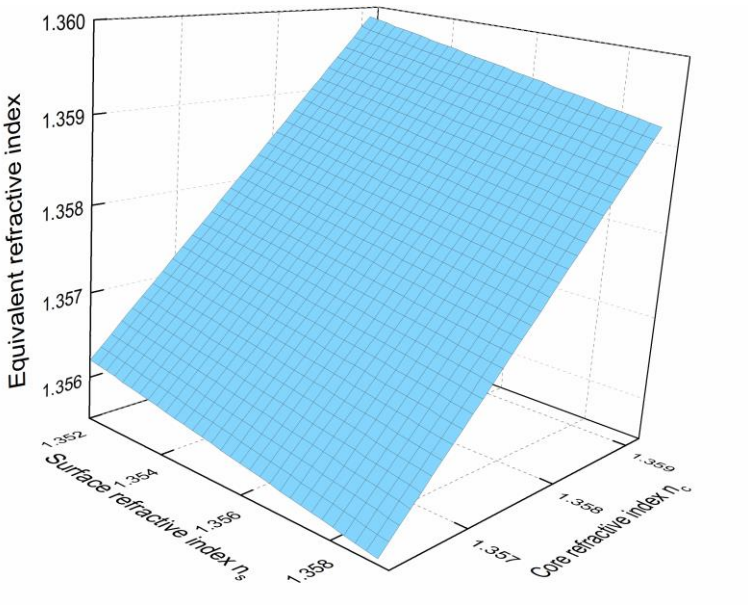

Figure 4.16 Dependence of the equivalent refractive index on the refractive indices at the droplet surface and center.

Figure 4.17 displays the temperature evolutions at the surface and center of ethanol and heptane droplets. The curves are the results of models whereas the scatters stand for experimental data. First of all, the experimental and simulated temperature values of small droplets consent with each other, as well as the evolution tendency. This is consistent for both ethanol and heptane droplets. In any case, the surface temperature from the experiment is always higher than the temperature at the droplet center, which confirms well with the simulation curves. Secondly, the deviation of the temperatures between experimental measurements and the predictions is visible when the droplet size is large, especially for ethanol droplets. It indicates that the temperature differences between experiments and simulations increase with the droplet size. This can be attributed to the shape change of larger droplets from spherical to spheroidal ones.

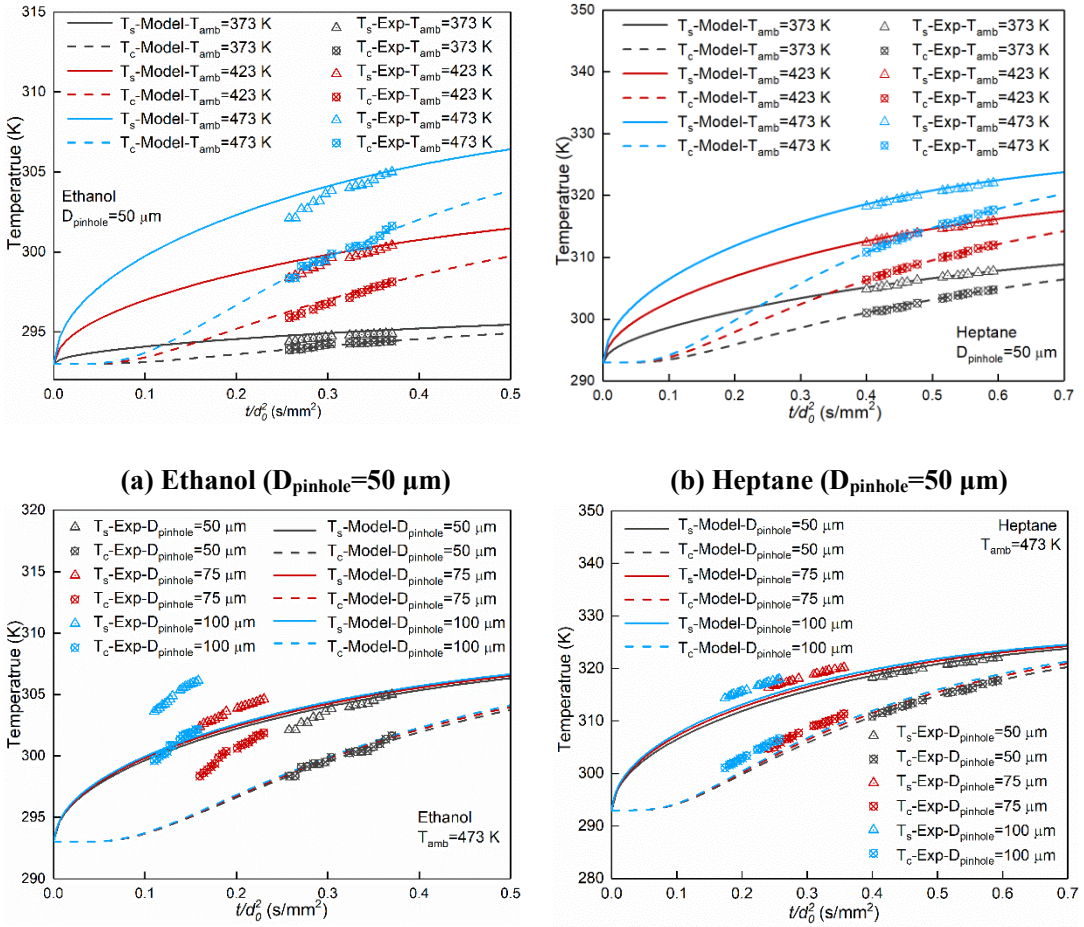

(a) Ethanol ($D_{pinhole}$=50 μm) **(b) Heptane ($D_{pinhole}$=50 μm)**

(c) Ethanol (T_{amb}=473 K) **(d) Heptane (T_{amb}=473 K)**

Figure 4.17 Comparison of the temperature evolutions between experiment and model.

The impact of shape change on the scattering angle is taken into account to interpret the temperature differences between experiments and models. As described previously, the scattering angle of an oblate droplet is large than that of a spherical droplet. Therefore, taking the simulated temperature values as references, the measured temperatures can be modified to optimum values by assuming an appropriate non-sphericity of droplet shape. **Figure 4.18** compares the resulting temperature evolutions after correction. When the droplets are generated from the pinhole sizes of 75 μm and 100 μm, the modifications of shape change are considered. As indicated, ethanol droplets with the non-sphericity of 1.002 and 1.007 generate good consistency with the simulation results. Likewise, the non-sphericity of heptane droplets is 1.001 and 1.003 respectively for two droplet sizes. It shows that the non-sphericity of heptane droplets is smaller than that of ethanol droplets. This can be explained by the fact that the heptane droplet stream has a slower falling velocity than ethanol droplets. The present

results confirm the possibility of shape change as well as its impact on the rainbow measurements. On the other hand, the spheroidal droplet shape well explains the deviation between the measurements and simulation, which provides a different sight to interpret the experimental results.

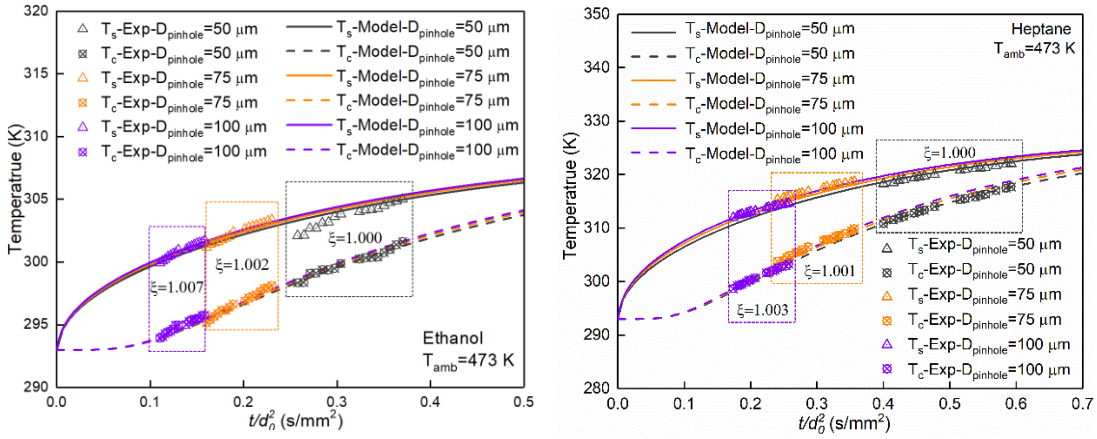

(a) Ethanol droplet **(b) Heptane droplet**

Figure 4.18 Temperature evolutions considering the shape change.

4.4 Summary

The transient evaporation characteristics of free-falling ethanol and heptane droplets under ambient temperatures of 373-473 K are investigated in this chapter with the rainbow technique. By analyzing the rainbow patterns captured in the vicinity of rainbow angle, the droplet size, the equivalent temperature of droplet together with the temperature values inside droplet has been simultaneously extracted. Some of the conclusions are summarized as follows:

1. Both the primary peaks and the ripple structures are distinctly presented in the rainbow images by using the present experimental configuration. It is observed that the rainbow pattern shifts to lower scattering angles by enhancing ambient temperature. While the particle with a larger size tends to have more peaks within the same scattering angle range.
2. The impact of ambient temperature, the initial droplet diameter, and the fuel type on the reduction rate of droplet size and heating rate in the liquid phase has been obtained. The results indicate that less volatile droplets are more likely to be affected by the change of ambient temperature or the initial droplet

size compared with more volatile droplets.

3. The experimental measurements show good agreement with the simulation results in the variation of diameter. However, the discrepancy between the measured temperatures and predicted values is observed, which originates from the temperature gradient in the liquid phase.
4. The parabolic distribution of refractive index along the radius direction is validated. The underlying relationship between the measured temperature and the temperature gradient inside the droplet is revealed. The temperature distributions in the liquid phase are obtained from the rainbow measurements.

5. Preferential evaporation of binary droplets

This chapter aims to investigate the evaporation characteristics of binary droplets under different conditions with the rainbow technique and numerical model. The influence of non-ideal vapor-liquid equilibrium (VLE) on the preferential behavior of ethanol/heptane droplets is revealed and validated. The mixture of heptane and ethanol has been adopted as tested fuel. Simulations have the same boundary and initial conditions as the experiment when conducting the comparative study with experiments.

5.1 Evaporation characteristics of binary droplets

The evaporation process of ethanol/heptane droplet is performed by both the ideal and non-ideal VLE methods in this section. As described before, three correction parameters, the activity coefficient, the Poynting factor, and the fugacity coefficient, are incorporated in the Effective Conductivity Model (ECM) and Effective Diffusivity Model (EDM) to present the non-ideal behavior at the droplet surface. The ambient temperature and pressure are 373 K and 473 K, 1 bar and 10 bar, respectively. The initial volume fraction of ethanol in the mixture ranges from 0.25 to 0.75. Accordingly, the nomenclature 'ETH25', 'ETH50', and 'ETH75' stand for the initial volume fraction of ethanol in the mixture with 25%, 50%, and 75%, respectively. The initial diameters of the three kinds of droplets are 109.90 μm, 108.63 μm, and 107.46 μm, which is consistent with the experimental conditions. In all cases in this section, the initial droplet temperature is 293 K with a velocity of 6.5 m/s. The 'NI-Model' and 'I-Model' mean the non-ideal equilibrium model and ideal equilibrium model respectively. Component 1 stands for heptane and component 2 is ethanol. Therefore, the separation factor α_{12} presents the relative volatility of heptane to ethanol. The ambient conditions and liquid composition of all the investigated cases in this section are listed in **Table 5.1**.

Table 5.1 Lists of the ambient conditions and liquid compositions of model.

Case	T_{amb} (K)	P_{amb} (bar)	Y_1 (Heptane by volume %)	Y_2 (Ethanol by volume %)
Section 5.1.1	373	1	25-75	75-25
Section 5.1.2	373	1	25-75	75-25

Section 5.1.3	373	1	25-75	75-25
	373	10	25-75	75-25
	473	1	25-75	75-25
	473	10	25-75	75-25

5.1.1 Variation of droplet size and temperature

Figure 5.1 gives the temporal evolution of normalized squared droplet diameter and surface temperature with different ethanol mass fractions by using the NI-Model and I-Model, respectively. Initially, the result presents the relationship between the mass fraction of ethanol and droplet lifetime. The larger initial concentration of ethanol in the liquid phase leads to a longer droplet lifetime. This behavior looks contradicted with normal cognition at first sight because ethanol has a much lower boiling point than heptane. Concerning it, increasing the proportion of more volatility component in the mixture would accelerate the evaporation rate and shorten evaporation time. Despite this, it is necessary to note the influence of latent heat when ethanol appears in the mixture. Since the latent heat of ethanol is considerably higher than the value of heptane, the surface temperature of ethanol is much lower than that of heptane under the same ambient condition. Therefore, adding ethanol into the mixture results in a relatively longer droplet lifetime. The result consents well with the evaporation behavior of individual components investigated in chapter 4.

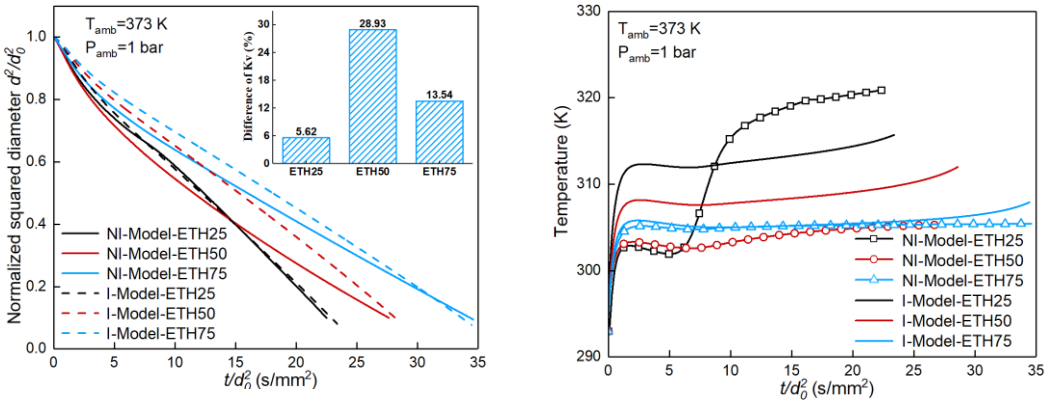

(a) Normalized diameter **(b) Surface temperature**

Figure 5.1 Variation of droplet normalized droplet diameter and surface temperature for ideal and non-ideal cases at T_{amb}=473 K and P_{amb}=1 bar.

Additionally, the difference between the NI-Model and I-Model predictions is

observed in the evaporation curves, as shown in **Figure 5.1**a. Here, the evaporation constant (denoted as K_V) is used to present the difference of those two methods, which is derived by linearly fitting the curve of normalized squared droplet diameter in the range of 0.15-0.5 [23]. In this context, the difference between the evaporation constant obtained by the NI-Model and I-Model is defined as,

$$D(\%)=\left|\frac{K_{V,NI}-K_{V,I}}{K_{V,NI}}\right|\times 100, \tag{5.1}$$

where $K_{V,NI}$ and $K_{V,I}$ are the evaporation constant for NI-Model and I-Model, respectively. The comparison is made in the subplot of **Figure 5.1**a. The results show that the deviations of evaporation constant between the NI-Model and I-Model are extremely large for ETH50 and ETH75 droplets, with a value of 28.95% and 13.54%, respectively. When it comes to ETH25 droplets, the deviation is relatively smaller than the other two composition cases.

The difference also appears in the temperature evolution obtained by those two methods. It is observed the droplet temperature experiences a rapid increase in the early heating period. After a short while, the droplet heating rate gradually slows down and reaches the quasi-steady state, which is the result of a balance between sensible and latent heat. The divergence between NI-Model and I-Model is evident especially after the initial heating period, as indicated in **Figure 5.1**b. For the I-Model predictions, the pseudo-state temperature decreases with the initial ethanol concentration in the liquid phase. However, for the results of the NI-Model, the pseudo-state temperature for ETH50 and ETH75 droplets is closer to that of ethanol, while the pseudo-state temperature for ETH25 is more comparable to heptane. This behavior is caused by the preferential evaporation of individual components in the mixture. For binary or multi-component droplet, the lighter components evaporate at a different timing than the heavier components, depending on the physical properties or ambient conditions. This specific fashion of evaporation behavior is normally referred as preferential evaporation [147]. In general, the droplet temperature at the end of evaporation should always approach the adiabatic evaporation temperature of the residual component. Therefore, the differences in temperature evolution between the NI-Model and I-Model predictions imply a distinct change of the preferential evaporation inside the mixture.

5.1.2 Preferential evaporation of heptane and ethanol

The discrepancies between the NI-Model and I-Model in modeling the droplet diameter and temperature provide a clue for the evaporation order of heptane and ethanol components in the mixture. **Figure 5.2** displays the evolutions of surface mass fraction of heptane and ethanol obtained from the NI-Model and I-Model. It should be noted that the surface mass fraction is a major parameter in deciding the mass and heat transfer rate, as well as the preferential evaporation behavior of individual components inside a multi-component droplet. The increase or decrease of the mass fraction with time denotes the evaporation sequence of two components. Here, a significant difference in the variation of mass fraction between the NI-Model and I-Model is observed. For all I-Model results, the heptane mass fraction at the droplet surface gradually increases with time, while the ethanol mass fraction has a reduction trend with time. The variation tendency of heptane and ethanol is always positive or negative regardless of the initial composition in the liquid phase. In other words, the evaporation order of those two components is always the first vaporization of ethanol followed by heptane in any case.

However, for NI-Model predictions, the vaporization order changes depending on the initial composition in the mixture. Heptane can evaporate faster or slower than ethanol. For ETH50 and ETH75 droplets, heptane evaporates faster than ethanol as denoted by the decreasing mass fraction of heptane with time. While for the ETH25 droplet, the evaporation order reverses. The alteration of the evaporation sequence is due to the influence of the non-ideality of the mixture presented by the molecular interactions.

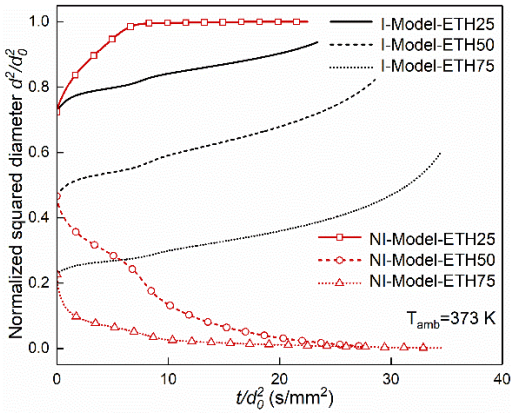

(a) Surface mass fraction of heptane

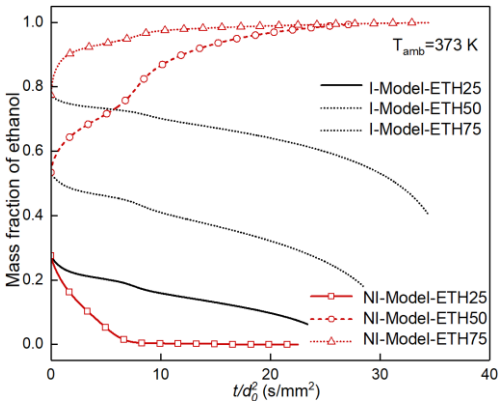

(b) Surface mass fraction of ethanol

Figure 5.2 Comparison of the surface mass fraction of heptane and ethanol for I-Model and NI-Model at T_{amb}=473 K and P_{amb} =1 bar.

As mentioned previously, the separation factor is a critical parameter for comprehending the order vaporization of multi-component droplets. **Figure 5.3** provides the evolution of the separation factor for the binary system. It can be seen the variation of separation factors agrees well with the change of mass fraction. Firstly, the separation factors for all the ideal droplets are below 1. This consents with the sequence evaporation behavior, with the first evaporation of ethanol and followed by heptane because ethanol has a lower boiling point than its counterpart heptane. By contrast, for the NI-Model system, the separation factor is larger than 1 for ETH50 and ETH75 droplets, which leads to the inversion of the evaporation order compared with the ideal cases. This indicates liquid composition is decisive for the evaporation order.

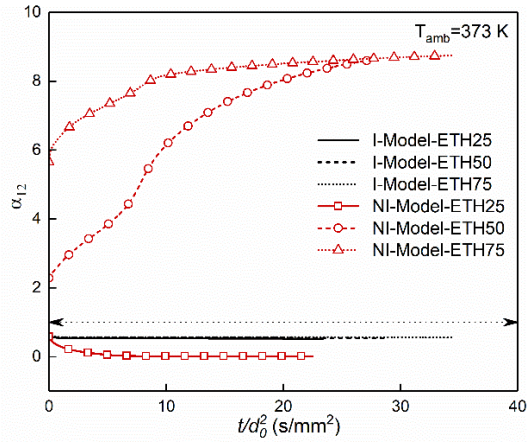

Figure 5.3 Evolution of separation factor in the binary system for ideal and non-ideal cases at T_{amb}=473 K and P_{amb} =1 bar.

5.1.3 The non-ideal behavior under different conditions

This section focuses on the impact of ambient conditions on the non-ideal behaviors by varying the ambient temperature up to 473 K and ambient pressure of 10 bar. The other initial conditions are the same as the last section. Firstly, the variation of normalized droplet diameter and surface temperature under different conditions are presented in **Figure 5.4**. In general, the evaporation and heating processes of droplets under those conditions are quite similar to the result obtained under 373 K and 1 bar ambient conditions. The initial increase in droplet diameter is caused by thermal

expansion when droplets are exposed to high temperature and pressure conditions.

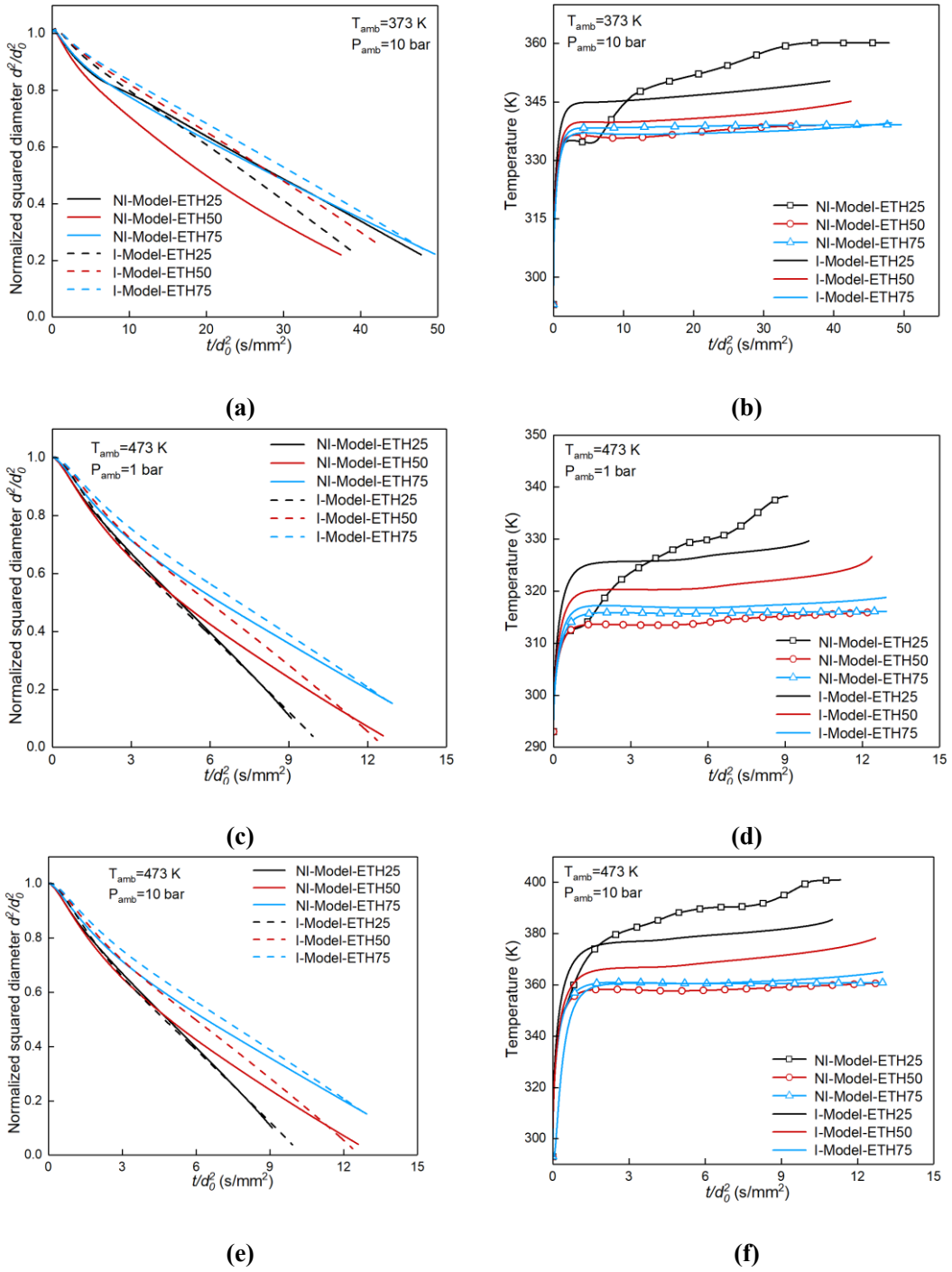

Figure 5.4 Evolution of normalized squared diameter and surface temperature for ideal and non-ideal cases at different ambient conditions; (a) and (b) are the ambient condition of T_{amb}=373 K and P_{amb} =10 bar; (c) and (d) are for T_{amb}=473 K and P_{amb} =1 bar; (e) and (f) correspond to T_{amb}=473 K and P_{amb} =10 bar.

As described before, for ideal VLE, the separation factor depends only on the temperature. While both the pressure and temperature coupled with the liquid

composition affect the separation factor for the non-ideal approach. The variation of the separation factors for all the cases is compared in **Figure 5.5**. Firstly, the separation factors for all the I-Model cases are similar and less than 1 as expected. In contrast, the separation factors evaluated by the NI-Model for ETH50 and ETH75 droplets differ appreciably with the I-Model results, having values considerably larger than 1. For ETH25 droplets, the NI-Model results are much closer to the I-Model. This indicates that when the concentration of the less volatility component in the mixture is large, the liquid can be regarded as ideally to some extent. When the lighter component dominates the mixture, the assumption of the ideal mixture is not valid.

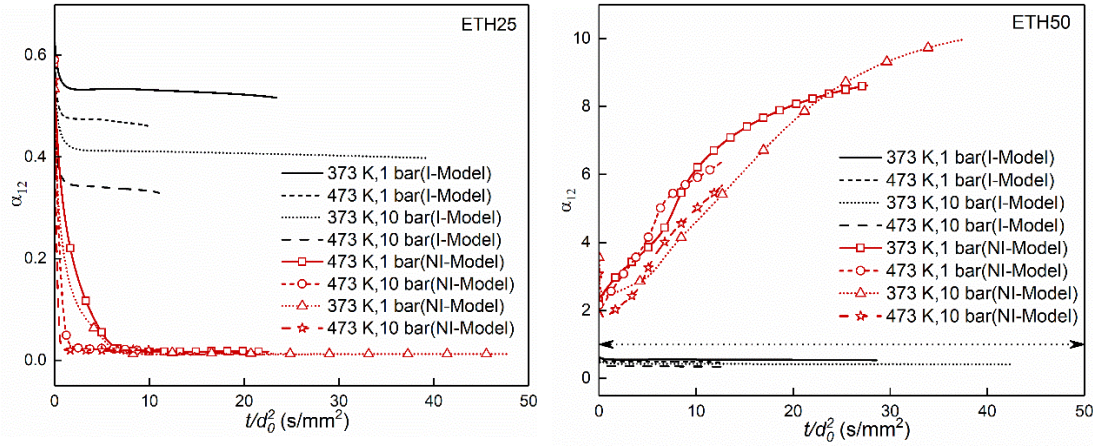

(a) ETH25 droplet **(b) ETH50 droplet**

(c) ETH75 droplet

Figure 5.5 The variation of the separation factor for three types of droplets under all the conditions.

Secondly, enhancing ambient temperature and pressure has a slight influence on the separation factor for ETH50 droplets as the differences under different conditions

are trivial as shown in **Figure 5.5**b. By contrast, for ETH75 droplet, increasing ambient temperature diminishes the value of α_{12} to a large extent as displayed in **Figure 5.5**c. Besides, a higher ambient pressure leads to a larger α_{12} under 373 K yet a lower α_{12} under 473 K condition. The variation of α_{12} under different ambient conditions for ETH50 and ETH75 droplets conveys the information that the ambient condition alters the relative volatility in the mixture quantitatively. In general, the value of separation factors is relatively smaller under higher ambient temperature and pressure conditions. This means the difference in the physical properties between individual components in the mixture is weakened by increasing ambient temperature and pressure because of the thermodynamic influence. It discloses that the non-ideal equilibrium is more likely to be affected by ambient conditions when the lighter components dominant the mixture.

5.2 Comparison against rainbow measurement

This section aims to investigate the ability of the rainbow technique in measuring the evolution of temperature, size, and composition during the binary droplet evaporation process. As presented by the simulation results, the non-ideal vapor-liquid equilibrium has an obvious impact on the temperature evolution and preferential evaporation of heptane/ethanol droplets. It is rare to examine this difference from the perspective of the experiment to the author's knowledge. However, the rainbow measurement can check this distinct evaporation behavior of binary droplets. The main thinking is to pick the most similar evolutions of refractive index in the liquid phase by comparing the refractive index of rainbow measurement with the refractive indices obtained from two models. This can validate the accuracy of different models as well as interpret the temperature and concentration distributions of each component inside the droplet, which gives a new sight to measure the evaporation behavior of binary droplets. **Table 5.2** lists the key parameters for experiments.

Table 5.2 Key parameters of experimental conditions.

	Section 5.2	Section 5.3.1	Section 5.3.2
Initial temperature (K)	293	293	293
Initial velocity (m/s)	6.5	6.5	6.5
Injection pressure (bar)	1.2	1.2	1.2

Injection frequency (kHz)	26.13	26.13			26.13		
Pinhole diameter (μm)	50	50		50	75		100
Initial volume fraction of ethanol	0.25 0.50 0.75	0.25 0.75			0.5		
Initial diameter (μm)	109.90 108.63 107.46	109.90 108.63			108.63 143.62 173.98		
Ambient temperature (K)	373	373	473	373			473

5.2.1 Transient variation of diameter and refractive index

The variation of normalized diameter with time obtained by the experimental method and two models for ethanal and heptane binary droplets are compared in **Figure 5.6**. As indicated, during the transient heating stage, two methods show an obvious difference in predicting the evolution of normalized diameter. The model using the ideal equilibrium has a smaller reduction in diameter by contrast with the non-ideal equilibrium prediction. The measurements from the rainbow experiment validate the accuracy of the model adopting the non-ideal equilibrium. This reveals that the influence of non-ideal equilibrium cannot be neglected for binary mixture with distinct physical properties of each component. Apart from that, it is observed that the reduction rate of droplet diameter tends to decrease with the increase of ethanol mass fraction. Despite the ethanol being much lighter and having a lower boiling point, adding more ethanol into the mixture depresses the droplet shrinkage as ethanol has a higher latent heat of vaporization, which consents well with the evaporation behavior of individual components as investigated in chapter 4.

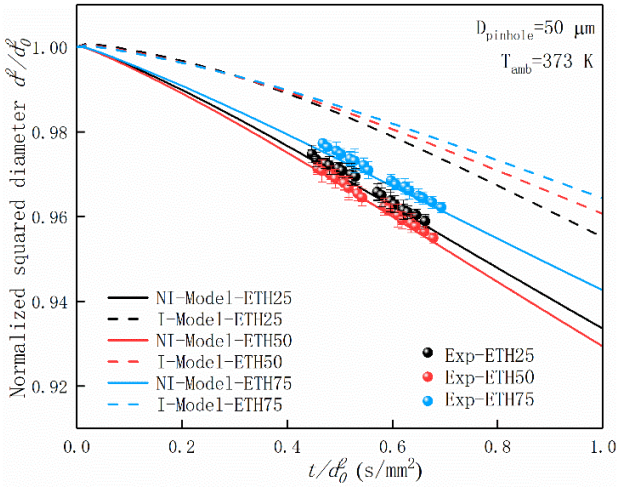

Figure 5.6 Variation of normalized droplet diameter.

For binary droplets, the temperature and component mass fraction have a coupled influence on the resulting refractive index, which makes it impossible to get the values of those two parameters directly from the measured refractive index. Therefore, retrieving the value of temperature and concentration from the rainbow measurements needs the help of the simulation model. The idea is to compare the experimental results with the equivalent refractive obtained by the non-ideal equilibrium and ideal equilibrium, from which choosing the best fitting curves of simulation.

In the first, the models predict the spatial distribution of refractive index along radius direction at different instants, as shown in **Figure 5.7**. The spatial distributions of the refractive index of three droplets are similar to each other for the ideal equilibrium method, i.e., the refractive index reduces andante from the droplet center to the surface at all instants. By contrast, the difference between the ideal and non-ideal predictions is distinct for all cases. For ETH50 and ETH75 droplets, the refractive index reduces appreciably from center to surface for non-ideal equilibrium predictions. While the refractive index of the ETH25 droplet has a completely different distribution with a much higher value at the droplet surface. The major difference between different predictions is at the position approaching the droplet surface. It is observed that the reduction tendency is similar to each other when the non-dimensional radius is smaller than 0.6. After that, the ideal equilibrium method has a slight rebound, whereas the non-ideal equilibrium method has a sharp reduction for ETH50 and ETH75 droplets, and a rapid increase for ETH25 droplet. Theoretically, the light path inside droplet spreads

from the droplet surface to the non-dimensional radius of 0.6. Therefore, not all the liquid phase affects the light path and the resulting rainbow angle. Only the range from non-dimensional radius 1 to 0.6 is effective, which is defined as the impact zone.

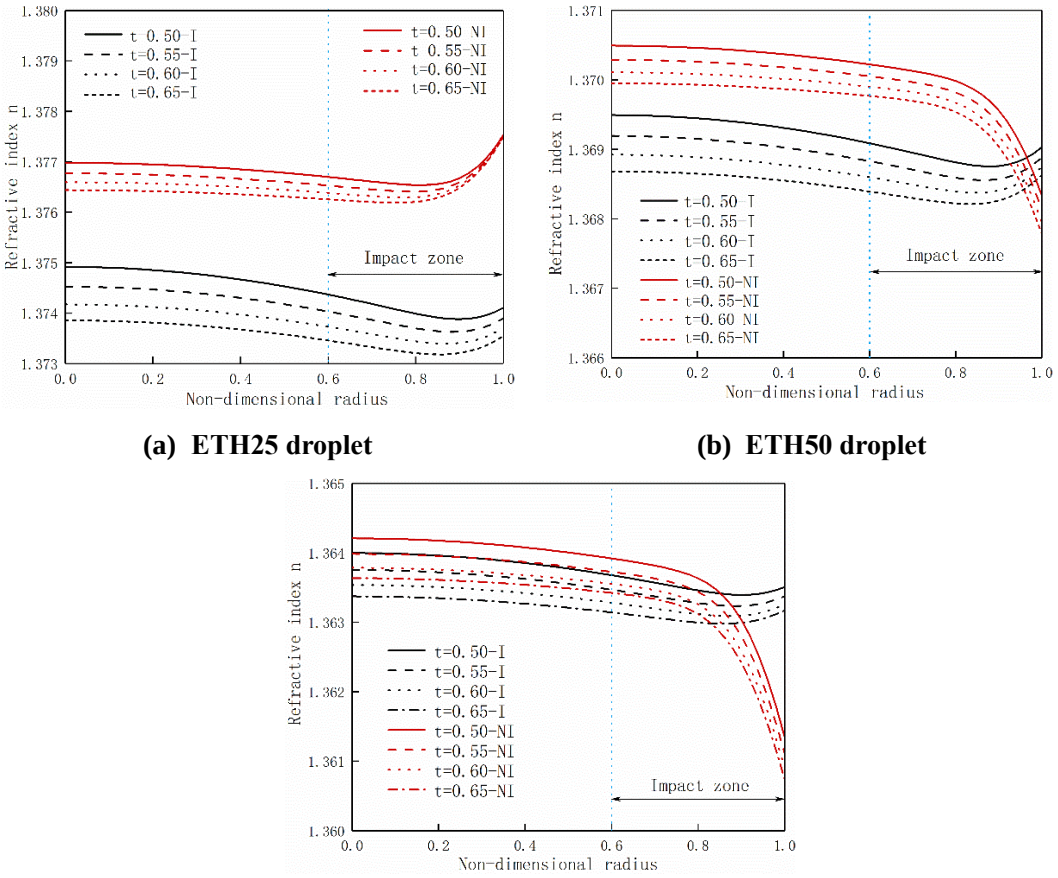

(a) ETH25 droplet **(b) ETH50 droplet**

(c) ETH75 droplet

Figure 5.7 The spatial distributions of the refractive index of three droplets obtained by two models under the ambient temperature of 373 K.

The contrary variation trend of refractive index between ETH25 and ETH75 droplets indicates that the evaporation scenery at the droplet surface of ETH25 is different from that of ETH50 and ETH75 droplets. **Figure 5.8** compares the spatial distribution of temperature and mass fraction of heptane for ETH25 and ETH75 droplets. All the results predicted by the ideal-equilibrium method have the same variation of mass fraction with advanced evaporation of ethanol and the accumulation of heptane at the droplet surface. When it comes to the non-ideal equilibrium predictions, the evaporation sequence depends on the individual droplet. For the ETH25 droplet, the ethanol is evaporated preferentially at the droplet surface, which leads to

the accumulation of heptane and the growth of refractive index. However, for ETH75 droplets, the heptane has prior evaporation at the droplet surface. Accordingly, ethanol cumulates at the droplet surface and brings about the reduction of the refractive index. The results reveal that the composition in the liquid phase has a decisive impact on the variation of the refractive index in the impact zone.

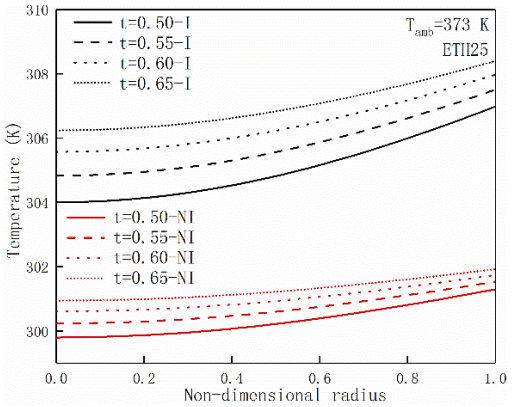

(a) Temperature of ETH25 droplet

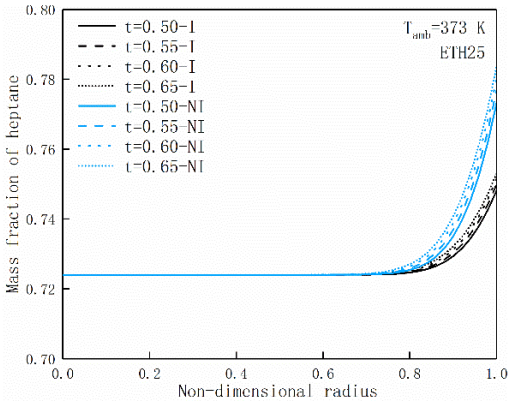

(b) Mass fraction of heptane for ETH25 droplet

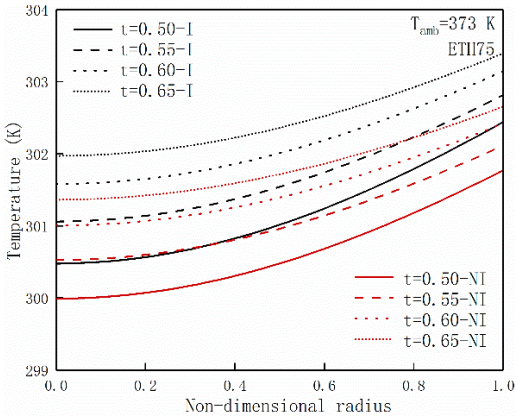

(c) Temperature of ETH75 droplet

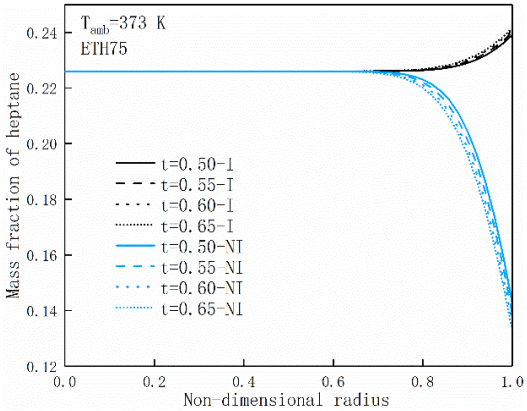

(d) Mass fraction of heptane for ETH75 droplet

Figure 5.8 The spatial distribution of temperature and mass fraction of heptane.

5.2.2 Comparison of the equivalent refractive index

This part explores the variation of equivalent refractive index with polynomial fittings. **Figure 5.9** compares the fitting curves of the refractive index for the non-ideal equilibrium method and ideal equilibrium predictions with different polynomial orders. Focusing on the impact zone, two curves at instants of 0.5 and 0.65 are fitted by three

polynomial orders, respectively. On one hand, the variations of refractive index by the ideal equilibrium method for all three droplets are consistent with each other, which can be fitted by the polynomial order of 1. On the other hand, for non-ideal equilibrium predictions, the optimum fit order varies from 8 to 5 with time for the ETH25 droplet. While the ETH50 droplet has the most satisfactory results with a polynomial order of 4 at t=0.5 and 3 at t=0.65, which is the same as the ETH75 droplet. This reveals a trend that the polynomial order and the corresponding refractive gradient reduce with time.

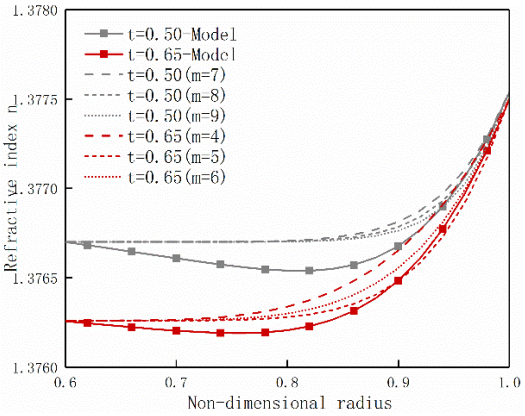

(a) The non-ideal equilibrium of ETH25

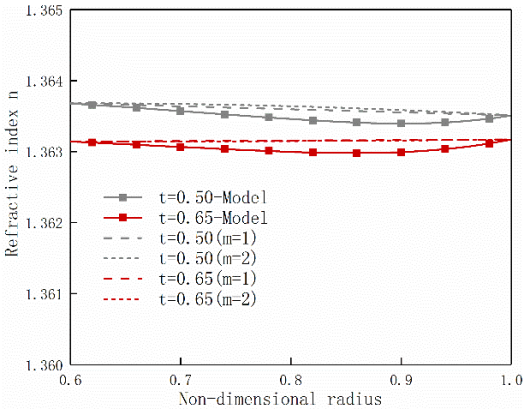

(b) The ideal equilibrium method of ETH25

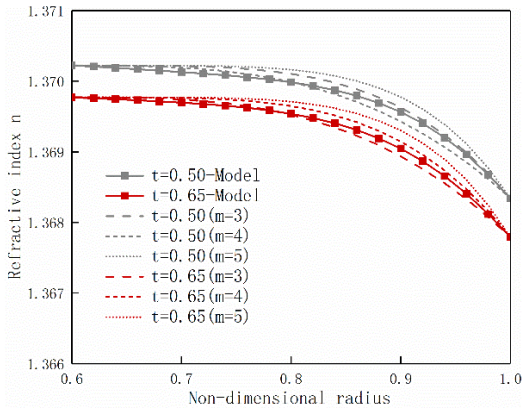

(c) The non-ideal equilibrium of ETH50

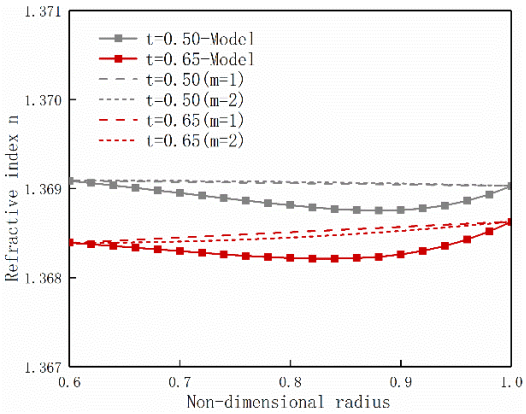

(d) The ideal equilibrium method of ETH50

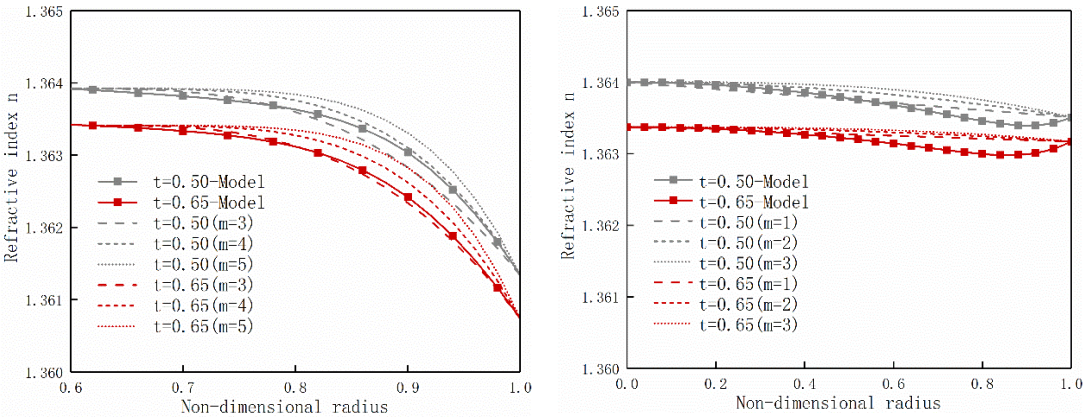

(e) The non-ideal equilibrium of ETH75 **(f) The ideal equilibrium method of ETH75**

Figure 5.9 The refractive index simulated with different polynomial orders for ETH25, ETH50, and ETH50 droplets.

The relation between the equivalent refractive index and the polynomial order is compared in **Figure 5.10**. The variation tendency of the equivalent refractive index for the ETH50 and ETH75 droplets is consistent with each other. By contrast, the ETH25 droplet shows a converse variation trend. For the ETH25 droplet, the results reveal that when the refractive index at the droplet surface has a larger value, the equivalent refractive index firstly increases then decreases with the polynomial order. The equivalent refractive index corresponding to a polynomial order 1 is inside the refractive indices range of the liquid phase. While the other equivalent refractive indices are smaller than the refractive index range of the liquid phase. Besides, the equivalent refractive index deriving from 8 to 5 differs trivially. For the other ETH50 and ETH75 droplets with a larger refractive index at the droplet center, the equivalent refractive index resulting from a polynomial order 1 is also in the refractive indices range of the liquid phase. Whereas the rest equivalent values locate above the refractive index range of the liquid phase. Therefore, the equivalent refractive indices from the ideal and non-ideal equilibrium methods have a significant difference.

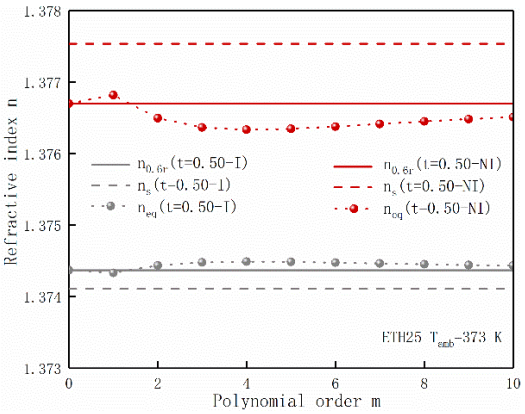

(a) ETH25 droplet

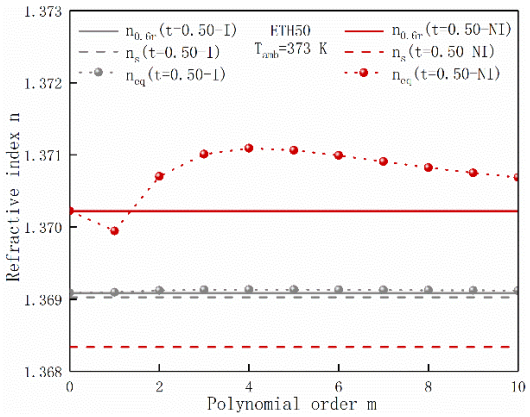

(b) ETH50 droplet

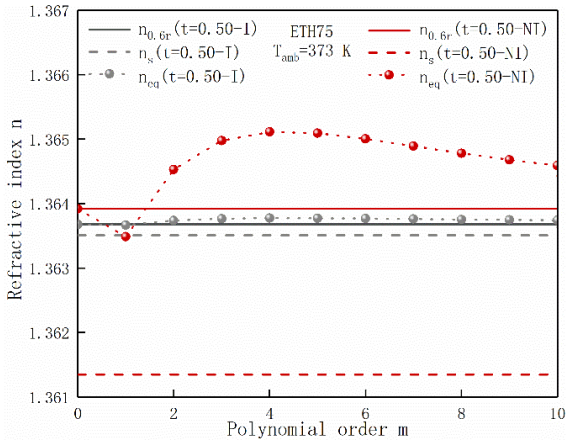

(c) ETH75 droplet

Figure 5.10 The equivalent refractive index with polynomial order for ETH25, ETH50, and ETH75 droplets.

The evolution of the refractive index from model prediction and experimental measurements are compared in **Figure 5.11**. The refractive indices at the center and surface of the droplet are also plotted for comparison. For the non-ideal equilibrium model, the equivalent refractive indices with two polynomial orders have been displayed. The results indicate that the refractive index reduces gradually with time. In addition, the differences of refractive index among droplet surface, droplet center, and the equivalent refractive index are tiny for ideal equilibrium prediction but apparent for non-ideal equilibrium predictions. The differences of the equivalent refractive index between the two models for all types of droplets are evident. The results show that the non-ideal equilibrium predictions are more consent with the experimental measurements for ethanol and heptane binary droplets. Although the polynomial order experiences a variation from 8 to 5 for ETH25 droplet and from 4 to 3 for ETH50 and

ETH75 droplet respectively, the equivalent refractive index because of the order change is unobvious. The experimental results validate the accuracy of non-ideal equilibrium simulation in predicting the temperature and concentration as well as the necessity of considering the impact of the non-ideal mixture.

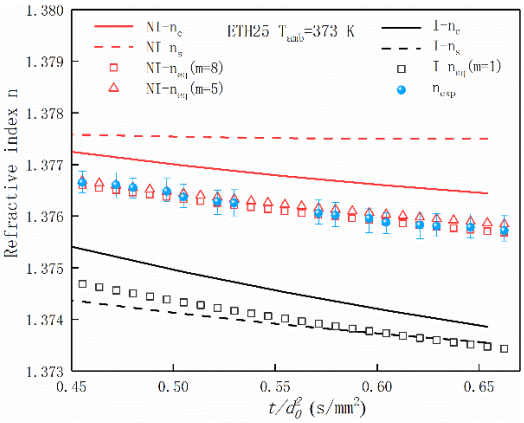

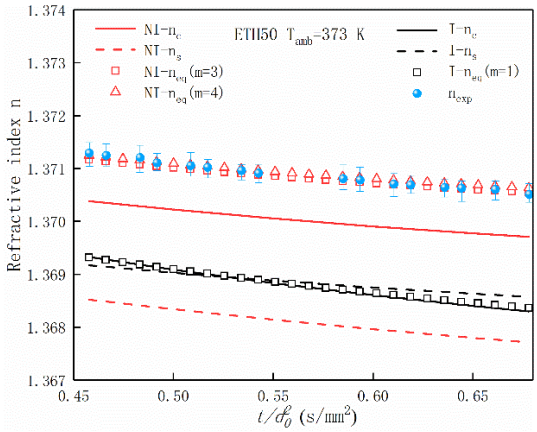

(a) ETH25 droplet **(b) ETH50 droplet**

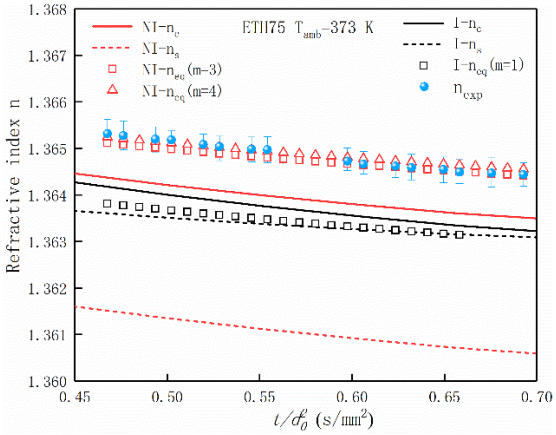

(c) ETH75 droplet

Figure 5.11 The comparison of refractive index between model and experiment for ETH25, ETH50, and ETH75 droplet.

5.2.3 Overall variation of refractive index

The temporal evolutions of the refractive index at the center and surface of different droplets are illustrated in **Figure 5.12**. The results indicate a considerable difference not only in the numerical value but also in variation tendency. In the first, for ETH25 droplet, the refractive index from the non-ideal equilibrium model experiences three segments including decrease, increase, and again decrease section. By contrast, the ideal equilibrium model produces a sharp decay and slightly growing refractive

index. Regarding the other two droplets, the refractive index keeps declining all the time for non-ideal equilibrium predictions. Nevertheless, the ideal equilibrium models generate similar variation trends with the ETH25 droplet. Taking the refractive index at droplet surface as an example, the maximum deviations of ideal equilibrium prediction from the non-ideal equilibrium results are 0.009, 0.018, and 0.013 respectively. Consistent behavior is the refractive index inside droplet declines with increasing the mass fraction of ethanol. This is due to the refractive index of ethanol being intrinsically smaller than that of heptane.

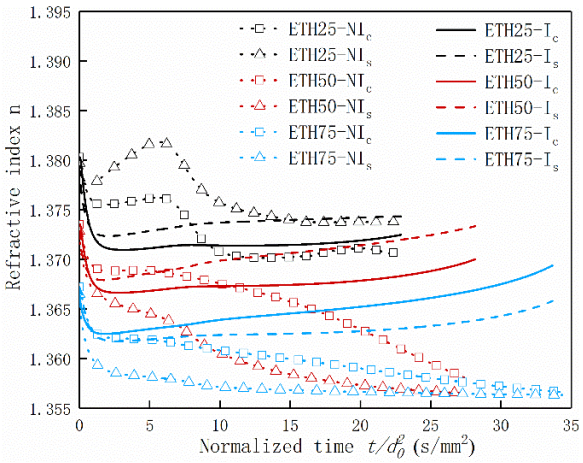

Figure 5.12 The variation of normalized diameter and refractive index of different droplets.

The overall temperature and concentration evolutions are displayed in **Figure 5.13** to comprehend the temporal variation of the refractive index. For non-ideal equilibrium prediction, the quasi-steady temperature of ETH25 droplet is higher than the other two droplets approaching the wet-bulb temperature of heptane. For ETH50 and ETH75 droplets, their quasi-steady temperature is close to each other with a value of 305 K. That is, adding more ethanol into the mixture tends to reduce the quasi-steady temperature, which accordingly declines the evaporation rate. The mass fraction of heptane declines with time for ETH50 and ETH75 droplets, whereas increases for ETH25 droplet. The temperature together with the composition decides the variation of the equivalent refractive index. In the initial stage, the sharp decrease of refractive index is the outcome of intensive droplet heating. Later, the composition dominates the variation of refractive index for the rest of the droplet lifetime for ETH50 and ETH75 droplets. For the ETH25 droplet, the second rapid heating stage of the droplet takes

over the control of the refractive index, which modifies the refractive index curve from rising to falling.

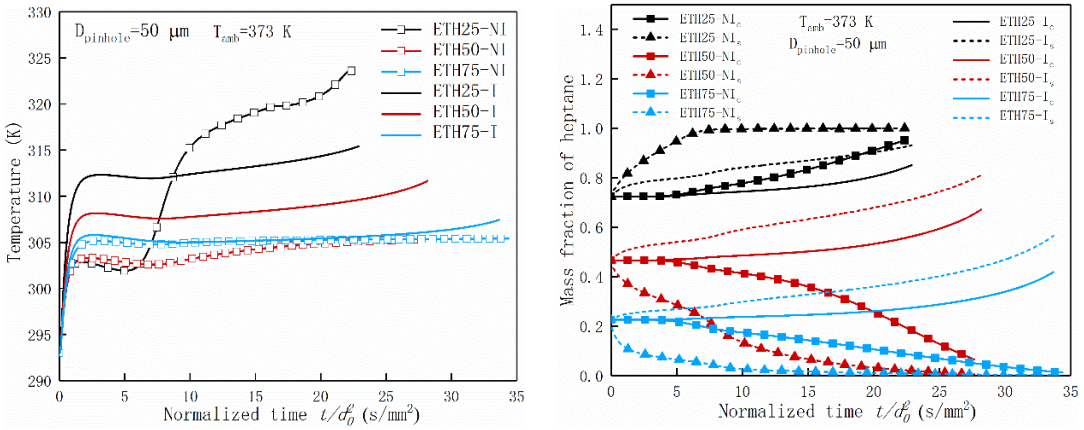

(a) Temperature **(b) Mass fraction of heptane**

Figure 5.13 The evolution of temperature and mass fraction of heptane for different droplets.

5.3 Comparative investigation of binary droplet evaporation

This section sheds a light on the variation of normalized diameter and refractive index with time obtained by the experimental and numerical method for ethanal and heptane binary droplets under different configurations. The coupling influence of temperature and concentration on the refractive index has been revealed. Three types of droplets, namely ETH25, ETH50, and ETH75, are investigated under the ambient temperature of 373 K and 473 K. The pinhole sizes are in the range of 50-150 μm.

5.3.1 Evaporation characteristics under different ambient conditions

Figure 5.14 compares the evolutions of diameter and refractive index of ETH25 and ETH75 droplets under the ambient temperature of 373 K and 473 K conditions. The pinhole size is 50 μm. For ETH25 droplet, the evaporation rate during this transient period is enhanced from 0.07 mm^2/s under 373 K to 0.135 mm^2/s under 473 K. By contrast, the evaporation rate increases from 0.067 mm^2/s to 0.116 mm^2/s by enhancing ambient temperature for ETH75 droplet. Therefore, increasing ambient temperature from 373 K and 473 K promotes the evaporation rate ETH25 and ETH75 droplets by 92.86% and 73.13% respectively. Increasing ambient temperature enhances the

evaporation rate of the heavier droplet to a more extent. This reveals that binary droplet with a much heavier component is more sensitive to the change of environment.

Comparing the refractive index variations under 373 K and 473 K, it is found that increasing ambient temperature reduces the refractive index, which holds for both ETH25 and ETH75 droplets. For ETH25 droplet, the overall variation refractive index at the droplet surface is larger than that at the droplet center. The difference of refractive index between droplet surface and center is relatively large under 473 K with a maximum value of 0.0028 compared with a maximum of 0.0013 under 373 K temperature conditions. This indicates that enhancing ambient temperature enlarges the gradient of refractive index in the liquid phase for ETH25 droplets. On the other hand, for the case of ETH75 droplet, the refractive index at the droplet center is always higher than that at the droplet surface under two ambient temperatures. The maximum differences of refractive index between droplet surface and center are 0.004 under 473 K and 0.0027 under 373 K, respectively. For ETH25 droplet, the reductions of refractive index during the present research range are 0.001 and 0.0026 respectively under 373 K and 473 K conditions. While the refractive index of ETH75 droplet reduces 0.001 and 0.0013 under 373 K and 473 K respectively. The reduction rate of the refractive index is promoted by enhancing ambient temperature. In a nutshell, the ETH25 droplet with a much heavy component in the liquid phase is more likely to be affected by the environment change as a result of the enlargement of the refractive index difference in the liquid phase and the promoted reduction rate of the refractive index under 473 K condition. This behavior is consistent with the variation of diameter.

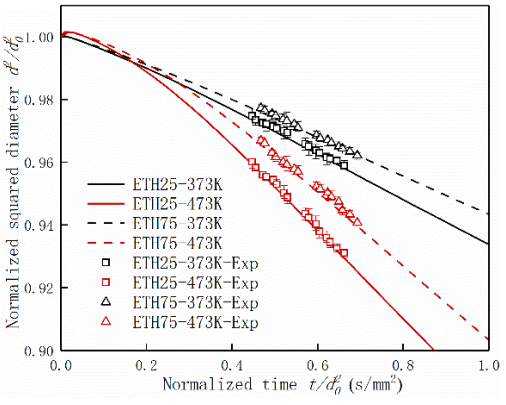

(a) Diameter

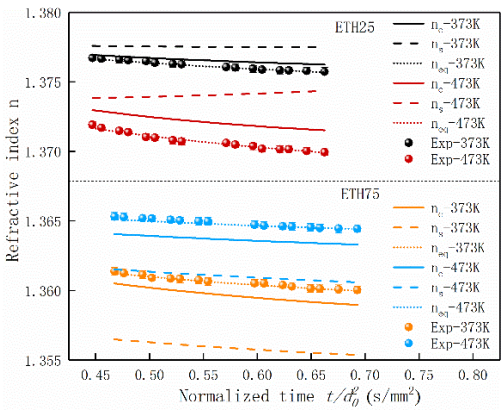

(b) Refractive index

Figure 5.14 The variation of normalized diameter and refractive index of ETH25 and ETH75 droplets under 373 K and 473 K.

The spatial distributions of temperature and mass fraction for ETH25 and ETH75 droplets under 373 K and 473 K are plotted in **Figure 5.15**. The temperature distribution and evolution presented in **Figure 5.15**a have the same variation tendency under different ambient conditions. However, the ETH25 droplet always maintains a lower temperature than the ETH75 droplet. In addition, the temperature, as well as the temperature gradient in the liquid phase under 473 K, is larger than that under 373 K conditions, which reveals a faster heating rate in the liquid phase. For the mass fraction of heptane, ETH25 and ETH75 droplets have a converse variation trend. Despite that, enhancing the ambient temperature impacts the evolutions of mass fraction in the same way, i.e., leading to a larger concentration of heptane for ETH25 droplet and a smaller mass fraction of heptane for ETH75 droplet under 473 K, which reveals the promotion of mass regression by increasing ambient temperature.

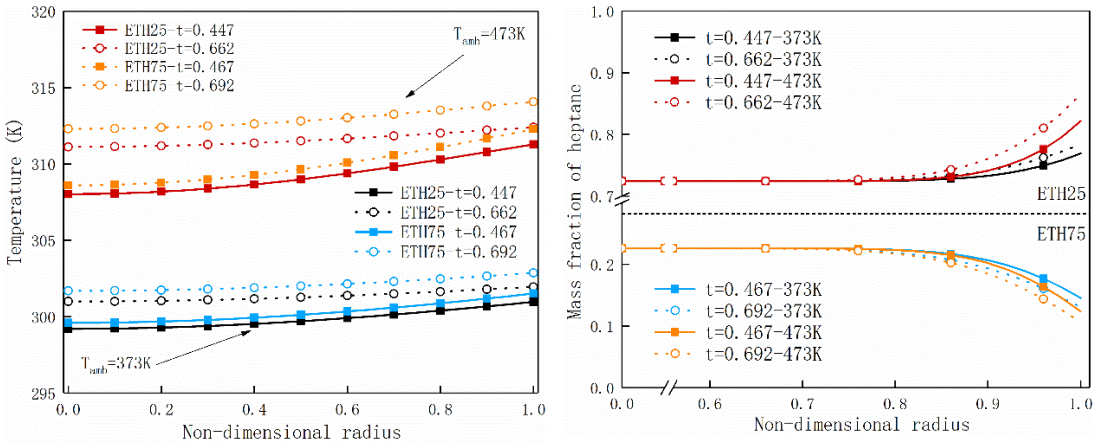

(a) Temperature evolutions **(b) Mass fraction evolutions**

Figure 5.15 The spatial distribution of mass fraction and temperature.

5.3.2 Droplet evaporation with different sizes

The evaporation characteristics of droplets produced from three pinhole sizes of 50, 75, and 100 μm are investigated in this section. Taking the ETH50 droplet as an example, the initial droplet diameters generated from three pinholes are 109.66, 143.62, and 173.98 μm respectively. As compared in **Figure 5.16**. the normalized droplet

diameter reduces with time for all droplet sizes. As the time after normalization differs obviously from each other among three droplets, it is difficult to tell the influence of droplet size on the diameter evolutions. Therefore, the reduction rate of diameter is plotted in **Figure 5.16**b. The results show a negative impact of droplet size on the reduction rate of diameter for experimental measurements during the present stage under both 373 K and 473 K ambient conditions. In addition, the reduction rate of diameter is greatly enhanced by increasing ambient temperature. Accordingly, the inhibition impact by increasing droplet size is more pronounced under 473 K.

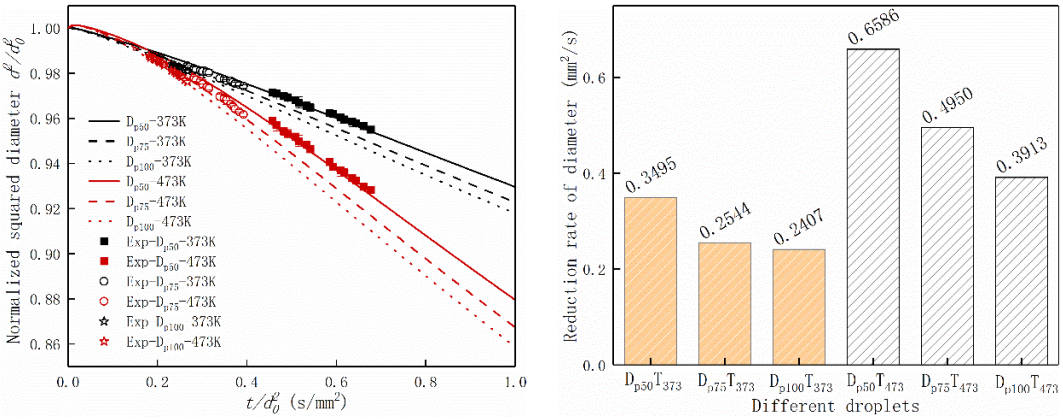

(a) Normalized droplet diameter **(b) Reduction rate of diameter**

Figure 5.16 The regression of diameter for three droplet sizes.

Next, the refractive index of three droplets under 473 K is compared in **Figure 5.17**. It indicates that a larger droplet has a higher refractive index value. ETH50 droplets with different initial diameters have a similar distribution in the liquid phase, i.e., a higher refractive index at the droplet surface and a lower refractive index at the droplet center. As a consequence, the resulting refractive index is larger than the refractive indices in the liquid phase.

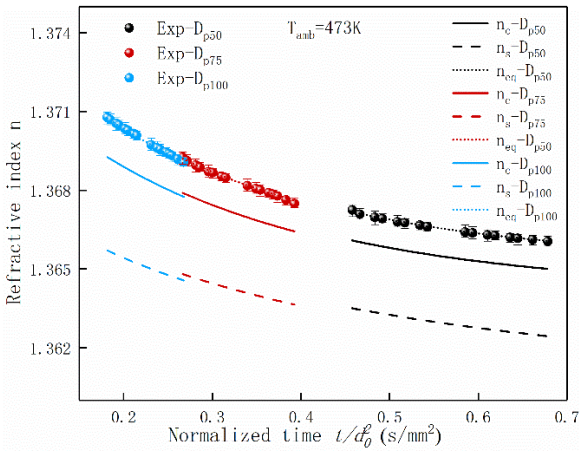

Figure 5.17 The variation of refractive index for three droplets.

After comparing the transient refractive index of three droplets, the variation of the refractive index during the whole droplet lifetime is compared in **Figure 5.18**. It can be seen that the refractive index of a larger droplet is lower than that of a smaller droplet. The evolution of the refractive index can be separated into two stages, a rapid reduction period followed by an andante regression period, which holds for all the droplets. This behavior is the coupling influence of temperature and concentration in the liquid phase. As displayed in **Figure 5.19**, the temperature increases shapely during the transient heating stage, which leads to the remarkable decrease of refractive index during this stage. In addition, despite that the mass fraction of heptane at the droplet center remains constant during this stage, it decreases significantly at the droplet surface all the time, which intensifies the reduction of the refractive index. However, judging from the variation curves of the refractive index, the liquid phase temperature has a decisive role in controlling the refractive index during this stage. The composition in the liquid phase determines the variation of the refractive index later on.

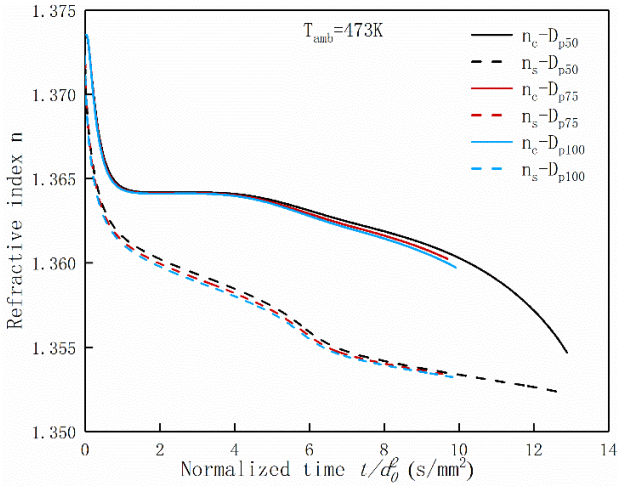

Figure 5.18 The variation of refractive index for droplets with different initial diameters under the ambient temperature of 473 K.

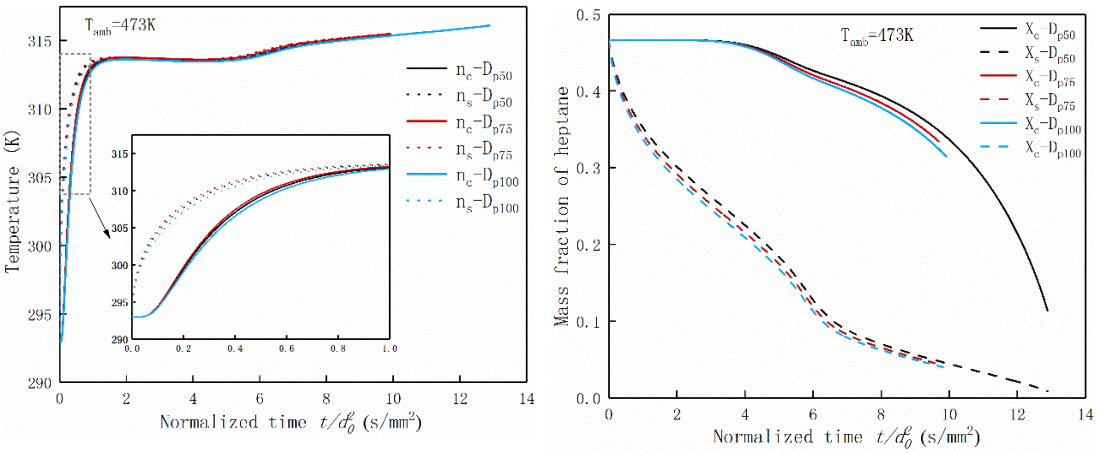

(a) Temperature **(b) Mass fraction of heptane**

Figure 5.19 The variation of temperature and concentration for three droplets.

5.3.3 Influencing factors of equivalent refractive indices

It is observed that the difference of the resulting equivalent refractive index and the refractive index at droplet surface links with the refractive index gradient in the liquid phase. Taking ETH25 droplet as an example, the measured refractive index differs obviously from the value in the liquid phase under the ambient temperature of 473 K compared with that under the 473 K condition. Therefore, the relationship of those differences is plotted in **Figure 5.20**. The horizontal axis is the refractive index difference between droplet surface and center, while the vertical axis stands for the minus of refractive index at droplet surface and equivalent refractive index. All the data

points in **Figure 5.14**b and **Figure 5.17** are utilized for plotting the fitting curve. The results demonstrate a linear relationship between the refractive index gradient in the liquid phase and the resulting refractive index. The larger the refractive index gradient in the liquid phase, the larger difference between the equivalent refractive index and the refractive index at the droplet center. It indicates that when the refractive index at the droplet center is smaller than the value at the droplet surface, the resulting equivalent refractive index is smaller than the refractive index at the droplet center, i.e., smaller than the smallest value in the liquid phase. Conversely, when the refractive index at the droplet center is larger than the value at the droplet surface, the equivalent refractive index is larger than the refractive index at the droplet center, i.e., larger than the largest value in the liquid phase.

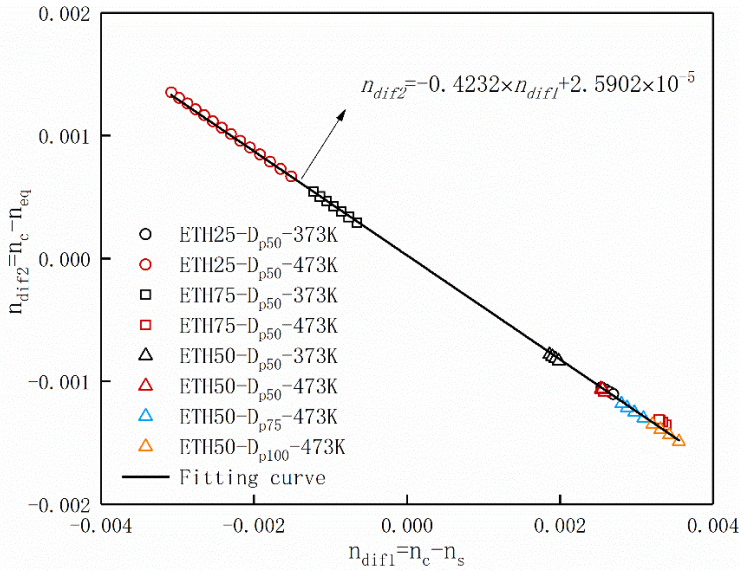

Figure 5.20 The relationship of refractive index difference among droplet surface, droplet center, and the equivalent refractive index.

5.4 Summary

The evaporation behavior of ethanol and heptane binary droplet has been investigated in this chapter by using both experiment and simulation methods. The main contribution is the observation of an inverse evaporation order of heptane and ethanol components due to the impact of non-ideal vapor-liquid equilibrium. Besides, the preferential behavior of ethanol and heptane binary droplet is confirmed with the rainbow measurement for the first time. The results provide a new sight to measure and

understand the evaporation behavior of binary droplets. Major concluding remarks are as follows:

1. The influence of non-ideal vapor-liquid equilibrium on the preferential evaporation of binary droplet is evaluated. The results reveal a significant change of separation factor and an inversion of the evaporation order of ethanol and heptane components at the droplet surface when the lighter component dominates the mixture.
2. The comparison of the refractive index between the rainbow measurements and model predictions confirms the accuracy of the non-ideal vapor-liquid equilibrium model in predicting the preferential evaporation behavior of binary droplet for the first time. The necessity of considering the impact of the non-ideal mixture has also been demonstrated.
3. The coupling influence of ambient temperature, pressure, and compositions in the liquid phase on the preferential evaporation behavior of droplets is revealed. It reveals that the effect of the non-ideal vapor-liquid equilibrium is more likely to be affected by ambient conditions when the lighter components dominant the mixture.
4. The joint influence of temperature and liquid compositions on the refractive index of the binary droplet is obtained. The temperature controls the variation of the refractive index in the early evaporation stage while the composition determines the refractive index later on. Besides, the composition dominates the spatial distribution of the refractive index near the droplet surface.

6. Conclusions and future work

6.1 Conclusions

Droplet transport and evaporation are ubiquitous in many industries and biological applications ranging from engines to thermal management to inkjet printing and so on. The evaporation of droplets in engines decides the formation of fuel vapor, which is critical for the combustion behavior of fuel spray and the emission performance. Meanwhile, the ever-rising emission standard and the environmental-friendly awareness bring up the change of evaporation environment and a number of green alternative fuels. Both the change of fuel type and vaporizing conditions have a significant impact on the droplet evaporation process. The investigations on the evaporation process of different kinds of droplets under complex ambient conditions are essential to achieve clean and efficient combustion. The combination of experimental method and simulation approaches have been utilized to shed a light on the joint influence of ambient conditions and liquid fuel type on the evaporation behavior of droplets. The high accuracy optical rainbow refractometry has been designed and established. An inversion algorithm considering a parabolic refractive index gradient in the liquid phase has been proposed to simultaneously extract the diameter and temperature distributions from the scattering light patterns. A systematical analysis of the differences between the experimental data and simulation results has been made. The main conclusions are as follows:

1. The droplet evaporation experimental system based on the rainbow technique has been designed and established, which is mainly composed of droplet generation, the high-temperature chamber, and the rainbow image system. The reliability and repeatability examinations have been made to ensure the accuracy of the rainbow measurement.
2. An inversion algorithm has been proposed to simultaneously extract the droplet diameter and temperature distributions from the scattering light patterns for the first time. The method improves the accuracy of the post-processing process by considering the impact of refractive index gradient and the modification of shape change on the rainbow angle.

3. A non-ideal vapor-liquid equilibrium model based on the effective conductivity and diffusivity model has been created. The method incorporates the impact of convection, the interactions between neighboring droplets, temperature-dependent physical parameters, and the polarity differences between different components. The accuracy of the established model is verified with the experimental data and simulation results in the literature.
4. The transient evaporation characteristics of free-falling ethanol and heptane droplets under different ambient temperatures are investigated with the rainbow technique. The parabolic distribution of refractive index along the radius direction is validated. The underlying relationship between the measured temperature and the temperature gradient inside droplet is revealed.
5. The impact of ambient temperature, the initial droplet diameter, and the fuel type on the reduction rate of droplet size and heating rate in the liquid phase has been obtained. The results indicate that less volatile droplets are more likely to be affected by the change of ambient temperature or the initial droplet size compared with more volatile droplets.
6. The influence of liquid compositions on the preferential evaporation behavior of binary droplet is observed. The results reveal a significant change of separation factor and an inversion of the evaporation order of ethanol and heptane component at the droplet surface when the lighter component ethanol dominates the mixture.
7. The comparison of the refractive index between the rainbow measurements and model predictions confirms the accuracy of the non-ideal vapor-liquid equilibrium model in predicting the preferential evaporation behavior of binary droplet for the first time. The coupling influence of ambient temperature, pressure, and compositions in the liquid phase on the preferential evaporation behavior of droplets is revealed.

6.2 Innovations

1. The high accuracy droplet evaporation setup based on the rainbow technique has been designed and established. An inversion algorithm has been proposed

by taking into account the impact of refractive index gradient and shape change of droplet on the rainbow angle. The diameter and temperature distributions of vaporizing droplets under high-temperature conditions have been measured simultaneously for the first time.

2. A non-ideal vapor-liquid equilibrium model based on the effective conductivity and diffusivity model has been created and validated. The method incorporates the impact of convection, the interactions between neighboring droplets, temperature-dependent physical parameters, and the polarity differences between different components.
3. The influence of liquid compositions on the preferential evaporation behavior of binary droplet is observed. The results reveal an inversion of the evaporation order of individual components at the droplet surface when the lighter component dominates the mixture. The rainbow experiment confirms the accuracy of non-ideal vapor-liquid equilibrium model in predicting the preferential evaporation behavior of binary droplet for the first time.

6.3 Future work

The accurate description of the droplet evaporation behavior and the development of evaporation theory and measurement technique has been achieved by coupling the experimental method and simulation approach in this work. Future work can focus on the evaporation behavior under high-pressure conditions. It is challenging to achieve a stable stream of a free-falling droplet in the first. On one hand, the pressure difference demands a higher injection pressure of the generator. On the other hand, any pressure disturbance leads to the oscillation of the droplet stream, which finally reflects on the distortion of scattering patterns. Furthermore, the simulation is designed for a single droplet, which is not strictly consistent with the experimental configuration. The neighboring droplet inside the droplet stream has an influence on the mass and thermal diffusion in the vapor phase, which is considered by the dimensionless spacing parameter in the present model. Further effort can be done on extending the single droplet model to droplet stream configurations.

References

[1] A. Muddapur, J.V. Jose, S. Sahu, T. Sundararajan, Spray dynamics and evaporation in a multihole GDI injector for pulsatile and split injection at elevated ambient pressure and temperature conditions, Fuel, 279 (2020) 118057.

[2] G. Liu, H. Cao, J. Xu, Solar evaporation of a hanging plasmonic droplet, Sol. Energy, 170 (2018) 184-191.

[3] S. Lei, Y. Shi, G. Chen, Heat-pipe based spray-cooling thermal management system for lithium-ion battery: Experimental study and optimization, Int. J. Heat Mass Transfer, 163 (2020) 120494.

[4] Y. Yang, L. Yang, X. Du, Y. Yang, Pre-cooling of air by water spray evaporation to improve thermal performance of lithium battery pack, Appl. Therm. Eng., 163 (2019) 114401.

[5] S. Hatte, K. Pandey, K. Pandey, S. Chakraborty, S. Basu, Universal evaporation dynamics of ordered arrays of sessile droplets, J. Fluid Mech., 866 (2019) 61-81.

[6] R. Bhardwaj, A. Agrawal, Likelihood of survival of coronavirus in a respiratory droplet deposited on a solid surface, Phys. Fluids, 32 (2020) 061704.

[7] B. Al Zaitone, Oblate spheroidal droplet evaporation in an acoustic levitator, Int. J. Heat Mass Transfer, 126 (2018) 164-172.

[8] W. Ranz, W.R. Marshall, Evaporation from drops, Chem. eng. prog, 48(3) (1952) 141-146.

[9] M. Renksizbulut, M. Yuen, Experimental study of droplet evaporation in a high-temperature air stream, J. Heat Transfer, 105(2) (1983) 384-388.

[10] M. Manjunath, V. Raghavan, P.S. Mehta, Vaporization characteristics of suspended droplets of biodiesel fuels of Indian origin and their diesel blends – An experimental study, Int. J. Heat Mass Transfer, 88 (2015) 28-41.

[11] C. Verwey, M. Birouk, Experimental investigation of the evaporation of suspended mono-sized heptane droplets in turbulence intensities approaching unity, Combust. Flame, 219 (2020) 425-436.

[12] J. Wang, X. Huang, X. Qiao, D. Ju, C. Sun, Experimental study on effect of support fiber on fuel droplet vaporization at high temperatures, Fuel, 268 (2020) 117407.

[13] I. Javed, S.W. Baek, K. Waheed, Evaporation characteristics of heptane droplets with the addition of aluminum nanoparticles at elevated temperatures, Combust. Flame, 160(1) (2013) 170-183.

[14] C. Chauveau, M. Birouk, F. Halter, I. Gokalp, An analysis of the droplet support fiber effect on the evaporation process, Int. J. Heat Mass Transfer, 128 (2019) 885-891.

[15] J.R. Yang, S.C. Wong, An experimental and theoretical study of the effects of heat conduction through the support fiber on the evaporation of a droplet in a weakly convective flow, Int. J. Heat Mass Transfer, 45(23) (2002) 4589-4598.

[16] H.L.-u. Rehman, J. Weiss, P. Seers, Effect of heat conduction on droplet life time and evaporation rate under forced convection at low temperatures, Exp. Therm. Fluid Sci., 72 (2016) 59-66.

[17] K. Han, G. Song, X. Ma, B. Yang, An experimental and theoretical study of the

effect of suspended thermocouple on the single droplet evaporation, Appl. Therm. Eng., 101 (2016) 568-575.
[18] L. Wang, J. Wang, X. Qiao, D. Ju, Z. Lin, Effect of ambient temperature on the micro-explosion characteristics of soybean oil droplet: The phenomenon of evaporation induced vapor cloud, Int. J. Heat Mass Transfer, 139(08) (2019) 736-746.
[19] J. Wang, X. Qiao, D. Ju, C. Sun, T. Wang, Bubble nucleation, micro-explosion and residue formation in superheated jatropha oil droplet: The phenomena of vapor plume and vapor cloud, Fuel, 261 (2020) 116431.
[20] M. Zhu, Z. Zhang, Y. Zhang, P. Liu, D. Zhang, An experimental investigation into the ignition and combustion characteristics of single droplets of biochar water slurry fuels in air, Appl. Energy, 185 (2017) 2160-2167.
[21] I. Javed, S.W. Baek, K. Waheed, Autoignition and combustion characteristics of kerosene droplets with dilute concentrations of aluminum nanoparticles at elevated temperatures, Combust. Flame, 162(3) (2015) 774-787.
[22] X. Ma, F. Zhang, K. Han, B. Yang, G. Song, Evaporation characteristics of acetone–butanol–ethanol and diesel blends droplets at high ambient temperatures, Fuel, 160 (2015) 43-49.
[23] H. Nomura, T. Murakoshi, Y. Suganuma, Y. Ujiie, N. Hashimoto, H. Nishida, Microgravity experiments of fuel droplet evaporation in sub-and supercritical environments, Proc. Combust. Inst., 36(2) (2017) 2425-2432.
[24] K. Han, C. Zhao, G. Fu, F. Zhang, S. Pang, Y. Li, Evaporation characteristics of dual component droplet of benzyl azides-hexadecane mixtures at elevated temperatures, Fuel, 157 (2015) 270-278.
[25] X. Huang, J. Wang, Y. Wang, X. Qiao, D. Ju, C. Sun, Q. Zhang, Experimental study on evaporation and micro-explosion characteristics of biodiesel/n-propanol blended droplet, Energy, 205 (2020) 118031.
[26] G.B. Chen, Y.H. Li, C.H. Lan, H.T. Lin, Y.C. Chao, Micro-explosion and burning characteristics of a single droplet of pyrolytic oil from castor seeds, Appl. Therm. Eng., 114 (2017) 1053-1063.
[27] V. Deprédurand, G. Castanet, F. Lemoine, Heat and mass transfer in evaporating droplets in interaction: Influence of the fuel, Int. J. Heat Mass Transfer, 53(17) (2010) 3495-3502.
[28] L. Perrin, G. Castanet, F. Lemoine, Characterization of the evaporation of interacting droplets using combined optical techniques, Exp. Fluids, 56(2) (2015) 1-16.
[29] T. Hillenbrand, D. Brüggemann, Evaporation of free falling droplets of binary alkane-ethanol blends, Fuel, 274 (2020) 117869.
[30] K. Han, B. Pang, X. Ma, H. Chen, G. Song, Z. Ni, An experimental study of the burning characteristics of acetone–butanol–ethanol and diesel blend droplets, Energy, 139 (2017) 853-861.
[31] R. Volkov, P. Strizhak, Using Planar Laser Induced Fluorescence to determine temperature fields of drops, films, and aerosols, Measurement, 153 (2020) 107439.
[32] C. Li, Q. Lv, Y. Wu, X. Wu, C. Tropea, Measurement of transient evaporation of

an ethanol droplet stream with phase rainbow refractometry and high-speed microscopic shadowgraphy, Int. J. Heat Mass Transfer, 146 (2020) 118843.
[33] Q. Lu, L.A. Melton, Measurement of transient temperature field within a falling droplet, AIAA J., 38(1) (2000) 95-101.
[34] F. Grisch, M. Orain, Role of Planar Laser-Induced Fluorescence in Combustion Research, (2009).
[35] H.-E. Albrecht, N. Damaschke, M. Borys, C. Tropea, Laser Doppler and phase Doppler measurement techniques, Springer Science & Business Media, 2013.
[36] G. Chen, M.M. Mazumder, R.K. Chang, J.C. Swindal, W.P. Acker, Laser diagnostics for droplet characterization: application of morphology dependent resonances, Prog. Energy Combust. Sci., 22(2) (1996) 163-188.
[37] S. Saengkaew, Study of spray heat up: on the development of global rainbow techniques, Rouen, 2005.
[38] G. Gouesbet, G. Gréhan, L. Méès, Light scattering theory and practice: beyond velocity and size measurements, 10th international conference of liquid atomization and spray systems, 2006.
[39] J.P.A.J. van Beeck, Rainbow phenomena: development of a laser-based, non-intrusive technique for measuring droplet size, temperature and velocity, 1997.
[40] S.V. Sankar, D.H. Buermann, W.D. Bachalo, Application of Rainbow Thermometry to the Study of Fuel Droplet Heat-Up and Evaporation Characteristics, ASME 1996 International Gas Turbine and Aeroengine Congress and Exhibition, American Society of Mechanical Engineers Digital Collection, 1996.
[41] J. Van Beeck, D. Giannoulis, L. Zimmer, M. Riethmuller, Global rainbow thermometry for droplet-temperature measurement, Opt. Lett., 24(23) (1999) 1696-1698.
[42] T. Scott, Michael Scot and the Four Rainbows, Transversal: International Journal for the Historiography of Science, (2) (2017) 204-204.
[43] H.C. Hulst, H.C. van de Hulst, Light scattering by small particles, Courier Corporation, 1981.
[44] C. Kanjanasakul, Analysis of the optical properties of droplets of different fluids in high-pressure environments by rainbow optical diagnostic, Normandie Université, 2017.
[45] J.A. Adam, The mathematical physics of rainbows and glories, Physics Reports, 356(4) (2002) 229-365.
[46] G. Mie, Beiträge zur Optik trüber Medien, speziell kolloidaler Metallösungen, Annalen der Physik, 330(3) (1908) 377-445.
[47] P. Debye, The diffraction theory of aberrations, Ann. Phys.(Leipzig), 30 (1909) 59-62.
[48] R. Li, H. Jiang, K.F. Ren, Debye series for light scattering by a multilayered sphere, Appl. Opt., 45(6) (2006) 1260-1270.
[49] H. Nussenzveig, High‐frequency scattering by a transparent sphere. II. Theory of the rainbow and the glory, J. Math. Phys., 10(1) (1969) 125-176.
[50] S. Saengkaew, T. Charinpanikul, C. Laurent, Y. Biscos, G. Lavergne, G. Gouesbet,

G. Gréhan, Processing of individual rainbow signals, Exp. Fluids, 48(1) (2010) 111-119.
[51] J. Wilms, B. Weigand, Composition measurements of binary mixture droplets by rainbow refractometry, Appl. Opt., 46(11) (2007) 2109-2118.
[52] N. Roth, K. Anders, A. Frohn, Simultaneous measurement of temperature and. size of droplets in the micrometer range, J. Laser Appl. 2(1) (1990) 37-42.
[53] N. Roth, K. Anders, A. Frohn, Refractive-index measurements for the correction of particle sizing methods, Appl. Opt., 30(33) (1991) 4960-4965.
[54] N. Roth, K. Anders, A. Frohn, Determination of size, evaporation rate and freezing of water droplets using light scattering and radiation pressure, Particle & particle systems characterization, 11(3) (1994) 207-211.
[55] J. Promvongsa, P. Vallikul, B. Fungtammasan, A. Garo, G. Grehan, S. Saengkaew, Multicomponent fuel droplet evaporation using 1D Global Rainbow Technique, Proc. Combust. Inst., 36(2) (2017) 2401-2408.
[56] X. Wu, H. Jiang, Y. Wu, J. Song, G. Gréhan, S. Saengkaew, L. Chen, X. Gao, K. Cen, One-dimensional rainbow thermometry system by using slit apertures, Opt. Lett., 39(3) (2014) 638-641.
[57] Y. Wu, J. Promvongsa, X. Wu, K. Cen, G. Grehan, S. Saengkaew, One-dimensional rainbow technique using Fourier domain filtering, Opt. Express, 23(23) (2015) 30545-30556.
[58] Y. Wu, J. Promvongsa, S. Saengkaew, X. Wu, J. Chen, G. Gréhan, Phase rainbow refractometry for accurate droplet variation characterization, Opt. Lett., 41(20) (2016) 4672-4675.
[59] Y. Wu, C. Crua, H. Li, S. Saengkaew, L. Maedler, X. Wu, G. Grehan, Simultaneous measurement of monocomponent droplet temperature/refractive index, size and evaporation rate with phase rainbow refractometry, J. Quant. Spectros. Radiat. Transfer, 214 (2018) 146-157.
[60] Y. Wu, H. Li, X. Wu, G. Gréhan, L. Mädler, C. Crua, Change of evaporation rate of single monocomponent droplet with temperature using time-resolved phase rainbow refractometry, Proc. Combust. Inst., 37(3) (2019) 3211-3218.
[61] C. Li, Y. Wu, X. Wu, C. Tropea, Simultaneous measurement of refractive index, diameter and colloid concentration of a droplet using rainbow refractometry, J. Quant. Spectrosc. Radiat. Transfer, (2020) 106834.
[62] C. Maqua, G. Castanet, F. Lemoine, Bicomponent droplets evaporation: Temperature measurements and modelling, Fuel, 87(13-14) (2008) 2932-2942.
[63] A.Y. Snegirev, Transient temperature gradient in a single-component vaporizing droplet, Int. J. Heat Mass Transfer, 65 (2013) 80-94.
[64] L. Kai, P. Massoli, Scattering of electromagnetic-plane waves by radially inhomogeneous spheres: a finely stratified sphere model, Appl. Opt., 33(3) (1994) 501-511.
[65] F. Onofri, G. Gréhan, G. Gouesbet, Electromagnetic scattering from a multilayered sphere located in an arbitrary beam, Appl. Opt., 34(30) (1995) 7113-7124.
[66] Z.S. Wu, L.X. Guo, K.F. Ren, G. Gouesbet, G. Gréhan, Improved algorithm for electromagnetic scattering of plane waves and shaped beams by multilayered

spheres, Appl. Opt., 36(21) (1997) 5188-5198.
[67] Z. Wu, Y. Wang, Electromagnetic scattering for multilayered sphere: recursive algorithms, Radio Sci., 26(6) (1991) 1393-1401.
[68] M.R. Vetrano, J. van Beeck, M. Riethmuller, Temperature gradient measurements in combustion droplets by standard rainbow thermometry, European Conference on Liquid Atomization and Spray Systems, Como, 2008.
[69] M.R. Vetrano, J.P.A.J. van Beeck, M.L. Riethmuller, Generalization of Rainbow Airy theory to nonuniform spheres, Opt. Lett., 30(6) (2005) 658-660.
[70] M.R. Vetrano, J.P.A.J. van Beeck, M.L. Riethmuller, Assessment of refractive index gradients by standard rainbow thermometry, Appl. Opt., 44(34) (2005) 7275-7281.
[71] S. Saengkaew, T. Charinpanitkul, H. Vanisri, W. Tanthapanichakoon, Y. Biscos, N. Garcia, G. Lavergne, L. Mees, G. Gouesbet, G. Grehan, Rainbow refractrometry on particles with radial refractive index gradients, Exp. Fluids, 43(4) (2007) 595-601.
[72] J. Zhou, Y. Fang, J. Wang, L. Zhu, T. Wriedt, Rainbow pattern analysis of a multilayered sphere for optical diagnostic of a heating droplet, Opt. Commun., 441 (2019) 113-120.
[73] C. Laurent, Y. Biscos, N. Doué, C. Maqua, F. Lemoine, G. Gréhan, G. Lavergne, Thermal gradient determination inside vaporizing droplets by combining rainbow and laser induced fluorescence measurements, Fluids Engineering Division Summer Meeting, 2006, 909-916.
[74] R.J. Hopkins, R. Symes, R.M. Sayer, J.P. Reid, Determination of the size and composition of multicomponent ethanol/water droplets by cavity-enhanced Raman scattering, Chem. Phys. Lett., 380(5-6) (2003) 665-672.
[75] C.D. Rosebrock, S. Shirinzadeh, M. Soeken, N. Riefler, T. Wriedt, R. Drechsler, L. Mädler, Time-resolved detection of diffusion limited temperature gradients inside single isolated burning droplets using Rainbow Refractometry, Combust. Flame, 168 (2016) 255-269.
[76] D.B. Spalding, The combustion of liquid fuels, Proc. Combust. Inst, 4(1) (1953) 847-864.
[77] G. Godsave, Studies of the combustion of drops in a fuel spray-the burning of single drops of fuel, Symposium (International) on Combustion, 4(1) (1953) 818-830.
[78] M. Goldsmith, On the burning of single drops of fuel in a oxidizing atmosphere, Biophys. J., 24(4) (1954) 2467–2483.
[79] G.M. Faeth, Current status of droplet and liquid combustion, Progress in Energy & Combustion Science, 3(4) (1977) 191-224.
[80] C.K. Law, W. Sirignano, Unsteady droplet combustion with droplet heating-II: conduction limit, Combust. Flame, 28 (1977) 175-186.
[81] C. Law, Internal boiling and superheating in vaporizing multicomponent droplets, AlChE J., 24(4) (1978) 626-632.
[82] B. Abramzon, W. Sirignano, Droplet vaporization model for spray combustion calculations, Int. J. Heat Mass Transfer, 32(9) (1989) 1605-1618.

[83] S.S. Sazhin, A. Elwardany, P.A. Krutitskii, G. Castanet, F. Lemoine, E.M. Sazhina, M.R. Heikal, A simplified model for bi-component droplet heating and evaporation, Int. J. Heat Mass Transfer, 53(21) (2010) 4495-4505.
[84] Z. Ni, C. Hespel, K. Han, F. Foucher, Numerical simulation of heat and mass transient behavior of single hexadecane droplet under forced convective conditions, Int. J. Heat Mass Transfer, 167 (2021) 120736.
[85] A. Saufi, A. Frassoldati, T. Faravelli, A. Cuoci, DropletSMOKE++: A comprehensive multiphase CFD framework for the evaporation of multidimensional fuel droplets, Int. J. Heat Mass Transfer, 131 (2019) 836-853.
[86] G. Strotos, I. Malgarinos, N. Nikolopoulos, M. Gavaises, Predicting the evaporation rate of stationary droplets with the VOF methodology for a wide range of ambient temperature conditions, Int. J. Therm. Sci., 109 (2016) 253-262.
[87] A.P. Pinheiro, J.M. Vedovoto, Evaluation of Droplet Evaporation Models and the Incorporation of Natural Convection Effects, Pinheiro, Abgail P, 102(3) (2019) 537-558.
[88] G.S. Zhu, S.K. Aggarwal, Transient supercritical droplet evaporation with emphasis on the effects of equation of state, Int. J. Heat Mass Transfer, 43(7) (2000) 1157-1171.
[89] B. Balaji, V. Raghavan, K. Ramamurthi, G. Gogos, A numerical study of evaporation characteristics of spherical n-dodecane droplets in high pressure nitrogen environment, Phys. Fluids, 23(6) (2011) 063601.
[90] A.P. Pinheiro, J.M. Vedovoto, A. da Silveira Neto, B.G. van Wachem, Ethanol droplet evaporation: Effects of ambient temperature, pressure and fuel vapor concentration, Int. J. Heat Mass Transfer, 143 (2019) 118472.
[91] S.S. Sazhin, Modelling of fuel droplet heating and evaporation: Recent results and unsolved problems, Fuel, 196 (2017) 69-101.
[92] G. Brenn, Concentration fields in evaporating droplets, Int. J. Heat Mass Transfer, 48(2) (2005) 395-402.
[93] S. Sazhin, Droplets and sprays, Springer, 2014.
[94] Y. Ra, R.D. Reitz, A vaporization model for discrete multi-component fuel sprays, Int. J. Multiphase Flow, 35(2) (2009) 101-117.
[95] S.S. Sazhin, M.A. Qubeissi, R. Kolodnytska, A.E. Elwardany, H. Ricardo, Modelling of biodiesel fuel droplet heating and evaporation, Fuel, 115 (2014).
[96] L. Chen, Z. Liu, Y. Lin, Z. Chi, Different spray droplet evaporation models for non-ideal multi-component fuels with experimental validation, Int. J. Heat Mass Transfer, 94(3) (2016) 292-300.
[97] G. Brenn, L. Deviprasath, F. Durst, C. Fink, Evaporation of acoustically levitated multi-component liquid droplets, Int. J. Heat Mass Transfer, 50(25-26) (2007) 5073-5086.
[98] P. Narasu, S. Boschmann, P. Pöschko, F. Zhao, E. Gutheil, Modeling and Simulation of Single Ethanol/Water Droplet Evaporation in Dry and Humid Air, Combust. Sci. Technol., 192(7) (2020) 1233-1252.
[99] A. Bader, P. Keller, C. Hasse, The influence of non-ideal vapor–liquid equilibrium on the evaporation of ethanol/iso-octane droplets, Int. J. Heat Mass Transfer, 64

(2013) 547-558.
[100] P. Keller, A. Bader, C. Hasse, The influence of intra-droplet heat and mass transfer limitations in evaporation of binary hydrocarbon mixtures, Int. J. Heat Mass Transfer, 67 (2013) 1191-1207.
[101] Z. Ni, K. Han, C. Zhao, H. Chen, B. Pang, Numerical simulation of droplet evaporation characteristics of multi-component acetone-butanol-ethanol and diesel blends under different environments, Fuel, 230(10) (2018) 27-36.
[102] T.S.a.M.H. Cyril Crua, High-speed microscopic imaging of the initial stage of diesel spray formation and primary breakup, Sae Technical Papers, (2010).
[103] M. Birouk, S.C. Fabbro, Droplet evaporation in a turbulent atmosphere at elevated pressure - Experimental data, Proc. Combust. Inst., 34 (2013) 1577-1584.
[104] E. Loth, Quasi-steady shape and drag of deformable bubbles and drops, Int. J. Multiphase Flow, 34(6) (2008) 523-546.
[105] D. Gera, M.P. Mathur, M.C. Freeman, A. Robinson, Effect of large aspect ratio of biomass particles on carbon burnout in a utility boiler, Energy & Fuels, 16(6) (2002) 1523-1532.
[106] J. Li, J. Zhang, A theoretical study of the spheroidal droplet evaporation in forced convection, Phys. Lett. A, 378(47) (2014) 3537-3543.
[107] S. Tonini, G. Cossali, An evaporation model for oscillating spheroidal drops, Int. Commun. Heat Mass Transfer, 51 (2014) 18-24.
[108] S. Tonini, G.E. Cossali, One-dimensional analytical approach to modelling evaporation and heating of deformed drops, Int. J. Heat Mass Transfer, 97 (2016) 301-307.
[109] V.S. Zubkov, G.E. Cossali, S. Tonini, O. Rybdylova, C. Crua, M. Heikal, S.S. Sazhin, Mathematical modelling of heating and evaporation of a spheroidal droplet, Int. J. Heat Mass Transfer, 108 (2017) 2181-2190.
[110] B. Al Zaitone, Evaporation of oblate spheroidal droplets: A theoretical analysis, Chem. Eng. Commun., 205(1) (2018) 110-121.
[111] H. Yu, J. Shen, C. Tropea, Application of vector ray tracing to the computation of Möbius shifts for the primary and secondary rainbows, Appl. Opt., 54(31) (2015) 9093-9101.
[112] H. Li, C.D. Rosebrock, T. Wriedt, L. M?Dler, The effect of initial diameter on rainbow positions and temperature distributions of burning single-component n-Alkane droplets, J. Quant. Spectrosc. Radiat. Transfer, 195 (2017) 164-175.
[113] Y. Wu, Q. Lv, X. Wu, X. Wang, K. Cen, Simultaneous measurement of surface tension and viscosity of oscillating droplet using time-resolved rainbow refractometry, Powder Technol., 391 (2021) 425-431.
[114] J. Jackson, From Alexander of Aphrodisias to Young and Airy, Physics reports, 320(1-6) (1999) 27-36.
[115] M. Abramowitz, Elementary analytical methods, Handbook of mathematical functions, Dover, New York, 1972.
[116] MiePlot, Available from: http://www.philiplaven.com/mieplot.htm (accessed on March 15th, 2022).
[117] S. Saengkaew, T. Charinpanitkul, H. Vanisri, W. Tanthapanichakoon, L. Mees, G.

Gouesbet, G. Grehan, Rainbow refractrometry: on the validity domain of Airy's and Nussenzveig's theories, Opt. Commun., 259(1) (2006) 7-13.
[118] R. Francesconi, S. Ottani, Correlation of density and refraction index for liquid binary mixtures containing polyglycols. Use of the group contributions in the Lorentz–Lorenz, Gladstone–Dale and Vogel equations to evaluate the density of mixtures, J. Mol. Liq., 133(1-3) (2007) 125-133.
[119] T. Smith, R. Bonner, Refractive index-temperature data for anhydrous ethyl alcohol, Anal. Chem., 24(3) (1952) 517-518.
[120] W. M bius, Zur Theorie des Regenbogens und ihrer experimentellen Pr fung, Annalen der Physik, 338(16) (1910) 1493-1558.
[121] J.S. Rosen, The refractive indices of alcohol, water, and their mixtures at high pressures, Rosen, Joseph S, 37(11) (1947) 932-938.
[122] C. Chen, K. Vedam, Piezo‐and elasto‐optic properties of liquids under high pressure. III. Results on twelve more liquids, Chen, CC, 73(9) (1980) 4577-4584.
[123] R.J. Riobóo, M. Philipp, M. Ramos, J.-K. Krüger, Concentration and temperature dependence of the refractive index of ethanol-water mixtures: Influence of intermolecular interactions, Riobóo, RJ Jiménez, 30(1) (2009) 19.
[124] K. Kerl, H. Varchmin, Refractive index dispersion (RID) of some liquids in the UV/VIS between 20° C and 60° C, J. Mol. Struct., 349 (1995) 257-260.
[125] J. Tojo, C. Diaz, Densities and refractive indices for 1-hexene+ o-xylene,+ m-xylene,+ p-xylene, and+ ethylbenzene, J. Chem. Eng. Data, 40(1) (1995) 96-98.
[126] A.Z. Tasic, B.D. Djordjevic, D.K. Grozdanic, N. Radojkovic, Use of mixing rules in predicting refractive indexes and specific refractivities for some binary liquid mixtures, J. Chem. Eng. Data, 37(3) (1992) 310-313.
[127] L. Lorenz, Ueber die refractionsconstante, Annalen der Physik, 247(9) (1880) 70-103.
[128] S. Saengkaew, D. Bonin, G. Grehan, Measurement of droplets temperature in a flame by using a global rainbow technique with a pulse laser, 23rd Annual Conference on Liquid Atomization and Spray Systems, 2010.
[129] J.P. van Beeck, M.L. Riethmuller, Rainbow interferometry with wire diffraction for simultaneous measurement of droplet temperature, size and velocity, Particle & particle systems characterization, 14(4) (1997) 186-192.
[130] C.A. Varnavas, A droplet evaporation model for high temperature and pressure spray applications, (1995).
[131] S. Gavhane, S. Pati, S. Som, Evaporation of multicomponent liquid fuel droplets: Influences of component composition in droplet and vapor concentration in free stream ambience, International Journal of Thermal Sciences, 105 (2016) 83-95.
[132] N.A. Fuchs, Evaporation and droplet growth in gaseous media, Elsevier, 2013.
[133] R. Nafziger, Convective droplet transport phenomena in high-temperature air streams, University of Waterloo, 1989.
[134] W.A. Sirignano, Fuel droplet vaporization and spray combustion theory, Progress in Energy and Combustion Science, 9(4) (1983) 291-322.
[135] C.K. Law, H. Law, A d2-law for multicomponent droplet vaporization and combustion, AIAA J., 20(4) (1982) 522-527.

[136] J.M. Smith, Introduction to chemical engineering thermodynamics, ACS Publications, 1950.
[137] G. Castanet, L. Perrin, O. Caballina, F. Lemoine, Evaporation of closely-spaced interacting droplets arranged in a single row, Int. J. Heat Mass Transfer, 93 (2016) 788-802.
[138] A. Atthasit, N. Doué, Y. Biscos, G. Lavergne, Influence of droplet concentration on the dynamics and evaporation of a monodisperse stream of droplets in evaporation regime, in: First international symposium on combustion and atmospheric pollution, St-Petersburg, Russia, 2003.
[139] J. Virepinte, Y. Biscos, G. Lavergne, P. Magre, G. Collin, A rectilinear droplet stream in combustion: droplet and gas phase properties, Combust. Sci. Technol., 150(1-6) (2000) 143-159.
[140] H. Zhang, C.K. Law, Effects of temporally varying liquid-phase mass diffusivity in multicomponent droplet gasification, Combust. Flame, 153(4) (2008) 593-602.
[141] B.E. Poling, J.M. Prausnitz, J.P. O'connell, The properties of gases and liquids, Mcgraw-hill New York, 2001.
[142] X. Ma, F. Zhang, K. Han, G. Song, Numerical modeling of acetone–butanol–ethanol and diesel blends droplet evaporation process, Fuel, 174 (2016) 206-215.
[143] V.Y. Borodulin, V. Letushko, M. Nizovtsev, A. Sterlyagov, The Experimental Study of Evaporation of Water–Alcohol Solution Droplets, Colloid J., 81(3) (2019) 219-225.
[144] V.Y. Borodulin, V. Letushko, M. Nizovtsev, A. Sterlyagov, Determination of parameters of heat and mass transfer in evaporating drops, Int. J. Heat Mass Transfer, 109 (2017) 609-618.
[145] N. Al-Esawi, M. Al Qubeissi, S.S. Sazhin, R. Whitaker, The impacts of the activity coefficient on heating and evaporation of ethanol/gasoline fuel blends, Int. Commun. Heat Mass Transfer, 98 (2018) 177-182.
[146] S. Saengkaew, G. Godard, J.B. Blaisot, G. Gréhan, Experimental analysis of global rainbow technique: sensitivity of temperature and size distribution measurements to non-spherical droplets, Exp. Fluids, 47(4) (2009) 839.
[147] M. Bardi, A.D. Lella, G. Bruneaux, A novel approach for quantitative measurements of preferential evaporation of fuel by means of two-tracer laser induced fluorescence, Fuel, 239(3) (2019) 521-533.